A Song of Atmosphere and Ocean:
Modeling and Simulation-Based Study of Nonlinear Waves

A THESIS
SUBMITTED TO THE FACULTY OF THE GRADUATE SCHOOL
OF THE UNIVERSITY OF MINNESOTA
BY

Xuanting Hao

IN PARTIAL FULFILLMENT OF THE REQUIREMENTS
FOR THE DEGREE OF
DOCTOR OF PHILOSOPHY

Lian Shen, Adviser

August 2019

Acknowledgement

I would like to express my special thanks of gratitude to my adviser, Professor Lian Shen, who introduced me into the fascinating area of computational fluid dynamics and physical oceanography. I couldn't be more grateful for the extremely valuable academic survival skills I learned from him, to name a few, identifying research ideas, scientific writing, self-management, etc. His forever enthusiasm and love for fundamental fluid dynamics studies have always inspired me to embrace the challenges.

Besides my advisor, I am profoundly grateful to other members of my preliminary and final exam committee, Professor Michele Guala, Professor Jiarong Hong, Professor Sungyon Lee, Professor Joseph W. Nichols, and Professor Fotis Sotiropoulos for their time and support, especially considering that I scheduled my exams during the winter/summer break. I would also like to thank the instructors of fluid mechanics courses, Professor Graham V. Candler, Professor Sean Garrick, Professor Ellen K. Longmire, and Professor Krishnan Mahesh, for making the topics on turbulence less formidable to me.

I am deeply indebted to Dr. Xin Guo for his remote tutorials in my first few years of study. Well-organized and easy to understand, these tutorials helped me to get through the most difficult times in the early stage. Xin has always been patient and prepared to help me with the debugging. Without his help, I would have struggled much longer with the numerical code.

I am fortunate enough to work together with all members of the Fluid Mechanics Lab, a lively community where new ideas emerge every day. In particular, I would like to thank Tao Cao and Anqing Xuan for their help on the numerical tools used in this work. Because of their effort, the numerical code saw a significant improvement

in the efficiency and robustness.

Finally, no words can truly express how grateful I am for the love and encouragement from my family. This work is for them: my parents and my lovely girlfriend, Zixuan Yan.

Abstract

Ocean waves play a critical role in connecting the atmosphere to the ocean and shaping the global climate. Existing statistics wave models are inappropriate for the mechanistic study of wave dynamics with nonlinearity and irregularity. We present a systematic study on nonlinear waves using deterministic models, with a focus on the fundamental momentum and energy transfer processes between waves and motions in the atmosphere and ocean. Numerical experiments are first carried out for turbulent wind blowing over a wave field with various wind speeds considered. The results show that the waves have a significant impact on the wind turbulent energy spectrum. By computing the universal constant in a wave-growth law proposed in the literature, we substantiate the scaling of wind–wave growth based on intrinsic wave properties. Another group of numerical experiments are conducted to investigate the momentum flux between wind and waves in the coastal region. We quantify the form drag and find it considerably larger in the coastal region case than in the open sea case. Our findings provide the direct computational evidence in support of the critical role wave shoaling plays in the increased coastal wind–wave momentum flux. In the final part, we investigate the oceanic internal wave impact on the surface wave. We directly capture the surface roughness signature with a deterministic two-layer model to avoid the singularity encountered in traditional ray theory. The surface signature characterized by a rough region followed by a smooth region traveling with a nondispersive internal wave is revealed by the local wave geometry variation in the physical space and the wave energy change in the spectral space. Our findings show that the formation of the surface signature is essentially an energy conservative process and justify the use of the wave-phase-resolved two-layer model.

Contents

List of Tables

List of Figures

1 Introduction

1.1 Motivations and background

Gravity waves are ubiquitous at the ocean surface. Whether at the open sea or in the coastal region, waves are an important part of the living environment of human beings. For instance, as a major source of the ship resistance, waves have accompanied all major human activities on the ocean since the early times of civilizations. Even in the legendary Homer epic, numerous description on waves can be found. Our study on waves is motivated by various scientific challenges and the socio–economic impacts: (1) As an major contributor to the momentum and energy transfer between the atmosphere and ocean, waves play a critical role in global climate (Cavaleri *et al.*, 2007); (2) Extremely high waves cause damage to offshore structures and ships (Dysthe *et al.*, 2008; Fedele *et al.*, 2016); (3) The remote sensing observation of the ocean rely on a better understanding of the wave field.

The generation and evolution of waves in the open sea has been observed and studied for a long time. In the past several decades, considerable progress has been made towards establishing operational wave models that help the understanding of the main features of waves and offer means to predict wave fields. Many statistical models have been proposed to describe the key physical processes such as wind–wave interaction and wave–current interaction. Due to the complexity of the wave system, however, existing wave models sometimes produce only qualitatively correct results and, often they cannot address site-specific flow physics when the wave conditions vary.

In the early days when computer simulations were not available, perturbation

expansions was the major tool for the analysis and calculation of wave properties. With the advent of computers, numerical simulation has become an indispensable tool in the study of waves. Early simulations were limited to simple waves, such as a monochromatic wave and combinations of linear waves. Recent years have seen a substantial increase of interest and activities in large scale simulations of complex wave field.

Wave models can be categorized into two types: (i) deterministic models in which wave fields are represented directly in physical space, such as the surface elevation with both the wave amplitude and phase resolved, and (ii) statistical models that describe the evolution of wave statistical quantities like the energy density function. Note that statistical models discard the wave phase information and only keep the amplitude for a specific wave component. As a result, statistical models are computationally less expensive but cannot provide as detailed information as the deterministic models. For example, statistical models can only quantify the probability for the occurrence of waves of certain magnitude, and cannot predict deterministically a specific wave event in physical space.

Today, we face two major challenges in the modeling of ocean wave field: nonlinearity and irregularity. The wave nonlinearity poses great challenges to the attempts to solve the problem analytically. The irregularity of wave field indicates that a successful wave prediction model can benefit from a combination of deterministic and statistical modeling approaches. In particular, the deterministic perspective has a great potential to improve the accuracy in wave simulation and forecasting.

1.2 Thesis overview

In this study, we apply a suite of deterministic wave models to the simulation of nonlinear wave fields, with impact from the atmospheric wind turbulence and the oceanic internal waves. While we focus on the fundamental physical mechanisms, we expect our knowledge to benefit research in physical oceanography, environmental sciences, renewable energy at sea, naval architecture, etc. From an academic point of view, the study of wave field may contribute to the study of nonlinear system dynamics in general.

In Chapter 2, we present a study on the interaction between wind and water waves with a broad-band spectrum using wave-phase-resolved simulation with long-term wave field evolution. The wind turbulence is computed using large-eddy simulation and the wave field is simulated using a high-order spectral method. Numerical experiments are carried out for turbulent wind blowing over a wave field initialised using the Joint North Sea Wave Project spectrum, with various wind speeds considered. The results show that the waves, together with the mean wind flow and large turbulent eddies, have a significant impact on the wavenumber–frequency spectrum of the wind turbulence. It is found that the shear stress contributed by sweep events in turbulent wind is greatly enhanced as a result of the waves. The dependence of the wave growth rate on the wave age is consistent with the results in the literature. The probability density function and high-order statistics of the wave surface elevation deviate from the Gaussian distribution, manifesting the nonlinearity of the wave field. The shape of the change in the spectrum of wind-waves resembles that of the nonlinear wave–wave interactions, indicating the dominant role played by the nonlinear interactions in the evolution of the wave spectrum. The frequency down-

shift phenomenon is captured in our simulations wherein the wind-forced wave field evolves for $O(3000)$ peak wave periods. Using the numerical result, we compute the universal constant in a wave-growth law proposed in the literature, and substantiate the scaling of wind–wave growth based on intrinsic wave properties.

Chapter 3 is devoted to the momentum flux between wind and waves in the coastal region. A number of previous field observations show that the wind–wave momentum flux in the coastal region exceeds the corresponding open sea value, the cause of which points to the wave shoaling effect, among other factors. To assess the contribution of wave shoaling to the enhanced momentum flux in the coastal region, we conduct a systematic study on the coastal wind–wave momentum transfer process using high-fidelity numerical simulations. In the first part of this chapter, we use wall-resolved large-eddy simulation (LES) to investigate wind turbulence over monochromatic waves propagating in coastal and oceanic waters. Our result shows that the momentum transfer in the coastal region case is significantly higher than the corresponding open sea case. We also observe quasi-periodic large-scale motions similar to those in channel flows and substantiate the correlation between the friction generation and the turbulence self-sustaining process. We quantify the form drag and find it considerably larger in the coastal region case than in the open sea case, which is associated with the qualitative difference in the wave-coherent components of the wind velocity and pressure field. A detailed analysis on the momentum budget shows that in the wave boundary layer the wave-induced momentum flux is small in the wind field in the open sea case, while in the coastal region case it is much higher. In the second part of the study, we use a mild slope equation to model the broad-band wave shoaling process along with wave refraction and nonlinear triad interactions. Several

phenomena are observed in the coastal region wave spectrum, including low-frequency waves, second-harmonic waves, and reduced directional spreading. The wind–wave momentum transfer is then quantified using a dynamic sea surface roughness model combined with wall-modelled LES and phase-resolved wave simulation. The resulting sea surface roughness is found to be over eight times that in open sea parameterisations, and the drag coefficient nearly doubles. The correlation function between the wind turbulence and wave surface elevation shows that the wave-coherent motions are much stronger in the coastal case. We have also identified the wave shoaling effect from the full wavenumber–frequency spectrum of wind turbulence. Our findings provide the direct computational evidence in support of the critical role wave shoaling plays in the increased coastal wind–wave momentum flux.

In Chapter 4, we investigate the oceanic internal wave impact on the surface wave, specifically, the surface signature associated with wave roughness change, which is critical for the identification and characterization of internal waves in oceans. With an $O(10^3 - 10^5)$ times difference in their length scales, it is challenging to simultaneously resolve the surface wave and internal wave dynamics. Here we present the first effort to directly capture the surface roughness signature with a deterministic two-layer model to avoid the singularity encountered in traditional ray theory. The surface signature characterized by a rough region followed by a smooth region traveling with a nondispersive internal wave is revealed by the local wave geometry variation in the physical space and the wave energy change in the spectral space. Our findings show that the formation of the surface signature is essentially an energy conservative process and justify the use of the wave-phase-resolved two-layer model.

2 Long-term Evolution of Coupled Wind–Wave System

2.1 Introduction

The momentum and energy transfer between wind and ocean surface waves is an essential component in air–sea interactions. It directly impacts the dynamics of the lower marine atmospheric boundary layer and the upper oceans. A solid understanding of the wind–wave interaction processes would bring benefits to society in applications, including marine weather forecasting, coping with natural and anthropologic hazards, energy harvest in offshore wind and wave farms, and marine ecosystem conservation, etc.

For deep water waves, it is wind forcing, nonlinear wave interactions, and wave breaking dissipation that dominate the dynamics of the wave field (Holthuijsen, 2007). Wave energy originates primarily from the wind blowing over the sea surface, an energy transfer process referred to as wind input. Jeffreys (1925, 1926) first proposed a separation sheltering mechanism to interpret the wind input to waves. He attributed wave growth to flow separation on the leeward side of the waves. His prediction of wave growth rate was found to be too low compared with measurements (see e.g. Young, 1999). Belcher & Hunt (1993) developed a non-separated sheltering theory, in which the thickening of the boundary layer on the leeward side of a wave causes a displacement of the mean flow and a pressure asymmetry in the outer region that contributes to the wave growth. The non-separated sheltering theory agrees much better with measurement data. Phillips (1957) proposed a theory in which he attributed

the main source of energy input to the resonance between the waves and the wind turbulence field, whereas the resulting linear growth rate is valid at the initial stage of wave generation. Miles (1957) used a quasi-linear theory to derive the Rayleigh equation for this problem and analysed the wave induced pressure perturbation using a predefined mean wind velocity profile. Miles' theory showed the importance of a characteristic height where the wind speed matches the phase speed of the progressive wave. A major limitation of Miles' theory is that the effect of turbulence was excluded from analysis. Real winds are much more complex. For example, their gustiness may have a significant impact on the wind–wave energy transfer (Nikolayeva & Tsimring, 1986). Through direct measurement of the airflow, a number of experimental studies conducted in the laboratory have revealed the impact of waves on the momentum and energy transfer between wind and waves. Typical wind–wave conditions include strong (hurricane) winds (Donelan, 2004; Troitskaya *et al.*, 2011*b*, 2012; Sergeev *et al.*, 2017), slow to moderate wind over wind–waves and mechanically generated swells (Veron, Saxena & Misra, 2007; Buckley & Veron, 2016, 2017), and steep (breaking) wave conditions (Reul, Branger & Giovanangeli, 1999, 2008, Troitskaya *et al.*, 2011*a*). While providing substantial insights to the canonical problem of monochromatic waves, many of these studies did not address complex wind–wave systems, especially when the wave field has a broad-band spectrum. One of the main objectives of the present study is to investigate the energy transfer process in complex wind–wave systems.

In the evolution of wave field, nonlinear resonant wave interactions, i.e., the energy transfer among different wave components, play an important role. Resonant interactions occur when certain conditions are satisfied in a group of wave compo-

nents, which is a quadruplet for surface waves in the deep water. Hasselmann (1962, 1963*a*,*b*) derived a kinetic equation, known as the Hasselmann equation, for the calculation of resonant quadruplet wave interactions. The Hasselmann equation quantifies energy transfer due to four-wave interaction in the long term, where the non-resonant nonlinear terms vanish because of the asymptotic form of this kinetic equation. Recently, growing computer capacity has enabled phase-resolving simulations of broad-band waves, where the long-term characteristics of nonlinear wave fields have been studied (e.g. Gagnaire-Renou, Benoit & Badulin, 2011; Annenkov & Shrira, 2013), and the four-wave resonant interaction is found to be crucial in the process. In the present study of wind–wave interactions, we also perform phase-resolving simulations of broad-band waves, which is coupled with wind turbulence simulation, and the four-wave resonant interaction is directly captured in our simulations.

Extensive studies have been performed to develop a universal law on the evolution of wave fields in time and space. Sverdrup & Munk (1947) proposed quantities necessary for the determination of such a law, including significant wave height, significant wave period, wind speed, fetch and duration. For decades, power law has been widely used to relate these quantities to wave growth, where the wind appears to control the wave evolution. In attempts to determine the constants in these power laws, studies have discovered an intrinsic feature of evolving wave fields, namely, self-similarity (see Hasselmann *et al.*, 1973). Badulin *et al.* (2005) conducted a series of numerical experiments, using parameterised models based on field measurements, to show that the wave spectra shapes are independent of the specific forms of wind input and dissipation. The result led to the weakly turbulent law for wave growth in support of the dominant role of nonlinear transfer (Badulin *et al.*, 2007). In a

later study (Gagnaire-Renou *et al.*, 2011), the self-similar parameter in the wave growth law was quantified through numerical simulations for fetch-limited cases. Recently, Zakharov *et al.* (2015) developed a universal law that is entirely associated with intrinsic wave properties such as wave energy, peak wave frequency and peak wavenumber, while the wind speed is excluded from the formula. Their argument is also based on the dominant role of nonlinear interactions. Despite the above efforts in understanding wave field evolution, it is unclear whether the waves would evolve differently if the wind input were evaluated directly from first principles rather than by using parameterised models. Among the parameterised models, there is no consensus about which one is the best. In the operational wave model (The WAVEWATCH III® Development Group, 2016) for instance, there are five different types of wind input source terms provided. In this regard, it would be desirable to examine the nonlinear interactions in the long-term evolution of a wave field using deterministic numerical tools where the wind turbulence is resolved.

The history of numerical study of wind–wave interaction that involves turbulence simulation is relatively short due to the complexity of the physical processes. The wave surface serves as an irregular bottom boundary of the wind field, which increases the complexity of solving the turbulence motions. Moreover, wave evolution involves nonlinear interactions that have a very large time scale, posing great challenges to the computational cost. In early studies, the focus was placed on wind turbulence, and only prescribed monochromatic waves were considered (Sullivan, Mcwilliams & Moeng, 2000; Kihara *et al.*, 2007; Yang & Shen, 2010). Simulations have also been applied to both air and water to study the initial stage of wave growth (Lin *et al.*, 2008; Zonta, Soldati & Onorato, 2015; Campbell, Hendrickson & Liu, 2016), wherein

the time durations of wave evolution in these studies are limited. Some recent studies focused on the interaction between wind and breaking waves with simple wave configurations, including a two-dimensional (2-D) simulation of wind over a narrow-banded breaking wave train (Iafrati *et al.*, 2019), and a three-dimensional simulation of wind over monochromatic breaking waves (Yang, Deng & Shen, 2018*b*).

In the present study, we simulate the coupled wind–wave system based on a computational framework developed by Yang & Shen (2011*a*,*b*) and Yang, Meneveau & Shen (2013). For wind turbulence, we perform large-eddy simulation (LES) on a curvilinear grid that dynamically fits the wave surface motions. For the wave field, we use a high-order spectral method (Dommermuth & Yue, 1987) to capture its nonlinear evolution. The wind LES and wave simulations are dynamically coupled. The wave field evolves for a long duration up to $O(3000)$ peak wave periods to have appreciable change in the wave spectrum. To our knowledge, this is the first wind and wave coupled simulation for such a long duration with the wave phases and turbulence eddies resolved. The analyses in this paper focus on the wave signature in the turbulence wind field, the energy transfer induced by the wind input and nonlinear interactions, and the statistical behaviours of an evolving wind–wave field. Our study aims to contribute to the fundamental understanding of the long-term wind-forced wave field evolution, and to pave the way for future wind–wave studies from the deterministic perspective. The remainder of this section is organized as follows. In § 2.2, we briefly introduce the wind–wave coupled solver and problem setting. In § 2.3-2.5, we examine the numerical results including wind turbulence over waves, wind input to waves, wave statistics, and features of the nonlinear wave field in long-term evolution. Finally, conclusions are given in § 2.6.

2.2 Numerical method and problem setup

2.2.1 LES of wind over surface waves

The turbulent airflow is computed with LES (Yang *et al.*, 2013), in which the air is treated as incompressible and is driven by a mean pressure gradient caused by the geostrophic wind forcing (Calaf, Meneveau & Meyers, 2010). The stratification is neglected. The molecular viscous effect is negligible due to the large Reynolds number in the problem of interest. Following the convention in the literature (e.g. Sullivan *et al.*, 2000, 2008), the streamwise, spanwise and vertical coordinates are denoted by (x, y, z) and equivalently (x_1, x_2, x_3). The governing equations for the airflow are (Pope, 2000)

$$\frac{\partial \widetilde{u}_i}{\partial x_i} = 0, \tag{1}$$

$$\frac{\partial \widetilde{u}_i}{\partial t} + \widetilde{u}_j \frac{\partial \widetilde{u}_i}{\partial x_j} = -\frac{1}{\rho_a}\frac{\partial \widetilde{p}^*}{\partial x_i} - \frac{\partial \tau_{ij}^d}{\partial x_j} - \frac{1}{\rho_a}\frac{\partial p_\infty}{\partial x}\delta_{i1}, \tag{2}$$

where $\widetilde{u}_i (i = 1, 2, 3) = (\widetilde{u}, \widetilde{v}, \widetilde{w})$ is the filtered velocity in which $\widetilde{\ldots}$ denotes the filtered quantity at the grid scale, $\widetilde{p}^*$ is the filtered modified pressure, τ_{ij}^d is the trace-free part of the subgrid-scale (SGS) stress tensor, ρ_a is the density of air and $\partial p_\infty / \partial x$ denotes the mean streamwise pressure gradient that drives the flow. The SGS stress tensor is calculated using the dynamic Smagorinsky model (see Germano *et al.*, 1991; Lilly, 1992).

In the simulation, the filtered Navier–Stokes equations are transformed into the

computational domain

$$\tau = t, \qquad \xi = x, \qquad \psi = y, \qquad \zeta = \frac{z - \tilde{\eta}(x,y,t)}{h - \tilde{\eta}(x,y,t)}, \tag{3}$$

where ξ, ψ, ζ and τ are the space and time coordinates in the computational domain and $\bar{h}$ is the mean domain height with $\overline{\cdots}$ denoting the averaging on the surface of a constant ζ. The coordinate transformation is illustrated in figure 1. As shown in figure 1(b), in the vertical direction, (u, v, p) are defined at the regular grid points, while w is defined on a staggered grid (Yang & Shen, 2011*a*). The only exception is at the bottom and top boundary, where (u, v, w, p) are defined on the same grid points. The Jacobian matrix corresponding to the transformation (3) is

$$\mathbf{J} = \begin{bmatrix} \dfrac{\partial \xi}{\partial x} & \dfrac{\partial \xi}{\partial y} & \dfrac{\partial \xi}{\partial z} \\ \dfrac{\partial \psi}{\partial x} & \dfrac{\partial \psi}{\partial y} & \dfrac{\partial \psi}{\partial z} \\ \dfrac{\partial \zeta}{\partial x} & \dfrac{\partial \zeta}{\partial y} & \dfrac{\partial \zeta}{\partial z} \end{bmatrix} = \begin{bmatrix} 1 & 0 & 0 \\ 0 & 1 & 0 \\ \dfrac{\zeta - 1}{h - \tilde{\eta}} \dfrac{\partial \tilde{\eta}}{\partial x} & \dfrac{\zeta - 1}{h - \tilde{\eta}} \dfrac{\partial \tilde{\eta}}{\partial y} & \dfrac{1}{h - \tilde{\eta}} \end{bmatrix}. \tag{4}$$

Then the governing equations (1)–(2) become:

$$\frac{\partial \tilde{u}}{\partial \xi} + \zeta_x \frac{\partial \tilde{u}}{\partial \zeta} + \frac{\partial \tilde{v}}{\partial \psi} + \zeta_y \frac{\partial \tilde{v}}{\partial \zeta} + \zeta_z \frac{\partial \tilde{w}}{\partial \zeta} = 0, \tag{5}$$

$$\begin{aligned} & \frac{\partial \tilde{u}}{\partial \tau} + \zeta_t \frac{\partial \tilde{u}}{\partial \zeta} + \tilde{u}\left(\frac{\partial \tilde{u}}{\partial \xi} + \zeta_x \frac{\partial \tilde{u}}{\partial \zeta}\right) + \tilde{v}\left(\frac{\partial \tilde{u}}{\partial \psi} + \zeta_y \frac{\partial \tilde{u}}{\partial \zeta}\right) + \tilde{w}\zeta_z \frac{\partial \tilde{u}}{\partial \zeta} \\ = \quad & -\frac{1}{\rho_a}\left(\frac{\partial \tilde{p}^*}{\partial \xi} + \zeta_x \frac{\partial \tilde{p}^*}{\partial \zeta}\right) - \frac{\tau_{11}^d}{\partial \xi} - \zeta_x \frac{\partial \tau_{11}^d}{\partial \zeta} - \frac{\tau_{12}^d}{\psi} - \zeta_y \frac{\partial \tau_{12}^d}{\partial \zeta} - \zeta_z \frac{\partial \tau_{13}^d}{\partial \zeta} - \frac{1}{\rho_a}\frac{\partial p_\infty}{\partial x}, \end{aligned} \tag{6}$$

$$\begin{aligned} & \frac{\partial \tilde{v}}{\partial \tau} + \zeta_t \frac{\partial \tilde{v}}{\partial \zeta} + \tilde{u}\left(\frac{\partial \tilde{v}}{\partial \xi} + \zeta_x \frac{\partial \tilde{v}}{\partial \zeta}\right) + \tilde{v}\left(\frac{\partial \tilde{v}}{\partial \psi} + \zeta_y \frac{\partial \tilde{v}}{\partial \zeta}\right) + \tilde{w}\zeta_z \frac{\partial \tilde{v}}{\partial \zeta} \\ = \quad & -\frac{1}{\rho_a}\left(\frac{\partial \tilde{p}^*}{\partial \psi} + \zeta_y \frac{\partial \tilde{p}^*}{\partial \zeta}\right) - \frac{\tau_{21}^d}{\partial \xi} - \zeta_x \frac{\partial \tau_{21}^d}{\partial \zeta} - \frac{\tau_{22}^d}{\psi} - \zeta_y \frac{\partial \tau_{22}^d}{\partial \zeta} - \zeta_z \frac{\partial \tau_{23}^d}{\partial \zeta}, \end{aligned} \tag{7}$$

$$\begin{aligned} & \frac{\partial \tilde{w}}{\partial \tau} + \zeta_t \frac{\partial \tilde{w}}{\partial \zeta} + \tilde{u}\left(\frac{\partial \tilde{w}}{\partial \xi} + \zeta_x \frac{\partial \tilde{w}}{\partial \zeta}\right) + \tilde{v}\left(\frac{\partial \tilde{w}}{\partial \psi} + \zeta_y \frac{\partial \tilde{w}}{\partial \zeta}\right) + \tilde{w}\zeta_z \frac{\partial \tilde{w}}{\partial \zeta} \\ = \quad & -\frac{1}{\rho_a}\left(\zeta_z \frac{\partial \tilde{p}^*}{\partial \zeta}\right) - \frac{\tau_{31}^d}{\partial \xi} - \zeta_x \frac{\partial \tau_{31}^d}{\partial \zeta} - \frac{\tau_{32}^d}{\psi} - \zeta_y \frac{\partial \tau_{32}^d}{\partial \zeta} - \zeta_z \frac{\partial \tau_{33}^d}{\partial \zeta}, \end{aligned} \tag{8}$$

where the time derivative in the physical space is associated with that in the transformed coordinates by

$$\frac{\partial}{\partial t} = \frac{\partial}{\partial \tau} + \frac{\zeta - 1}{\bar{h} - \tilde{\eta}} \frac{\partial \tilde{\eta}}{\partial t}, \tag{9}$$

and the Laplacian operator in the transformed coordinates is

$$\nabla^2 = \frac{\partial^2}{\partial \xi^2} + \frac{\partial^2}{\partial \psi^2} + 2\zeta_x \frac{\partial^2}{\partial \xi \partial \zeta} + 2\zeta_y \frac{\partial^2}{\partial \psi \partial \zeta} + (\zeta_x^2 + \zeta_y^2 + \zeta_z^2)\frac{\partial^2}{\partial \zeta^2} + (\zeta_{xx} + \zeta_{yy})\frac{\partial}{\partial \zeta}. \tag{10}$$

The upper boundary of the air flow is treated as shear free, while at the bottom boundary a wall model is used to estimate the shear stress at the wave surface (Yang,

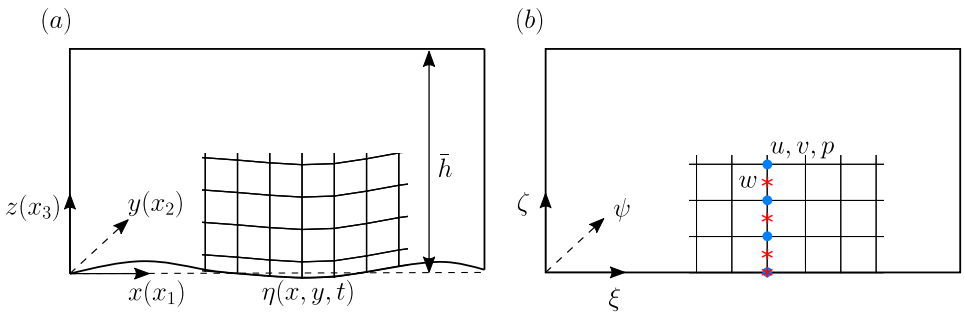

Figure 1: Sketch of the coordinates and grid in: (a) the physical domain and (b) the computational domain. For clarity, we only show part of the grid in each domain and the grid sizes are exaggerated. The grid points defining (u,v,p) and w are denoted by $\bullet$ and $*$, respectively.

Meneveau & Shen, 2014a,b)

$$\tau_{i3}(x,y,t) = -\widehat{\widetilde{U}}_r(x,y,t)\left[\frac{\kappa}{\ln(d_2/z_0)}\right]^2 \times\left[\widehat{\widetilde{u}}_{r,i}(x,y,t)\cos\theta_i+\widehat{\widetilde{u}}_{r,3}(x,y,t)\sin\theta_i\right],\ (i=1,2), \tag{11}$$

where $\widehat{\widetilde{\ldots}}$ denotes quantities filtered at the test-filter scale; $\widehat{\widetilde{U}}_r(x,y,t)$ is the magnitude of the test-filtered air velocity in the horizontal directions relative to the ocean surface; $\kappa=0.41$ is the von Kármán constant; $\widehat{\widetilde{u}}_{r,i}(x,y,t)=\widehat{\widetilde{u}}_i(x,y,d_2,t)-\widehat{\widetilde{u}}_{s,i}(x,y,t)(i=1,2,3)$ are the test-filtered velocity components on the first off-surface grid point relative to the sea-surface velocity $\widehat{\widetilde{u}}_{s,i}(x,y,t)$; and θ_i are the local inclination angles of the surface. The wall model has been applied to the study of wind over waves of short to intermediate lengths (Sullivan *et al.*, 2008; Liu *et al.*, 2010; Yang *et al.*, 2013) as well as wind over swells (Nilsson *et al.*, 2012; Yang *et al.*, 2014a,b). Note that for swell cases, there might be flow inversion very close to the wave surface (see Veron *et al.*, 2007; Buckley & Veron, 2016, 2017) affecting the basic assumption of the wall model and thus its accuracy. The wall model also requires the wave surface

to be well-defined with a small to intermediate steepness such that no violent wave breaking occurs. Otherwise, the resulting wave breaking may affect the wind–wave momentum transfer (e.g., Yang *et al.*, 2018*b*). In general, the logarithmic-law-based wall-layer model is valid when the turbulent eddies are in equilibrium within the grid (Piomelli & Balaras, 2002). This assumption holds in this study because we focus on wind-generated waves instead of swells, and wave breaking is expected to be low at the present wind conditions.

Here we briefly outline the key steps in the numerical scheme. Derivatives are calculated in the horizontal directions using Fourier transform, while those in the vertical direction are calculated using second-order finite difference. The second-order Adam–Bashforth method is used for time advancement. The advection equations of the velocity field are first integrated in time excluding the pressure term. By imposing the divergence-free condition, the pressure field is computed from the Poisson equation. Due to the coordinate transformation, the operator (46) contains nonlinear terms and the Poisson equation is solved in an iteration process. The velocity field is then corrected in the second step with the integration of the pressure term. The initial condition of the wind turbulence is generated by adding random turbulence fluctuations to a logarithmic mean profile, and data for analysis is collected from the fully coupled wind–wave simulation. The details of the numerical schemes for simulating (1) and (2) with the use of (11) and the validations are given in Yang & Shen (2011*a*,*b*) and Yang *et al.* (2013).

2.2.2 High-order spectral method for wave simulation

The high-order spectral (HOS) method is used to simulate the evolution of wave fields denoted by the surface elevation at each position, $\eta(x, y, t)$. In the HOS method, the water motion is treated as a potential flow of an incompressible fluid where the effects of viscosity, turbulence and surface tension are negligibly small. The derivation by Zakharov (1968) shows that the nonlinear wave system is Hamiltonian and can be uniquely determined by the surface elevation $\eta(x, y, t)$ and the surface velocity potential $\Phi^S(x, y, t) \equiv \Phi(x, y, \eta(x, y, t), t)$. The velocity potential $\Phi(x, y, z, t)$ in the domain can be evaluated through $\eta(x, y, t)$ and $\Phi^S(x, y, t)$ up to an arbitrary perturbation order-M. The governing equations are (Dommermuth & Yue, 1987)

$$\begin{aligned} \eta_t &+ \nabla_{\boldsymbol{x}}\eta \cdot \nabla_{\boldsymbol{x}}\Phi^S - (1 + \nabla_{\boldsymbol{x}}\eta \cdot \nabla_{\boldsymbol{x}}\eta) \\ &\times \left[\sum_{m=1}^{M}\sum_{l=0}^{M-m}\frac{\eta^l}{l!}\sum_{n=1}^{N}\Phi_n^m(t)\frac{\partial^{l+1}}{\partial z^{l+1}}\,\Psi_n(\boldsymbol{x}, z)|_{z=0}\right] = 0, \end{aligned} \tag{12}$$

$$\begin{aligned} \Phi_t^S &+ g\eta + \frac{1}{2}\nabla_{\boldsymbol{x}}\Phi^S \cdot \nabla_{\boldsymbol{x}}\Phi^S - \frac{1}{2}(1 + \nabla_{\boldsymbol{x}}\eta \cdot \nabla_{\boldsymbol{x}}\eta) \\ &\times \left[\sum_{m=1}^{M}\sum_{l=0}^{M-m}\frac{\eta^l}{l!}\sum_{n=1}^{N}\Phi_n^m(t)\frac{\partial^{l+1}}{\partial z^{l+1}}\,\Psi_n(\boldsymbol{x}, z)|_{z=0}\right]^2 = -\frac{p_a(\boldsymbol{x}, t)}{\rho_w}, \end{aligned} \tag{13}$$

where $\nabla_{\boldsymbol{x}} \equiv (\partial/\partial x, \partial/\partial y)$ is the gradient operator in horizontal directions, ρ_w is the density of water, $p_a(\boldsymbol{x}, t)$ is the air pressure at the surface, $\Psi_n(\boldsymbol{x}, z) = \exp(i\boldsymbol{k_n} \cdot \boldsymbol{x} + k_n z)$ is the basis function for deep water, and $\Phi_n^m(\boldsymbol{k_n}, t)$ is the corresponding Fourier coefficient of wavenumber $\boldsymbol{k_n}$.

Physically, equations (12) and (13) are, respectively, the kinematic and dynamic

boundary conditions at the wave surface. Given an initial field constructed from realistic waves, these equations can be integrated numerically. The linear terms, e.g., $\nabla_{\boldsymbol{x}}\eta$ and $\nabla_{\boldsymbol{x}}\Phi^S$, are first calculated in the spectral space and then transformed back to the physical space via the fast Fourier transform. The computation of the nonlinear terms, e.g., $\nabla_{\boldsymbol{x}}\eta \cdot \nabla_{\boldsymbol{x}}\Phi^S$, is completed in the physical space at each grid point. The fourth-order Runge–Kutta scheme is used for time integration, thus obtaining the evolution of the nonlinear wave field with the wave phases resolved. The details of the numerical schemes for simulating (12) and (13) and the validations are given in Dommermuth & Yue (1987) and Xiao *et al.* (2013).

The HOS method is a useful tool for simulating wave field evolution with the following advantages: (a) the wind input can be directly incorporated into the wave evolution through the pressure $p_a(\boldsymbol{x}, t)$ at the ocean surface; (b) the maximum order-M can be easily adjusted based on the wave problem; (c) it imposes much less restrictions upon the bandwidth of the wave spectrum compared with the nonlinear Schrödinger equation; and (d) it has a relatively low computational cost for high numerical accuracy, which is a major advantage in large-scale simulations (Wu, 2004). However, the HOS method might fail when there are steep waves or wave breaking, due to the potential flow assumption and the perturbation expansion technique. Therefore, a numerical dissipation model is necessary to mimic the wave energy dissipation due to wave breaking. In the present study, following Xiao *et al.* (2013), we apply an adaptive filter to the surface quantities η and Φ^S

$$\begin{bmatrix} \hat{\eta}_{\mathrm{f}}(\boldsymbol{k}) \\ \hat{\Phi}^S_{\mathrm{f}}(\boldsymbol{k}) \end{bmatrix} = \begin{bmatrix} \hat{\eta}(\boldsymbol{k}) \\ \hat{\Phi}^S(\boldsymbol{k}) \end{bmatrix} G(k; C_1, C_2), \tag{14}$$

where $G(k; C_1, C_2) = \exp[-(k/C_1 k_p)^{C_2}]$ is the filter function, $C_1 = 8$ and $C_2 = 30$ are constants that control the strength of the filter, and $(\hat{\eta}_\mathrm{f}, \hat{\Phi}^S_\mathrm{f})$ are the filtered quantities in the wavenumber space. The corresponding filter in the frequency domain is $G'(f; C_1, C_2) = (4\pi^2 f\sqrt{2f}/g)\exp[-(4\pi^2 f/C_1 g k_p)^{C_2}]$. As shown, G and G' are low-pass filters that dissipate wave energy at short lengthscales and high frequencies. In cases such as steep waves in shallow water studied by Kirby & Kaihatu (1996) and Kaihatu *et al.* (2007), the frequency distribution of the filter was found to have a controlling impact on the spectrum evolution. In the present deep water wave simulation using the filters given above and with the wave steepness set to be small, the impact of dissipation on spectrum evolution is insignificant compared with wind input and nonlinear wave interactions. Also note that while this model can ensure the stability of wave simulation using HOS, it should not be treated as a high-order tool for simulating steep waves. In those conditions, the separation of airflow occurs (Reul *et al.*, 1999, 2008; Buckley & Veron, 2016, 2017), inducing a significant pressure gradient that affects the wind input. The filter would smooth out the wave surface before flow separation. Therefore, the filter is more appropriate to use for applications in wave fields of small to intermediate steepness, which is the case of this study.

2.2.3 Simulation set-up

A typical wave field in the open ocean has wavelengths ranging from a few centimetres to hundreds of meters. Apparently, the computational cost would become far beyond the current computer power to fully resolve such a broad range of fluid motions. It is crucial therefore to choose appropriate dimensions for the wind field and wave field. Since the focus of this study is the evolution of the coupled wind–wave system,

we choose a Joint North Sea Wave Project (JONSWAP) (Hasselmann *et al.*, 1973) spectrum at an early stage of wave growth to initialise the wave simulation

$$E(f) = \frac{\alpha_p g^2}{(2\pi)^4 f^5} \exp\left[-\frac{5}{4}\left(\frac{f}{f_p}\right)^{-4}\right] \gamma_J^{\exp\left[\frac{-(f-f_p)^2}{2\sigma_J^2 f_p^2}\right]}, \tag{15}$$

where $E(f)$ is the frequency spectrum, α_p is the Phillips parameter (Phillips, 1958), f_p is the peak wave frequency, $\gamma_J = 3.3$ and

$$\sigma_J = \begin{cases} 0.07 & f \leq f_p, \\ 0.09 & f > f_p. \end{cases} \tag{16}$$

It is generally assumed that the directional spectrum can be written as the product of the omnidirectional spectrum and a spreading function (Longuet-Higgins, 1963)

$$E(f, \theta) = E(f) D(f, \theta). \tag{17}$$

In this study, we adopt the widely used spreading function $D(f, \theta) = (2/\pi)\cos^2\theta$ to generate the initial wave field. The physical parameters of the wave field are summarised in table 1. In this paper, we use the subscript '0' to indicate quantities of the initial condition unless otherwise specified. For the wave simulation using the HOS method, we set the perturbation order to $M = 3$ because resonant wave interactions (Hasselmann, 1962) can be fully resolved (Tanaka, 2001). Besides, previous studies (Annenkov & Shrira, 2013; Xiao *et al.*, 2013) have suggested that higher order wave statistics including skewness and kurtosis can be accurately captured when the wave nonlinearity is resolved up to the third order in long-term wave evolution. This

α_p	f_{p0} (Hz)	λ_{p0} (m)	c_{p0} (m/s)	T_{p0} (s)
1.4×10^{-2}	0.40	10	3.9	2.5

Table 1: Parameters of the initial JONSWAP wave field, where α_p is the Phillips parameter, f_{p0} is the peak wave frequency, λ_{p0} is the peak wavelength, c_{p0} is the peak wave speed, and T_{p0} is the peak wave period. The subscript '0' denotes the initial condition.

is primarily because the dominant terms of skewness and kurtosis are determined by the wave energy up to the sixth order in terms of wave steepness parameter ϵ (Janssen, 2009). Note that while in principle we could start the simulations with other spectra or even white noise and let the physical wind–waves develop eventually, the computational cost would be too high for the present computing power. For convenience, phase-resolved wave field simulations, such as the ones using the HOS method, often start with an emperical wave spectrum that is already in the similarity form, such as the JONSWAP spectrum. The total energy of the initial spectrum is often deliberately controlled so that the wave steepness and magnitude are within the applicable range. In the present study, where mild waves are of interest, the Phillips parameter α_p that is associated with the total energy is set to a relatively small value (table 1), which is comparable to those in previous studies, e.g., $\alpha_p = 0.0131$ used in Tanaka (2001).

The computational domain size of the wind field is 200m $\times$ 100m $\times$ 100m with a grid number of $256 \times 128 \times 256$. The wave field has the same horizontal dimension of 200m $\times$ 100m with a grid number of 512×256. These parameters are chosen with deliberation. The grid resolution is chosen such that the peak wave length contains enough grid points to resolve most of the energy-containing eddies in the air turbulence. According to Pope (2000), the grid resolution is sufficiently high once

Case	U_{10} (m/s)	u_* (m/s)	c_{p0}/U_{10}	c_{p0}/u_*	$\mathrm{Re}_* = u_*\lambda_{p0}/\nu$	T_s/T_{p0}
WW6	6	0.22	0.66	17.8	1.5×10^5	$3.64{\times}10^3$
WW7	7	0.26	0.56	15.2	1.7×10^5	$3.12{\times}10^3$
WW8	8	0.30	0.49	13.3	2.0×10^5	$2.73{\times}10^3$
WW9	9	0.33	0.44	11.8	2.2×10^5	$2.42{\times}10^3$

Table 2: Parameters of the airflow above wave surface, where U_{10} is the wind speed at 10m above the mean ocean surface, u_* is the air-side friction velocity, Re_* is the Reynolds number based on the wavelength and friction velocity, and T_s is the simulation time duration. The velocity ratios c_{p0}/U_{10} and c_{p0}/u_* are called the 'wave age'. Here, ν is the kinematic viscosity of air.

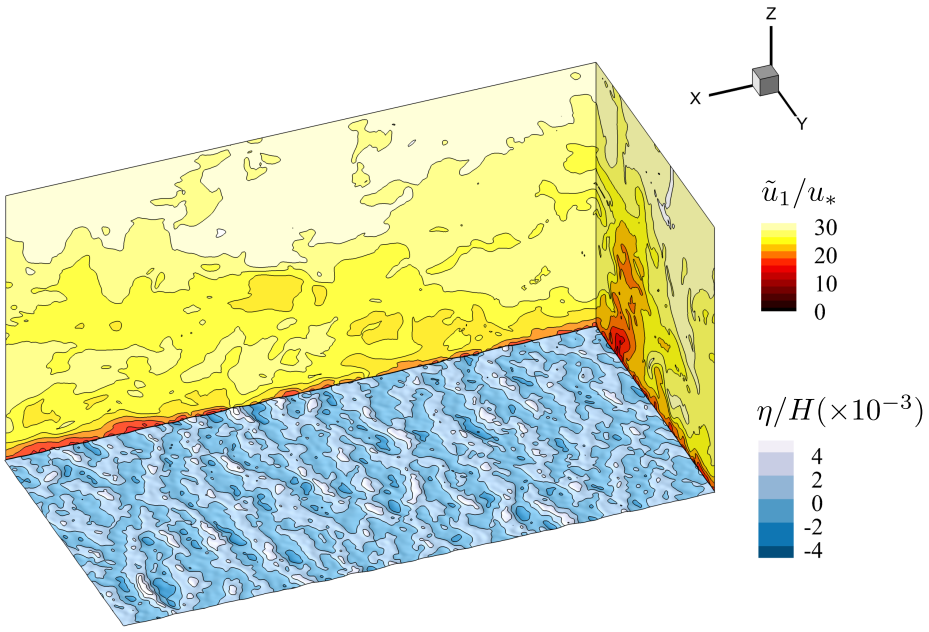

Figure 2: Snapshot of the wind–wave field. Contours plotted in the $x-z$ and $y-z$ planes represent the streamwise wind velocity $\tilde{u}_1$ normalised by the friction velocity u_*. Contours plotted in the $x-y$ plane are the surface elevation η normalised by the mean vertical height of the wind field H.

the bulk ($\sim$80%) turbulence energy is resolved everywhere except for the near-wall region. In the following spectral analysis of the wind turbulence, this requirement is examined in detail. In the wind simulation, we use an evenly spaced grid in all three directions, and the grid size is 0.78 m in horizontal directions and 0.39 m in the vertical direction. As a comparison, some previous studies on wind turbulence over waves have used coarser grids, such as 4.8 m $\times$ 4.8 m $\times$ 1m (Sullivan *et al.*, 2008) and 24.5 m $\times$ 24.5 m $\times$ 7.8 m (Yang *et al.*, 2014*b*). Note that the grid in Sullivan *et al.* (2008) is non-uniform in the vertical direction and the grid size varies from 1 m to 28 m. We would like to emphasise that for the wall-layer model to be valid, the size of the first grid near the wave surface cannot be too fine because the wall-layer model implicitly assumes a Reynolds-averaged inner layer (Piomelli & Balaras, 2002). In the wall-modelled LES, the aerodynamic roughness z_0 is required because the viscous sublayer is not resolved. Here, we choose a typical open-sea value of 2×10^{-4} m following Sullivan *et al.* (2008) and Jiang *et al.* (2016). Since the roughness is used as a property of the mean velocity profile, rather than the instantaneous turbulence field, the fixed value is acceptable when the change in the wind–wave condition is not significant. The parameters of the wind turbulence are summarised in table 2. We choose the four wind speeds to ensure that the wave ages fall into the representative region of wave growth in the real ocean condition while the wave breaking effect is not significant. The total number of the grid points in our wave simulation is eight times the grid number (256×64) in Chalikov, Babanin & Sanina (2014) and Chalikov (2016), slightly smaller than the maximum grid number (1025×257) in Engsig-Karup, Bingham & Lindberg (2009). The time duration of our simulation, $O(3,000T_{p0})$, is nearly ten times that in Chalikov *et al.* (2014) and Chalikov (2016), and much longer

than the maximum simulation time $O(50T_{p0})$ in Engsig-Karup *et al.* (2009). Besides, these studies only involve the wave simulation, while the wind turbulence is not simulated. The present study has wind simulation in addition to the wave simulation, which substantially increases the computational cost. The wave parameters have also been justified by performing independent wave simulations at different grid numbers and perturbation orders (see appendix A).

We initialise the wind field with random fluctuations superposed to a mean logarithmic profile over a flat surface. At the same time, the wave field is initialised using the summation of various wave components in the directional JONSWAP spectrum as stated above, and it first evolves independent of the wind input. After a sufficiently long period of wind and wave simulations separately, the wind turbulence becomes fully developed and the nonlinearity of the wave field has also been fully developed. The wind field and the wave field are then dynamically coupled gradually through a relaxation process, with the wind field providing air pressure to the waves and the wave field in return providing the surface elevation and velocity as the bottom boundary conditions to the wind field above. The data for analysis is collected after the relaxation is completed and the coupled wind–wave field has evolved $O(100T_p)$ to eliminate the relaxation effect. We then continue the fully coupled wind–wave simulations for $O(3,000T_{p0})$ (table 2) to capture the long-term wave dynamics. For illustration purpose, we plot a snapshot of the streamwise velocity for the fully coupled wind–wave field in figure 2.

Case	c_{p0}/U_{10}	c_{p0}/u_*	κ	z_0 (m)
WW6	0.66	17.8	0.371	2×10^{-4}
WW7	0.56	15.2	0.378	2×10^{-4}
WW8	0.49	13.3	0.395	2×10^{-4}
WW9	0.44	11.8	0.418	2×10^{-4}
TE1	0.06	1.4	0.464	9.1×10^{-6}
TE2	0.06	1.6	0.414	4.1×10^{-5}
TE3	0.08	2.5	0.408	5.0×10^{-5}
TE4	0.12	3.7	0.423	1.3×10^{-4}
TE5	0.22	6.5	0.448	1.5×10^{-4}

Table 3: Wave age and features of the wind velocity profile. Here TE1-TE5 denote the wind–wave cases in a tank experiment (Buckley & Veron, 2016, 2017).

2.3 Wind turbulence over waves

The marine atmospheric boundary layer is dynamically coupled with the oceans through the waves, which have spatial variations in both the wavy surface geometry and wave orbital velocity. As a result, the turbulent air flow over waves is more complex than that over a flat wall. In this section, we conduct analyses on the wind turbulence field with an emphasis on the wave effects.

2.3.1 Velocity profile and correlation with waves

The wind velocity profile over waves can be quantified by the von Kármán constant κ and the aerodynamic surface roughness z_0 in the logarithmic region. In table 3, we list our result and that of the recent tank experiments by Buckley & Veron (2016, 2017), in which the wind velocity field near the wave surface is measured at a high resolution. For our simulation result, the mean velocity is calculated by taking the time-averaging of the streamwise velocity. The experimental result is estimated using the data extracted from the figures in Buckley & Veron (2017). While a logarithmic

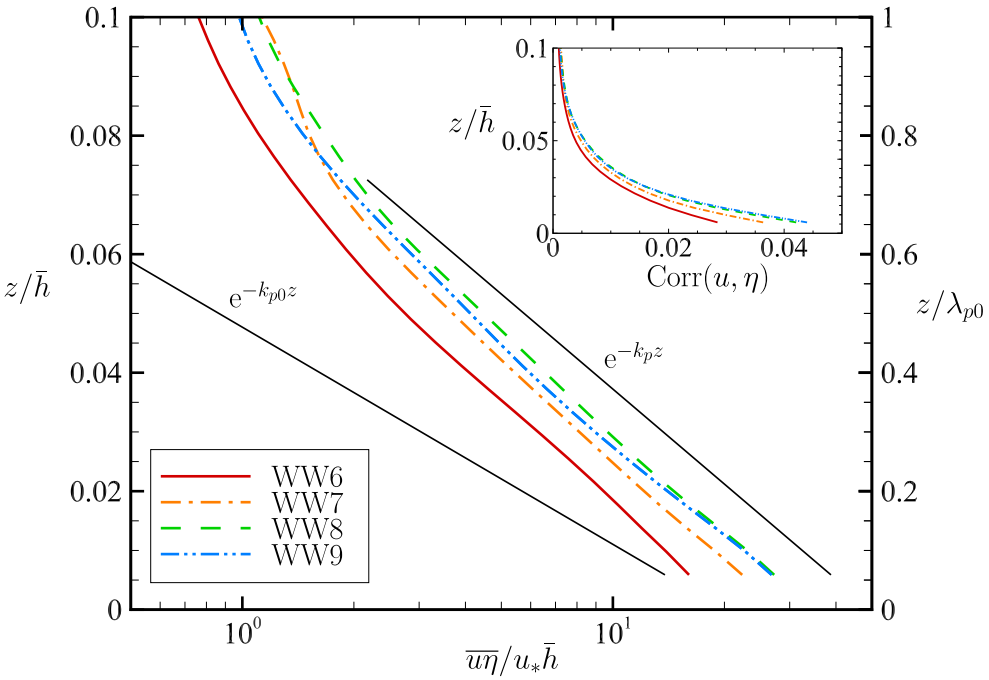

Figure 3: Vertical distribution of the normalised correlation between the wind turbulence velocity and surface wave elevation. The inset is the vertical distribution of the correlation coefficient. Also plotted are two trend lines decreasing exponentially with height, denoted by black solid lines. Here, k_p and k_{p0} are the average peak wavenumber in the corresponding time duration and the peak wavenumber of the initial spectrum, respectively.

region is found in each velocity profile in our simulation cases and the experimental cases (Buckley & Veron, 2016, 2017) and the ranges of parameters are consistent, the values of κ and z_0 vary with different wind–wave conditions, indicating the wave effect on wind turbulence. The wave effect can also be revealed by the correlation between the turbulence velocity and surface elevation as shown in figure 3. We also plot in the inset of figure 3 the correlation coefficient: $\mathrm{Corr}(u,\eta) = \overline{u\eta}/(\overline{uu}\cdot\overline{\eta\eta})^{1/2}$, which decreases monotonically with the height. The results shown here are calculated using data near the end of the simulation. The magnitude of $\overline{u\eta}$, a measure of the wave-coherent motion in the wind turbulence, decreases exponentially with height $\sim \exp(-k_p z)$. The other trend line $\sim \exp(-k_{p0} z)$, which uses the initial peak wavenumber k_{p0}, has appreciable deviation. This result indicates that the wind and wave fields are coupled.

2.3.2 Spectral analysis

We examine the properties of the wind turbulence from the perspective of space–time correlations. Instead of calculating the correlation functions directly, we compute the full wavenumber–frequency spectrum of the streamwise velocity of the turbulence field because it provides a more intuitive approach to investigate turbulence motions of different scales (Pope, 2000). The spectrum is calculated at different vertical heights above the mean wave surface, using numerical data collected at a sampling time interval comparable to the time scale of the smallest resolved eddies in the present simulation. For demonstration purposes, we integrate the full spectrum $F_{11}(\boldsymbol{k},\omega;z)$ along the spanwise wavenumber k_2 to obtain the projected spectrum $F_{11}(k_1,\omega;z)$ on

the $k_1 - \omega$ plane

$$F_{11}(k_1, \omega; z) = \int F_{11}(\boldsymbol{k}, \omega; z) \mathrm{d}k_2, \tag{18}$$

where ω is the angular frequency.

For comparison, we also calculate the wavenumber–frequency spectrum of turbulence over a flat wall using the model proposed by Wilczek & Narita (2012), which is written as

$$F_{11}(\boldsymbol{k}, \omega; z) = F_{11}(\boldsymbol{k}; z) \left[2\pi \langle (\boldsymbol{V} \cdot \boldsymbol{k})^2 \rangle\right]^{-1/2} \exp\left[-\frac{(\omega - \boldsymbol{k} \cdot \boldsymbol{U})^2}{\langle (\boldsymbol{V} \cdot \boldsymbol{k})^2 \rangle}\right], \tag{19}$$

where $\boldsymbol{U} = \boldsymbol{U}(z)$ is the mean velocity at the corresponding height, $\langle \cdot \rangle$ is the averaging operator on a horizontal plane, and $\boldsymbol{V}$ is the velocity of large random eddies with a Gaussian distribution. The wavenumber spectrum $F_{11}(\boldsymbol{k}; z)$ is calculated using 2-D Fourier transform at each height, while the random eddy effect yields $(\boldsymbol{V} \cdot \boldsymbol{k})^2 \approx \langle \tilde{u}'\tilde{u}' \rangle k_1^2 + \langle \tilde{v}'\tilde{v}' \rangle k_2^2$ (Wilczek & Narita, 2012).

The numerical results of the wavenumber–frequency spectrum of wind turbulence over waves (18) and the model results of turbulence over a flat wall (19) are plotted in figure 4. Because the calculation of the spectrum requires data with high resolution in time, we continue the simulation for a period of $33.4T_{p0}$ and output data at a sampling rate of approximately $0.087T_{p0}$. As shown, our simulation results capture the Doppler shift by the mean velocity and demonstrate the Doppler broadening due to turbulence eddies, consistent with the model for turbulence over a flat wall. The frozen turbulence hypothesis (Taylor, 1938) only predicts the Doppler shift effect, and neglects the correlations induced by the turbulence eddies. He, Jin & Yang (2017) pointed out that the inclusion of the random eddy effect in Wilczek & Narita

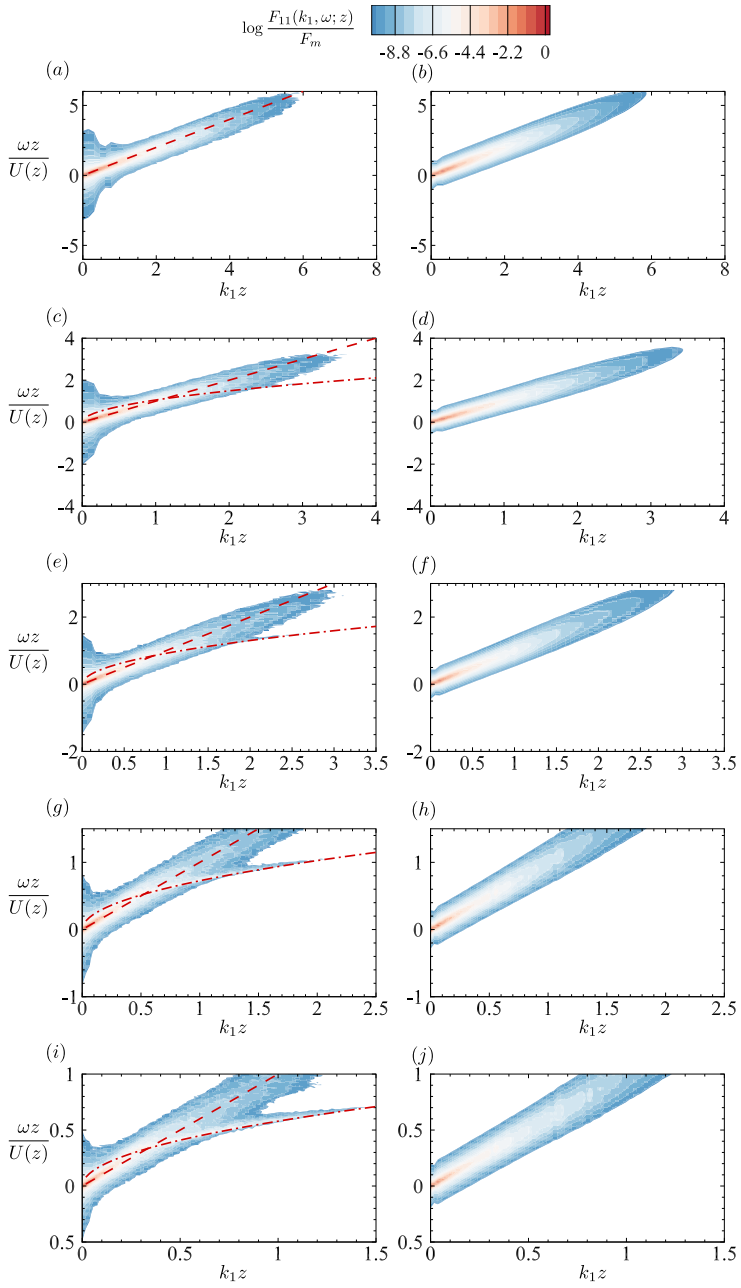

Figure 4: Contours of the wavenumber–frequency spectrum for the streamwise velocity F_{11}, normalised by its maximum value F_m. From top to bottom, the height $z/\lambda_{p0} = \{0.98, 0.51, 0.35, 0.20, 0.12\}$. Left column: simulation results of wind turbulence over waves; right column: prediction of the random-sweeping model for turbulence over a flat wall. In the left column, the Doppler shift $\omega = k_1 U(z)$ is denoted by $- - -$, and the dispersion relation for deep water wave $\omega = \sqrt{g k_1}$ is denoted by $- \cdot -$. Case WW6 is presented here.

(2012)'s model can be seen as a theoretical validation of the elliptic model (He & Zhang, 2006) of spatial–temporal correlation functions. It should be noted that in our results shown in figure 4(a), (c), (e), (g), and (i) the energy at very small wavenumbers ($k < 0.067 \sim 0.080k_{p,0}$) is distributed over a relatively wide region along the frequency axis, which is not seen in the model results of (19). Such a discrepancy is caused by the limitation in the time duration of the numerical data and the computational domain size. For wavenumbers higher than this range, the limitation associated with the domain size does not affect the accuracy of energy spectra. The agreement between our numerical result and the random sweeping model can be seen as evidence that the small scale turbulence is adequately resolved.

The wave signature in the wind turbulence is distinct in our numerical results, as indicated by the dispersion relation of water waves in figure 4(c), (e), (g), and (i). This phenomenon can be qualitatively explained as follows. At the wave surface, where physically there is the no-slip boundary condition for the airflow, the velocity of air equals that of the water, namely the wave orbital velocity. The contours of the wavenumber–frequency spectrum of wind turbulence at the wave surface should then fall precisely along the wave dispersion relation, while the Doppler effect of the mean wind and the effect of large eddies do not exist at the surface. As the vertical height increases, the wave effect decreases, and the mean flow, along with the large eddies, becomes the dominant effect in the turbulence spectrum. Eventually, the wave effect vanishes above a certain height, and our result in figure 4(a) shows that this height is of $O(1/k_p)$, consistent with the concept of wave boundary layer (Sullivan & McWilliams, 2010). For monochromatic waves, the wave effect can be evaluated by extracting the wave-coherent turbulence from the full turbulence via triple decompo-

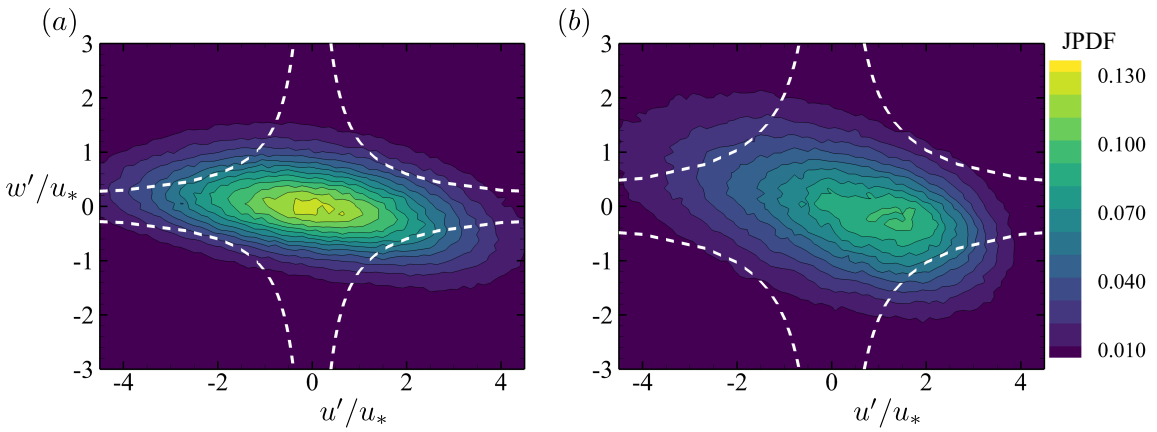

Figure 5: Joint probability distribution function of the normalised velocity fluctuations at the height of (a) $z/\bar{h} = 0.014$ $(z/\lambda_{p,0} = 0.14)$ and (b) $z/\bar{h} = 0.1$ $(z/\lambda_{p,0} = 1.0)$. The white dashed line denotes the constant hole size $H = |u'w'|\,/|\widehat{u'w'}| = 3$. The result of case WW6 is shown.

sition (Buckley & Veron, 2016, 2017). By performing integration on F_{11} in different regions of figure 4(i), we estimate that approximately 90% of the total energy is contained by turbulent motions of length scales greater than 9.2 m. Therefore, our grid size satisfies the requirement of resolving the bulk turbulent energy. Meanwhile, it is sufficiently high to capture the wave signature on turbulence as shown in figure 4. The presence of the wave signature shows that the dynamic coupling between the wind turbulence and wave field involves complex nonlinear processes, which cannot be captured by existing empirical parameterised models. The quantitative analysis of the wave effect on the wind wavenumber–frequency spectrum is beyond the scope of this study and will be investigated in the future.

2.3.3 Quadrant analysis

In this section, we conduct quadrant analysis on the wind turbulence field and explore how waves affect the key turbulence events. First proposed by Wallace, Eckelmann

& Brodkey (1972), the quadrant analysis divides the turbulent velocity fluctuations u' and w' into four parts, each denoting a certain category of turbulence events: $Q1(u' > 0, w' > 0)$, outward interaction; $Q2(u' < 0, w' > 0)$, ejection; $Q3(u' < 0, w' < 0)$, inward interaction; $Q4(u' > 0, w' < 0)$, sweep. As an example, we plot the joint probability distribution function of the normalised velocity fluctuations of case WW6 in figure 5. The difference between the quadrant distributions at two different heights is apparent: close to the wave surface (figure 5a), the quadrant distribution is dominated by the $Q4$ sweep events, whereas far from the wave surface (figure 5b), both $Q2$ and $Q4$ become significant.

To quantify the contributions to the shear stress from different events, we use the method proposed by Lu & Willmarth (1973). Given a positive constant H, we can calculate the conditional statistics $S_{i,H} = \widehat{u'w'}_{i,H}/|\widehat{u'w'}|, (i = 1, 2, 3, 4)$, for all velocity fluctuations satisfying $|u'w'|/|\widehat{u'w'}| \geq H$ in four quadrants. Hereafter, the operator $\widehat{\cdots}_{i,H}$ is the conditional version of the Reynolds averaging operator $\widehat{\cdots}$, and the Reynolds stress $\widehat{u'w'}$ is calculated at different heights. Our definition of $S_{i,H}$ is the same as the one proposed by Raupach (1981), which differs slightly from the original one in Lu & Willmarth (1973) by a factor of the correlation coefficient. The stress fraction $S_{i,H}$ measures the momentum flux contributed by events stronger than the threshold H in the ith quadrant. For each constant value of H, the curve $H = |u'w'|/|\widehat{u'w'}|$ (see the red dashed lines in figure 5) divides each quadrant into two regions: the 'hole' with weak events and the outer region with strong events. The value of H is therefore a measure of the 'hole' size. When $H = 0$, all the events are taken into consideration, and thus we have $\sum_{i=1}^{4} S_{i,H=0} = 1$.

Figure 6 shows the result of the present study compared with the experimental re-

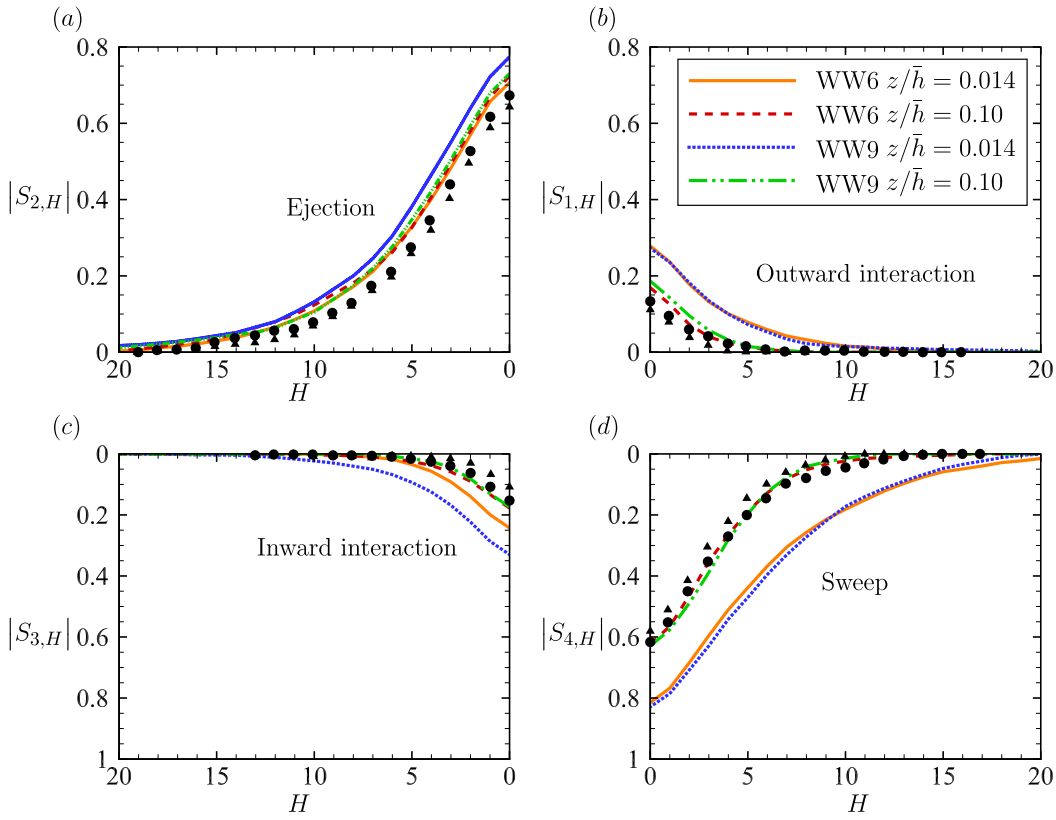

Figure 6: Magnitude of the stress fraction $S_{i,H}(i = 1, 2, 3, 4)$ as a function of the hole size H. The results in Raupach (1981) for a turbulent flow over a smooth surface are denoted by: •, $z/\bar{h} = 0.06$ and ▲, $z/\bar{h} = 0.19$.

sult in a turbulent boundary layer over a smooth surface (Raupach, 1981). For clarity, we present the results of case WW6 and WW9 considering that those of case WW7 and WW8 are not qualitatively different. Our results at $z/\bar{h} = 0.1$ ($z/\lambda_{p,0} = 1.0$) collapse to the smooth surface result (Raupach, 1981) in all four quadrants. At such height, the wave effect becomes negligibly small and the turbulence barely 'feels' its impact. This is in sharp contrast to the near-surface region, where the contributions of various events deviate from the smooth surface result. The near-surface results in case WW6 and WW9 are nearly identical except for some deviations in the contribution of the inward interaction ($Q3$). The contribution from ejection ($Q2$) remains largely unchanged compared with the smooth surface result, whereas the contributions of outward interaction ($Q1$) and sweep ($Q4$) events to the shear stress are greatly enhanced. When $H = 0$, for instance, the contributions of sweep and outward interaction events have increased from 60% to 80%, and 17% to 27%, respectively. Recognizing the challenges in distinguishing the broad-band-wave effect on wind turbulence, we further calculate the quadrant ratio $Q_r = -(Q2 + Q4)/(Q1 + Q3)$ in the same way as in Sullivan *et al.* (2008). Here, Q_r characterizes the ratio of downward momentum flux to upward flux. The value of Q_r is evaluated at $z/\lambda_{p,0} = 0.18$ above the mean surface. For waves along the wind, Q_r obtained from experiments decreases with the wave age, which is expected because the momentum transfer from wind to waves in the downward direction is smaller for longer and faster waves. We find that the quadrant ratio in our simulations is close to the range obtained from experiments (Smedman *et al.*, 1999; Edson *et al.*, 2007; Buckley & Veron, 2016) for the similar wave age. Note that the instantaneous wave ages in all cases slowly increase with time as the coupled system evolves towards the wind–wave equilibrium state,

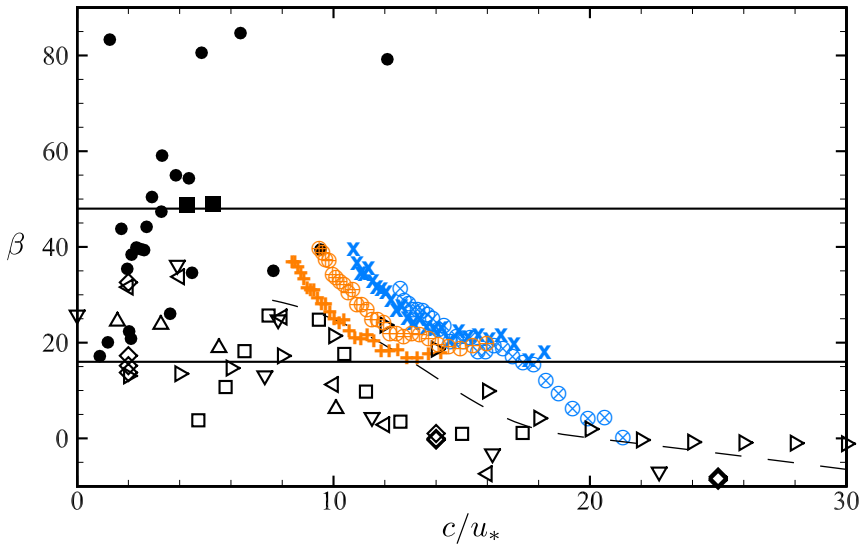

Figure 7: Wave growth rate β as a function of wave age c/u_*. Measurement data are plotted for comparison: ■, Mastenbroek *et al.* (1996); ●, Grare *et al.* (2013). Also plotted are numerical data for comparison: ▽, DNS, Sullivan *et al.* (2000); ▷, RANS (Reynolds-averaged Navier–Stokes), Li *et al.* (2000); ◁, DNS, Kihara *et al.* (2007); ◇, DNS, Yang & Shen (2010); □, LES, Liu *et al.* (2010). The horizontal solid lines are the upper ($\beta = 48$) and lower limit ($\beta = 16$) of the empirical formula by Plant (1982). The growth rate values predicted from Miles (1993) theory are denoted by $- - -$. Present simulation results are denoted by: ⊗, case WW6; ×, case WW7; ⊕, case WW8; +, case WW9.

which is associated with the frequency downshift phenomenon discussed in detail in § 2.5.2.

2.4 Wind input to waves

In this section, we investigate the wind input to quantify the net energy transfer from the wind to the waves. We consider the wave growth rate for a wave component

defined as (see Donelan, 1999; Li, Xu & Taylor, 2000)

$$\beta = \frac{2}{\lambda(ak)^2}\int_0^{\lambda}\frac{p}{\rho_a u_*^2}\frac{\partial\eta}{\partial x}\mathrm{d}x, \tag{20}$$

where p denotes the pressure at the wave surface, and ak is the wave steepness. Here, we have assumed that the wind input is primarily caused by the pressure (normal stress) as it can be shown that the work done by tangential stress is negligibly small (appendix D). For the broad-band wave field, we use the technique proposed by Liu *et al.* (2010) to evaluate β with the pressure and wave fields decomposed in the Fourier space. Suppose one component of the surface elevation is $\eta(x,t) = a_\eta\cos(kx-\omega t+\theta_\eta)$ and the surface pressure is $p(x,t) = a_p\cos(kx-\omega t+\theta_p)$, where a_η and a_p denote the amplitudes in the Fourier space, and θ_η and θ_p the corresponding phases. The wave growth rate is then obtained as $\beta = a_p\sin(\theta_p-\theta_\eta)/a_\eta\rho_a u_*^2$. Note that the magnitude and the phase of the pressure play a decisive role, and their values can only be determined from the wind turbulence simulation.

The wind input can also be quantified by the temporal growth rate (Donelan & Pierson, 1987)

$$\gamma = S_{\lambda/2}\left(\frac{U_{\lambda/2}}{c}-1\right)\left|\frac{U_{\lambda/2}}{c}-1\right|, \tag{21}$$

where $S_{\lambda/2}$ is the coefficient originated from the flow-separation-induced sheltering mechanism proposed by Jeffreys (1925, 1926), and $U_{\lambda/2}$ is the mean wind velocity at the reference height $z = \lambda/2$. Note that the theory of Jeffreys has been known to be inapplicable for wave growth unless the wave breaks (Banner & Melville, 1976). While there is no rigorous criterion for choosing the reference height, $\lambda/2$ (or λ) has been found effective for reducing scattering (Donelan & Pierson, 1987; Donelan, 1999;

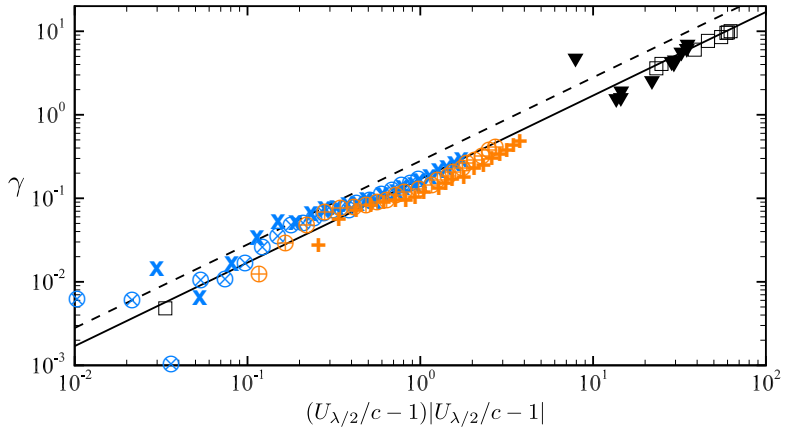

Figure 8: Temporal growth rate γ as a function of $\left(U_{\lambda/2}/c-1\right)\left|U_{\lambda/2}/c-1\right|$. Present simulation results are denoted by: $\otimes$, case WW6; $\times$, case WW7; $\oplus$, case WW8; $+$, case WW9. Also plotted are: $\blacktriangledown$, measurement data, Donelan (1999); $\square$, DNS of monochromatic waves, Yang & Shen (2010). The parameterisations are denoted by lines: ——, $\gamma = 0.17\left(U_{\lambda/2}/c-1\right)\left|U_{\lambda/2}/c-1\right|$, Donelan *et al.* (2006); $-\,-\,-$, $\gamma = 0.28\left(U_{\lambda/2}/c-1\right)\left|U_{\lambda/2}/c-1\right|$, Donelan (1999).

Donelan *et al.*, 2006; Yang & Shen, 2010).

We plot the wave growth rate β as a function of the wave age c/u_* for all four simulation cases in figure 7. The data points correspond to the wave modes in the range of $k_p/2 < k < 2k_p$, where wind turbulence and wave motions are best resolved. The values presented here as well as in figure 8 are the time-averaged result over $100T_{p0}$ using the raw data at the end of the simulation in each case (see table 2). As shown, most data points fall into the range proposed by Plant (1982), which is based on experimental data assuming 'the air-water interface to be well defined'. In other words, the energy dissipation caused by wave breaking was negligibly small for the compiled data (Plant, 1982), which has the same assumption as in the setup of our numerical experiments. For measurements completed in wave tanks (Mastenbroek *et al.*, 1996; Grare *et al.*, 2013), due to the restriction on the tank size, the wavelengths

are small and so are the wave ages. In our four simulation cases of WW6−WW9, as U_{10} increases from 6m/s to 9m/s, the data sets move to the left as the wave age decreases. In each case, the wave growth rates induced by wind input vary among different wave components, where fast (respectively, slow) waves have smaller (respectively, larger) growth rates. The dependence of β on c/u_* is similar to previous numerical results (Li *et al.*, 2000; Sullivan *et al.*, 2000; Kihara *et al.*, 2007; Liu *et al.*, 2010; Yang & Shen, 2010). For those results obtained with DNS, β tends to be underestimated because of the low Reynolds numbers in DNS (Sullivan *et al.*, 2000; Yang & Shen, 2010). In the present LES results, the Reynolds number is realistically large.

Figure 8 shows the variation of the temporal growth rate $\gamma = \beta(u_*/c)^2$ with the inverse wave age function $\left(U_{\lambda/2}/c - 1\right)\left|U_{\lambda/2}/c - 1\right|$. The present result directly calculated from the surface pressure of the turbulent flow is compared with the parameterisations in terms of $U_{\lambda/2}$. It should be noted that, due to the LES used in the present study, we are able to simulate wind–wave interaction at a much larger scale than the previous DNS study of Yang & Shen (2010). Consistent with the previous DNS results for monochromatic waves, the present LES results for broad-band wave fields support the parameterisations proposed by Donelan *et al.* (2006) and Donelan (1999).

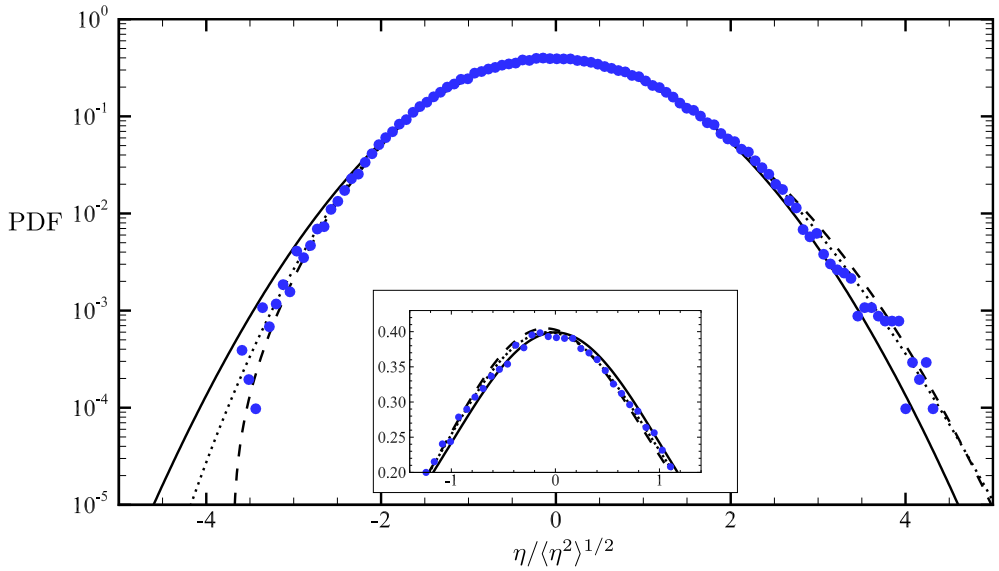

Figure 9: Probability density function (p.d.f.) of the normalised surface elevation $\eta/\bar{\eta^2}^{1/2}$. The embedded figure is a zoom-in view of the peak region. The present result is denoted by •. Also plotted are: the standard Gaussian distribution (——), the second-order approximation by Tayfun (1980) and Socquet-Juglard *et al.* (2005) ($\cdots$), and the Gram-Charlier series (– – –). The result is shown for case WW6.

2.5 Wind-forced wave field

2.5.1 Wave statistics

We first present the statistical properties of the wind–waves, including the probability density function of the surface elevation and other key wave statistics such as skewness and kurtosis. The p.d.f. of the normalised surface elevation, $\eta/\bar{\eta^2}^{1/2}$, is shown in figure 9. Also shown is the standard Gaussian distribution, a second-order approximation (Tayfun, 1980; Socquet-Juglard *et al.*, 2005), and the Gram-Charlier (GC) series, which utilizes the third- and fourth-order statistics to approximate the statistical distribution (see appendix B). The features of the wave statistics are similar for the cases WW6–WW9 in the present study, and we choose case WW6 as an example to present these features in this section. Under linear approximation, the p.d.f. of surface elevation is Gaussian, while our result exhibits a deviation from Gaussian in that the distribution function is tilted, consistent with field measurements (see e.g. Ochi & Wang, 1984). This feature of p.d.f. corresponds to a positive skewness, and is caused by the shape of nonlinear waves with flatter troughs and sharper crests (Holthuijsen, 2007). Our numerical result agrees better with the second-order approximation and the GC series than with the Gaussian distribution, likely due to the higher-order nonlinearity (Agafontsev & Zakharov, 2015). The greatest deviation from the Gaussian distribution occurs at large absolute values of surface elevations that indicate extreme waves associated with strong nonlinearity, similar to laboratory measurement (Onorato *et al.*, 2009). Note that in experiments, it is challenging to obtain a large data set of instantaneous surface elevations with the environment unchanged, and the p.d.f. is usually calculated from the temporal record of wave surface assuming that ensemble

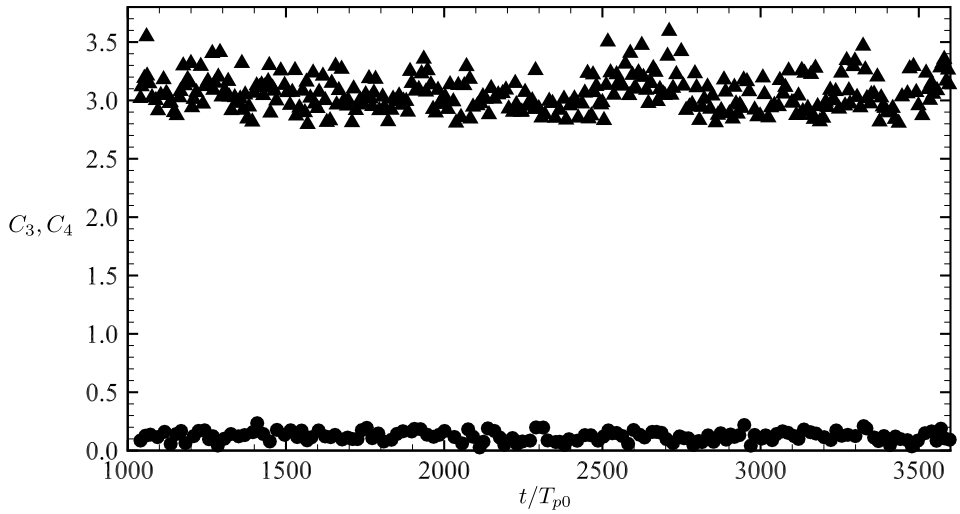

Figure 10: Evolution of the skewness (•) and kurtosis (▲) of the wave field. The result is shown for case WW6.

averages are identical to time averages. In this study, we compute the p.d.f. of surface elevation using the instantaneous data following Tanaka (2001) so that the number of independent observations of the surface elevation is much larger than what is required for an accurate estimate (Tayfun & Fedele, 2007). In this regard, the p.d.f. obtained from our numerical result is useful as a measurement of the statistical behaviour of the irregular wave field.

Skewness and kurtosis are important statistics associated with the physical features of a nonlinear wave field. Specifically, the skewness indicates the deviation of the wave profile from a sinusoidal shape as mentioned above, while the wave kurtosis may suggest the occurrence of extreme waves (Onorato *et al.*, 2009; Xiao *et al.*, 2013). We calculate the skewness C_3 and the kurtosis C_4 from the instantaneous

C_{3+}	C_{3m}	C_{3L}	C_{3A}	$C_{3X,+}$	$C_{3X,m}$	C_{3T}
0.12	0.25	0.17	0.012	–	–	0.20
C_{4+}	C_{4m}	C_{4L}	C_{4A}	$C_{4X,+}$	$C_{4X,m}$	C_{4T}
3.04	3.75	3.08	3.12	3.01-3.20	3.02-3.55	3.10

Table 4: Skewness and kurtosis estimated from different approaches. Subscript + and m respectively denote the time-averages and the maxima of our results (case WW6). Other subscripts are: L, (24) and (25), theoretical prediction of Longuet-Higgins (1963); A, (26) and (27), empirical equations of Annenkov & Shrira (2014); X, numerical result of Xiao *et al.* (2013); T, numerical result of Tanaka (2001).

surface elevation as

$$C_3 = \frac{\overline{\eta^3}}{\left(\overline{\eta^2}\right)^{3/2}}, \tag{22}$$

$$C_4 = \frac{\overline{\eta^4}}{\left(\overline{\eta^2}\right)^{2}}. \tag{23}$$

In nonlinear wave fields, bound waves occur in the form of harmonics, which result in a change in skewness and kurtosis. For narrow-band wave fields, the second-order nonlinear effect of bound waves has been investigated (Longuet-Higgins, 1963) and the statistics are found to be

$$C_{3L} = 3k_p\overline{\eta^2}^{1/2}, \tag{24}$$

$$C_{4L} = 3 + 24k_p^2\overline{\eta^2}. \tag{25}$$

Additionally, the wave statistics may be influenced by resonant interactions (Janssen, 2009; Annenkov & Shrira, 2013). Taking into consideration this dynamic effect, Annenkov & Shrira (2014) computed the skewness and kurtosis for a wide range of

JONSWAP spectrum parameters and directional spreadings. Their result is written in the form of the following empirical formula,

$$C_{3A} = (0.0897 + 0.02\gamma_J^{-0.5})\varepsilon_c, \tag{26}$$

$$C_{4A} = 12.6\gamma_J^{-0.328}\varepsilon_c^2 + 3, \tag{27}$$

where ε_c is a characteristic wave steepness.

The evolution of the skewness and kurtosis is plotted in figure 10. There is a clear difference between our result and the statistics of a standard Gaussian distribution, which has $C_3 = 0$ and $C_4 = 3$ (for more details see appendix B), largely due to the wave nonlinearity. This phenomenon is consistent with the result obtained by Tanaka (2001), who monitored both quantities in simulations of relatively short duration, such as $25T_P$ and $100T_P$. The values of skewness and kurtosis are summarised in table 4, where C_{iL} and C_{iA} $(i = 3, 4)$ are computed using the corresponding parameters of our case set-up. The time-averages (denoted by subscript '+') are an average measure of the non-Gaussianity of the irregular wave field, while the maximum values (denoted by subscript 'm') can serve as an indicator of extreme wave events (Xiao *et al.*, 2013). Again, we present here the result in case WW6 because the skewness and kurtosis of the wave fields share similar behaviours among the different cases WW6–WW9 and their dependence on the wind speed is less significant. The discrepancy among different results in table 4 is primarily due to the different wave properties, including the frequency bandwidth, directional spreading, wave nonlinearity, etc. The frequency bandwidth can affect the probability of extreme wave occurrence, causing an increase in the maximum values of the kurtosis (Xiao *et al.*, 2013). The directional

spreading can also change the value of the high-order statistics (Onorato *et al.*, 2009; Toffoli *et al.*, 2009; Annenkov & Shrira, 2014). The wave nonlinearity has the most prominent impact on the values of the skewness and kurtosis because it is the decisive factor for the deviation from Gaussianity.

2.5.2 Wave evolution

One of the main goals of the present study is to investigate how wave fields would evolve from the deterministic perspective, where both the wind input and nonlinear wave interaction are resolved from first principles. In this section, we focus on the long-term evolution of the wave field, including the frequency downshift phenomenon and wave-based scaling law.

In statistical phase-averaging models, the wave evolution is described by the wave energy balance equation (Komen *et al.*, 1994)

$$\frac{\partial E}{\partial t} + \boldsymbol{C_g} \cdot \nabla_{\boldsymbol{x}} E = S_{tot}, \tag{28}$$

where $\boldsymbol{C_g}$ is the group velocity, and $S_{tot} = S_{nl} + S_{in} + S_{dis}$ is the sum of source terms representing different physical processes, including nonlinear wave interaction S_{nl}, wind input S_{in}, and dissipation S_{dis}. The wave energy balance equation can be written in the wavenumber (k_x, k_y) space or the directional frequency (f, θ) space (see appendix C). While both forms have been used in the literature, the directional form of wave spectrum is used almost exclusively in experiments and the output of the aforementioned operational wave models. Therefore, our numerical results in this section are calculated in the directional frequency space and then presented in the

form of an omnidirectional spectrum.

For the dynamically coupled wind–wave field, separating the nonlinear interactions from wind input and dissipation in the data analysis is difficult (Plant, 1982). We plot the rate of change of the omnidirectional spectrum $\Delta E/\Delta t$ in figure 11. Interestingly, the shapes of $\Delta E/\Delta t$ at different time instants are similar, with a shift in frequency, to that of the S_{nl} calculated with the initial decoupled wind–wave field using the WRT method (Webb, 1978; Tracy & Resio, 1982). The downshift of the peaks of $\Delta E/\Delta t$ can be seen as an indication of the frequency downshift of the wave spectrum. Even in the absence of wind forcing, we would expect the frequency downshift to be present as a consequence of the four-wave interaction except that the overall wave energy growth rate can be different. Note that the frequency downshift may also occur in a narrow-banded wave field accompanied by wave breaking (Tulin & Waseda, 1999). Because of the turbulence generated in wave breaking, in those cases the wave turbulence framework that is based on weak nonlinearity is not valid any more.

We next examine the evolution of the wind-forced wave field through analysis of the wave spectrum. Acknowledging that the nonlinear interactions are dominant locally in the spectral space allows one to further simplify the spectral evolution equation as (Badulin *et al.*, 2005, 2007)

$$\frac{\mathrm{d}E}{\mathrm{d}t} \approx S_{nl}. \tag{29}$$

Meanwhile, because the nonlinear interaction process conserves the total energy, its

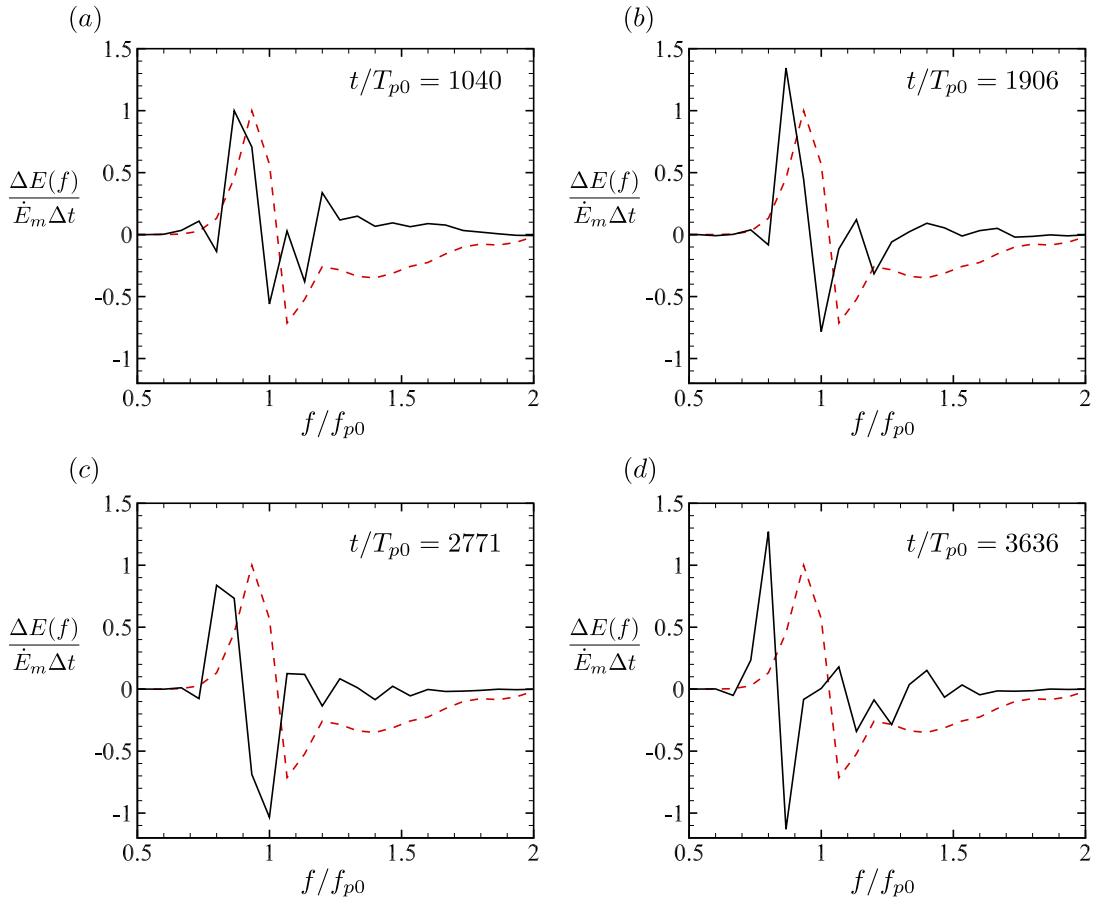

Figure 11: Normalised rate of change of the omnidirectional energy density function (——) at different time instants. Also plotted is the normalised S_{nl} (– – –) calculated for the initial wave spectrum using the WRT method. Here, $\dot{E}_m$ is the maximum value of S_{nl}. The result is shown for case WW6.

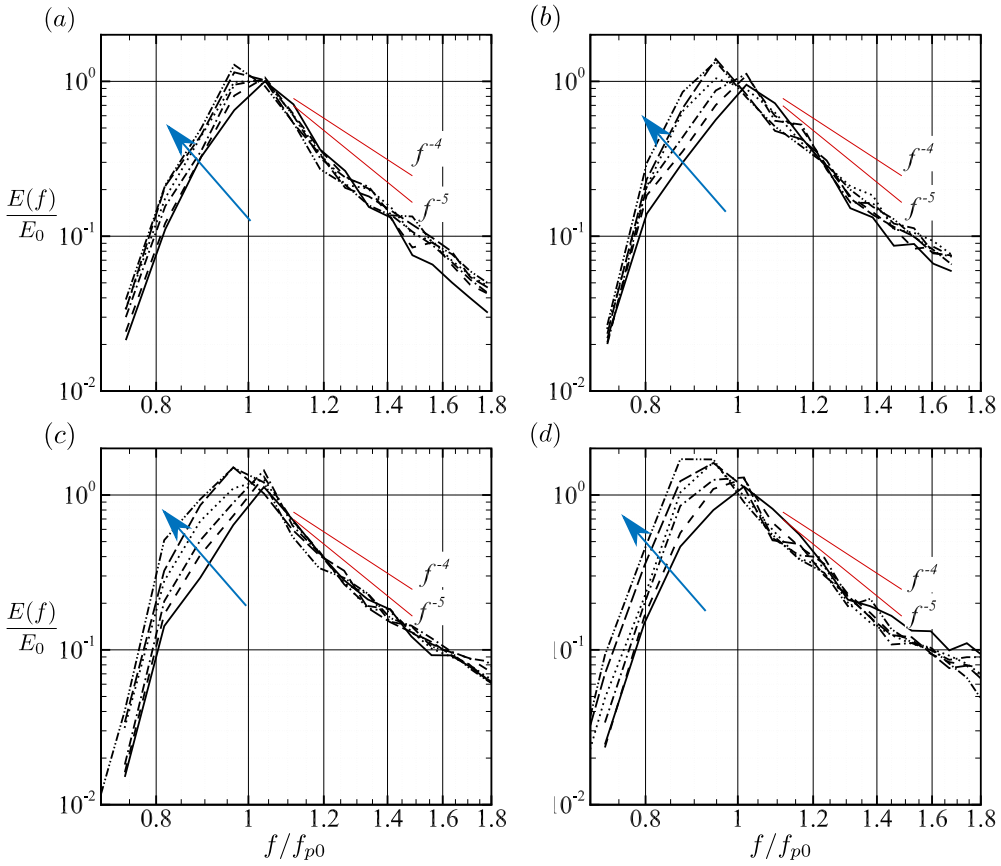

Figure 12: Evolution of the normalised omnidirectional frequency spectrum $E(f)/E_0$, where $E_0 = E(f_{p0})$ is the peak wave energy density of the initial wave field. Figures (a)−(d) correspond to cases WW6 − WW9, respectively. Arrows indicate the direction of time increase. The evolution period is from $t = 1039T_{p0}$ (denoted by ——) to $t = 2424T_{p0}$ (denoted by $-\cdots-$) and the interval between each two consecutive curves is approximately $277T_{p0}$.

corresponding term vanishes in the integral form of equation (28)

$$\int \frac{\mathrm{d}E}{\mathrm{d}t}\mathrm{d}\boldsymbol{k} = \int (S_{in} + S_{dis})\,\mathrm{d}\boldsymbol{k}. \tag{30}$$

In figure 12, we provide the numerical evidence of self-similarity by showing the frequency downshift phenomenon is consistent with field measurements (e.g. Hasselmann *et al.*, 1973). The peak wave frequency sees a downshift due to the nonlinear interactions, whereas the total wave energy increases as a result of wind input. The frequency downshift is essentially the inverse cascade of wave energy because the wave field has not reached a stationary state, whereas for the classic stationary solution of the kinetic equation (Hasselmann, 1962, 1963*a*,*b*), the energy flux to low frequencies is zero (Kats & Kontorovich, 1973, 1974; Zakharov & Zaslavskii, 1982). Figure 12 shows that over the duration of evolution in our simulations, and for the different wind speeds considered, the shape change in the wave spectrum is largely consistent for all the simulation cases.

According to Zakharov *et al.* (2015), the evolution of the wind-forced wave field can be summarised in a concise form

$$\mu^4\nu = \alpha_0^3, \tag{31}$$

where $\mu = E^{1/2}\omega_p^2/g$ is a measure of the wave steepness, $\nu = \omega_p t$ (respectively, $\nu = 2\,|\boldsymbol{k}_p|\,x$) is the dimensionless duration (respectively, fetch) for duration-limited growth (respectively, fetch-limited growth), and α_0 is a universal constant. Here, we use the simulation time to approximate the time duration of wave evolution. In the spirit of converting the time derivative to the space derivative (see Zakharov *et al.*,

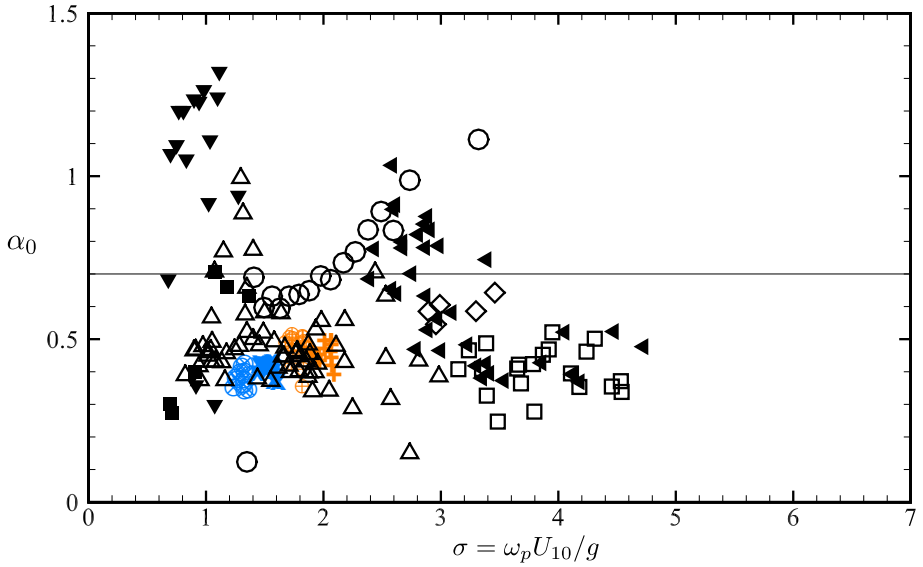

Figure 13: Universal constant α_0 as a function of the normalised peak wave frequency $\sigma = \omega_p U_{10}/g$. The present simulation results are denoted by: $\otimes$, case WW6; $\times$, case WW7; $\oplus$, case WW8; $+$, case WW9. Data compiled by Zakharov *et al.* (2015) are superposed for comparison, including the duration-limited data of: ■, DeLeonibus & Simpson (1972); ▼, Liu (1985); ◀, Hwang & Wang (2004), and fetch-limited data of: □, Burling (1959); ◇, Donelan (1979); ○, García-Nava *et al.* (2009); △, Romero & Melville (2010). Solid line corresponds to the theoretical value proposed by Zakharov *et al.* (2015).

2015), the fetch can be estimated using

$$x = x_0 + \int_0^t C_{\text{charac}} \mathrm{d}t, \tag{32}$$

where x_0 is the fetch of the initial JONSWAP spectrum and $C_{\text{charac}} = \int C_g E \mathrm{d}\boldsymbol{k} / \int E \mathrm{d}\boldsymbol{k}$ is a characteristic wave speed. Note that the choice of C_{charac} is not unique. For instance, one can also choose the peak wave group velocity $C_{\text{charac}} = C_g$. These two definitions are essentially the same when the bandwidth of the wave field is small because the weight function $E/\int E \mathrm{d}\boldsymbol{k}$ approximates a δ function. For the broadband wave field in our study, there is a 10% difference between these two definitions. To determine the dependence of α_0 on fetch and duration, we calculate α_0 using the numerical data and plot in figures 13 its values as the wave field evolves. The data points are calculated from the instantaneous results of the raw data in the entire simulation period (see table 2). As shown, while the values are less than $\alpha_0 \approx 0.7$ proposed by Zakharov *et al.* (2015), the simulation data show much less scattering than the experimental data, and remain almost constant. Our simulation result can be seen as a numerical support to the Zakharov law in the wind–wave region considered. We would like to point out that several factors may contribute to the difference in the value of α_0. The wave growth here is essentially duration-limited rather than fetch-limited. Besides, the choice of the reference fetch in (32) can affect α_0. Another possible explanation for the deviation is that the wave field is not fully self-similar. The same issue may occur when the universal law is validated against laboratory observations (e.g. Toba, 1972) where the wave ages are too small. As discussed by Zakharov *et al.* (2015), this error may be eliminated by using experimental

data obtained from large water tanks at large fetch (e.g. Caulliez, 2013), where the self-similarity of waves has been established.

2.6 Conclusions

In this study, we have used a coupled wind LES and wave HOS computational approaches to study the energy transfer processes in an interacting wind–wave system. The features of the numerical experiments include representative wave ages, broad-band wave field, and long-term wave evolution up to $O(3,000T_{p0})$. The LES and HOS capture a wide range of motions that constitute the most energetic part of wind turbulence and nonlinear waves.

Here, we briefly summarise our main findings. We have calculated the full wavenumber–frequency spectrum of the streamwise wind velocity, which is found to manifest a combined effect of mean flow, large energy-containing eddies, and wave effect that is identified for the first time. As expected, the wave effect on the wind turbulence spectrum is most prominent within a layer of a thickness that is comparable to the peak wavelength. Via quadrant analysis on the wind turbulence field, we have shown that the contributions of sweep and outward interaction events to the shear stress are greatly enhanced by the waves. We have also quantified the energy growth rate for each wave component in the broad-band wave field. The wind input is responsible for the wave energy increase while the energy dissipation related to the wave breaking model is small compared with the wind input (appendix D).

We have examined the statistical properties of the wind–wave field. The probability density function of the surface elevation and high-order wave statistics show a deviation from the Gaussian distribution due to the wave nonlinearity. We have

calculated the total energy change in the wave spectrum. The result shows a positive–negative sign change across the peak frequency. The shape of the energy change is similar to that of the nonlinear interactions, suggesting that nonlinear interactions play a dominant role in the wave field evolution although they have no net contribution to the total wave energy growth. The presence of the nonlinear interactions in the wind-forced wave field results in the frequency downshift phenomenon throughout the numerical experiment, which is observed for the first time in numerical studies when the wind turbulence is resolved using LES. To quantitatively determine the role of the nonlinear interactions, we compute the value of α_0 that arises from the scaling based on intrinsic wave properties. Our numerical result shows that while lower than the recommended value 0.7, α_0 remains largely constant in the evolution period and for the different simulation cases considered. In summary, the present numerical result supports the dominant role of nonlinear interactions in long-term wave evolution, and consequently the universal wave evolution law based on the scaling of wave properties.

Finally, we remark that the deterministic numerical simulation used in this study is a valuable research tool, but is also computationally demanding (for example, a typical case takes about two months to run on a parallel computer using 384 cores). This poses challenges to further increase the evolution period of the wave field with the existing computer power. In the future, with the increase of computer power, when the simulations can be carried out for much longer evolution periods, it would be helpful to provide further quantitative analysis on the wave evolution process when the wave properties, including the total wave energy, peak wavenumber and peak wave frequency, are plotted as functions of time or fetch. These functions

are valuable to the further assessment of the wave turbulence theory (see Badulin *et al.*, 2005; Gagnaire-Renou *et al.*, 2011) and may provide additional support for the significance of nonlinear interactions in the wind-forced wave evolution. The computation framework developed in this study will be useful for such studies. In addition, the energy dissipation of wave breaking is excluded in the analysis of the present study. In the design of our numerical experiments, we deliberately chose relatively weak wind speeds to reduce the impact of wave breaking that cannot be directly resolved by the HOS method due to the potential flow assumption. The complexity of wave breaking requires substantial work in modelling and validation, which is beyond the scope of this study. In future study, it will be beneficial to improve the heuristic wave breaking model in the present numerical tool to better capture the energy dissipation caused by different types of breakers (Melville, 1996; Duncan, 2001, Perlin, Choi & Tian, 2013).

3 Wave Shoaling Effect on Wind–Wave Momentum Flux

3.1 Introduction

Wind–wave interactions, including the momentum transfer between wind and waves in coastal regions, are of great socio–economic significance. For example, in coupled ocean–atmosphere models, the parameterisation of the wind–wave momentum flux serves as the interface to pass the responses between ocean and atmosphere models (see e.g., The WAVEWATCH III® Development Group, 2016). Because the momentum transfer is a key process of the dynamic interactions between the atmosphere and oceans, a deep understanding of this physical process is critical for the assessment of coastal vulnerability for extreme events such as El Niño and La Niña (Barnard *et al.*, 2015).

The sea state, in particular the wave properties, governs the momentum transfer in the wind–wave system. At sea, the aerodynamic surface roughness is widely used to quantify the momentum transfer (e.g. Smith, 1988):

$$z_0 = z_{0,s} + z_{0,w}, \tag{33}$$

where $z_{0,s} = 0.11\nu_a/u_\tau$ represents the viscosity-related surface roughness at a flat plane, and $z_{0,w}$ is associated with the wave-induced form drag. In many sea states, $z_{0,s}$ is negligibly small compared with $z_{0,w}$, i.e., $z_0 \approx z_{0,w}$. The surface roughness is typically expressed as a function of the following parameters: the wind speed at a reference height, such as U_{10} at 10m above sea surface, the wave age, i.e., the ratio of

dominant wave phase speed to the friction velocity c/u_τ, and the wave slope (Edson *et al.*, 2013). Charnock (1955) proposed one of the earliest models for the wave-induced surface roughness $z_{0,w}$:

$$z_{0,w} = \alpha_{ch} \frac{u_\tau^2}{g}, \tag{34}$$

where α_{ch} is the Charnock coefficient. As a rough estimation, α_{ch} can take the value of 0.011 (Smith, 1980, 1988) for the open sea and $0.017 - 0.018$ for coastal waters (Garratt, 1977; Wu, 1980). Apparently, the Charnock coefficient itself is dependent on the sea state and cannot be treated as a constant. In many observations, the Charnock coefficient is found to be a function of the wave age. For example, Smith *et al.* (1992) reported the surface roughness in a cubic function of the friction velocity:

$$z_0 = 0.48 \frac{u_\tau^3}{g c_p}, \tag{35}$$

where c_p is the wave phase speed at the wave spectrum peak. An example of wave-slope-based roughness modelling can be found in Taylor & Yelland (2001):

$$\frac{z_0}{H_s} = A_1 \left(\frac{H_s}{\lambda_p} \right)^{B_1}, \tag{36}$$

where A_1 and B_1 are empirical constants obtained by fitting field data, H_s is the significant wave height, and λ_p is the wavelength at the wave spectrum peak. The modelling of the surface roughness is far from complete and faces many challenges. First of all, there is no consensus on the dependent variables as mentioned above. Even for models using the same variable, say, the wave age, there exists notable dif-

ference among the models from different observations. It might be questionable to use a single dependent variable such as equation (35), where the Charnock coefficient is a function of u_τ. As pointed out by Smith *et al.* (1992), this self-scaling problem may lead to spurious result, and might be mediated by using the combination with other parameters, such as the significant wave height. Moreover, in some early parameterisations, the reference speed U_{10} is commonly used for the convenience of comparison. Hwang (2004) has argued that $U_{\lambda/2}$, or equivalently U_λ, can reflect the dynamic influence of waves on the wind flow more faithfully. It is unlikely that further improvement can be obtained by only adjusting the coefficients in wind velocity dependent models without the wave information (Edson *et al.*, 2013), and including wave age or wave slope is therefore a necessity for modelling.

To date, the majority of the existing parameterised models are for momentum flux in the open sea, without taking into consideration the impact of water depth in coastal regions. The existing open sea roughness models cannot be directly applied to the coastal regions. There has been measurement evidence that the wind–wave momentum transfer in coastal regions is appreciably higher than that in the open sea (Geernaert, Katsaros & Richter, 1986; Geernaert, 1990). In an early observation from a fixed platform, Mahrt *et al.* (1996) calculated the drag coefficient (for its definition see appendix E) at various wind speeds and found that its values are in general higher in short-fetch cases compared with long-fetch cases. In their study, the fetch was determined by the wind direction because the platform was fixed. In another coastal experiment reported by Oost *et al.* (2001), the drag coefficients were found to be higher than the open ocean value reported by Smith (1980). The authors explained this difference by pointing out that the mean wave age in Smith (1980) was 25, while

in their experiment it was $1.1 \sim 1.5$. Using data acquired in a surf zone, Shabani, Nielsen & Baldock (2014) calculated the drag coefficient and surface roughness, and compared their result with a collection of existing open sea parameterisations. They found increases in the drag coefficient and the normalised surface roughness in the surf zone. Zhao *et al.* (2015) measured coastal momentum flux and observed a higher drag coefficient when the wind speed fell into the range of $10\text{m/s} < U_{10} < 30\text{m/s}$. They developed an empirical model using curve fitting and incorporated the change in wave steepness caused by water depth variation. Ortiz-Suslow *et al.* (2015) measured the wind turbulence at a tidal inlet and calculated the drag coefficient using the Smith (1988) method. The average ratio of the observed coastal drag coefficient to the open sea value was found to be around 2.5. Despite the experimental evidence, the present understanding of the mechanisms that cause the increased coastal momentum flux remains inconclusive due to the complexity in the physical processes. It is believed by some researchers that the change in the wave age is critical in causing the increased momentum flux (Mahrt *et al.*, 1996; Shabani *et al.*, 2014; Ortiz-Suslow *et al.*, 2015). Also, in the parameterised model of Zhao *et al.* (2015) mentioned above, the wave steepness variation originates from an idealised wave shoaling scenario. Therefore, we expect that wave shoaling, which can lead to the changes in wave speed and steepness, would impact the wind–wave momentum transfer.

Wave shoaling is a phenomenon that occurs when waves propagate from open sea to coastal region, causing a change in wave properties. When the bottom slope is gentle, the wave shoaling is analogous to light propagation through slowly-varying medium in optics. In fact, the knowledge of ocean wave shoaling has inspired theoretical and experimental studies of the similar phenomenon in optical fibre (e.g.,

Wabnitz, 2013; Wetzel *et al.*, 2015). For monochromatic waves propagating over bathymetry with parallel contours, the shoaling process can be quantified by the shoaling coefficient (Dean & Dalrymple, 1991, 2001), a function of the ratio between the wave phase speed in the coastal region and that in the open sea. For a general broadband wave field, however, it is challenging to obtain an analytical solution even for a simple bathymetry. Besides shoaling, refraction could occur for waves propagating obliquely to the constant water depth direction. Bragg resonance is another physical process in the coastal region, when surface waves interact with bottom ripples (Liu & Yue, 1998; Ardhuin & Herbers, 2002). Nonlinear resonance interaction among three waves becomes possible, because the dispersion relation in finite water depth is different from that in the open sea, and the resonant conditions can be satisfied (see e.g., Nazarenko, 2011). To capture the dynamics of waves in coastal regions, various mathematical models have been developed (e.g., Dingemans, 1997), including the mild slope equation models, Boussinesq-type equations, non-hydrostatic models, etc. Mild slope equation models (e.g., Porter, 2003; Kirby, 1986) were developed assuming that the bottom slope is small and the velocity potential can be expanded into Taylor series (Young, 1999). The Boussinesq-type equations (e.g., Kirby, 1986; Chamberlain & Porter, 1995; Porter & Staziker, 1995) are based on coastal region assumption, and the vertical coordinate is eliminated (Dingemans, 1997). Both the mild slope models and Boussinesq-type models rely on the assumption of slowly-varying bathymetry (Belibassakis & Athanassoulis, 2002). Non-hydrostatic models (Casulli & Stelling, 1998; Stansby & Zhou, 1998; Zijlema, Stelling & Smit, 2011; Wei & Jia, 2014) are based on the Reynolds-averaged Navier–Stokes (RANS) equations, and the free surface motion is tracked by a single value function of horizontal coordinates and

time. Due to the nature of the non-hydrostatic models, they are more appropriate for modeling non-dispersive waves (e.g., infragravity waves, see Rijnsdorp, Ruessink & Zijlema, 2015), and less applicable for modeling a complete coastal wave field that is a composite of both long non-dispersive and short dispersive waves (Munk, 1949; Tucker, 1950).

In this study, we design a series of numerical experiments to assess the impact of wave shoaling on the wind–wave momentum transfer in the coastal region. The simulations address the critical need of resolving the wind turbulence and capturing the wave dynamics, as suggested by the field studies in literature. The numerical tools used here include a wind–wave coupling scheme (Yang & Shen, 2011*b*; Yang, Meneveau & Shen, 2014*a*,*b*), a dynamic sea surface roughness model (Yang, Meneveau & Shen, 2013), and a wave shoaling model (Davis *et al.*, 2014). To the best of our knowledge, this is the first comprehensive simulation-based study of its kind focusing on the coastal wind–wave momentum transfer, whereas in previous numerical studies that involve the investigation of momentum transfer (e.g., Sullivan, Mcwilliams & Moeng, 2000; Yang & Shen, 2010; Druzhinin, Troitskaya & Zilitinkevich, 2012; Sullivan, McWilliams & Patton, 2014), the waves are all in open seas. In this paper, the analyses focus on the change in wind turbulence associated with the shoaling of monochromatic waves, the nonlinear broadband wave shoaling process, and the wind turbulence over the shoaling broadband waves. The remaining of this paper is organized as follows. In § 3.2, we report the mechanistic study on wind over monochromatic waves. In § 3.3, we present the study on wind over broadband waves. Finally, discussions and conclusions are given in § 3.4.

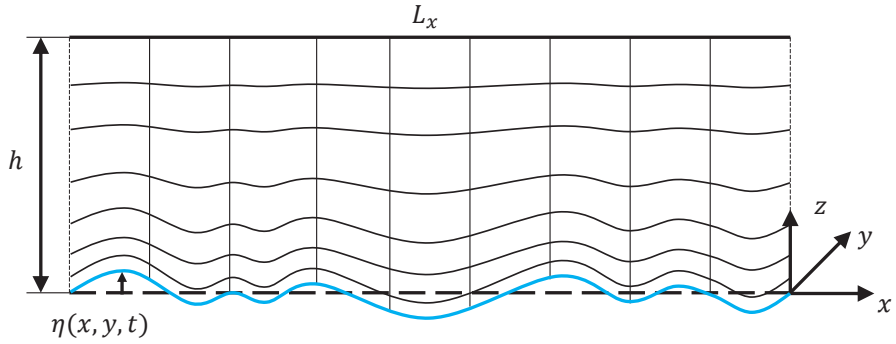

Figure 14: Sketch of the boundary-fitted grid in the (x, z)-plane. Here h is the mean domain height, L_x is the domain length in x-direction, and $\eta(x, y, t)$ is the wave surface elevation.

3.2 Wind over monochromatic waves

3.2.1 Problem setup and numerical method

In the field, the wave shoaling process occurs over a relatively long distance and it is impractical to perform LES for the entire domain of the wave shoaling process. We choose our computational domains separately at open sea and coastal region, assuming that the dynamics of wind turbulence, waves and wind–wave interactions change slowly in space. In each case, the wind turbulence field interacts locally with the wave field (Toba, 1972), while the spatial change of the wind–wave field associated with the wave shoaling is realised by varying parameters among different cases.

We first conduct a mechanistic study on the momentum transfer between wind and monochromatic waves and compare the results between open sea and coastal region cases. The wind turbulence is simulated using wall-resolved LES while the bottom boundary condition for the wind field simulation is a prescribed monochromatic wave. We use a mean pressure gradient caused by the geostrophic wind forcing (Calaf,

Meneveau & Meyers, 2010) to drive the wind turbulence. The key assumptions of the wind field include incompressible air and neutrally stratified condition. Let x, y, and z denote the streamwise, spanwise, and vertical coordinates, respectively, then the governing equations can be written as:

$$\frac{\partial \widetilde{u}_i}{\partial x_i} = 0, \tag{37}$$

$$\frac{\partial \widetilde{u}_i}{\partial t} + \widetilde{u}_j \frac{\partial \widetilde{u}_i}{\partial x_j} = -\frac{1}{\rho_a}\frac{\partial \widetilde{p}^*}{\partial x_i} - \frac{\partial \tau_{ij}^d}{\partial x_j} + \nu_a \frac{\partial^2 \tilde{u}_i}{\partial x_j \partial x_j} - \frac{1}{\rho_a}\frac{\partial p_\infty}{\partial x}\delta_{i1}, \tag{38}$$

where $\widetilde{u}_i (i = 1, 2, 3) = (\widetilde{u}, \widetilde{v}, \widetilde{w})$ is the filtered velocity in LES with $(\widetilde{\ldots})$ denoting the filtered quantity at the grid scale, $\widetilde{p}^*$ is the filtered modified pressure, τ_{ij}^d is the trace-free part of the subgrid-scale (SGS) stress tensor, ρ_a is the density of air, ν_a is the kinematic viscosity of air, and $\partial p_\infty / \partial x$ denotes the mean streamwise pressure gradient that drives the flow. In the present study, the SGS stress tensor is calculated using the dynamic Smagorinsky model (see Germano *et al.*, 1991; Lilly, 1992).

The filtered Navier–Stokes equations (37)–(38) are transformed into the computational domain, which is defined by:

$$\tau = t, \qquad \xi = x, \qquad \psi = y, \qquad \zeta = \frac{z - \tilde{\eta}(x, y, t)}{h - \tilde{\eta}(x, y, t)}, \tag{39}$$

where ξ, ψ, ζ, and τ are the space and time coordinates in the computational domain, and h is the mean domain height. This transformation corresponds to a wave-following boundary-fitted grid (see figure 14). The Jacobian matrix corresponding to

the transformation (39) is:

$$\mathbf{J} = \begin{bmatrix} \dfrac{\partial \xi}{\partial x} & \dfrac{\partial \xi}{\partial y} & \dfrac{\partial \xi}{\partial z} \\ \dfrac{\partial \psi}{\partial x} & \dfrac{\partial \psi}{\partial y} & \dfrac{\partial \psi}{\partial z} \\ \dfrac{\partial \zeta}{\partial x} & \dfrac{\partial \zeta}{\partial y} & \dfrac{\partial \zeta}{\partial z} \end{bmatrix} = \begin{bmatrix} 1 & 0 & 0 \\ 0 & 1 & 0 \\ \dfrac{\zeta - 1}{h - \tilde{\eta}} \dfrac{\partial \tilde{\eta}}{\partial x} & \dfrac{\zeta - 1}{h - \tilde{\eta}} \dfrac{\partial \tilde{\eta}}{\partial y} & \dfrac{1}{h - \tilde{\eta}} \end{bmatrix}. \tag{40}$$

Then the governing equations (37)– (38) become:

$$\frac{\partial \tilde{u}}{\partial \xi} + \zeta_x \frac{\partial \tilde{u}}{\partial \zeta} + \frac{\partial \tilde{v}}{\partial \psi} + \zeta_y \frac{\partial \tilde{v}}{\partial \zeta} + \zeta_z \frac{\partial \tilde{w}}{\partial \zeta} = 0, \tag{41}$$

$$\begin{aligned} &\frac{\partial \tilde{u}}{\partial \tau} + \zeta_t \frac{\partial \tilde{u}}{\partial \zeta} + \tilde{u}\left(\frac{\partial \tilde{u}}{\partial \xi} + \zeta_x \frac{\partial \tilde{u}}{\partial \zeta}\right) + \tilde{v}\left(\frac{\partial \tilde{u}}{\partial \psi} + \zeta_y \frac{\partial \tilde{u}}{\partial \zeta}\right) + \tilde{w}\zeta_z \frac{\partial \tilde{u}}{\partial \zeta} \\ =& -\frac{1}{\rho_a}\left(\frac{\partial \tilde{p}^*}{\partial \xi} + \zeta_x \frac{\partial \tilde{p}^*}{\partial \zeta}\right) - \frac{\tau_{11}^d}{\partial \xi} - \zeta_x \frac{\partial \tau_{11}^d}{\partial \zeta} - \frac{\tau_{12}^d}{\psi} - \zeta_y \frac{\partial \tau_{12}^d}{\partial \zeta} - \zeta_z \frac{\partial \tau_{13}^d}{\partial \zeta} \\ &+ \nu_a \nabla^2 \tilde{u} - \frac{1}{\rho_a}\frac{\partial p_\infty}{\partial x}, \end{aligned} \tag{42}$$

$$\begin{aligned} &\frac{\partial \tilde{v}}{\partial \tau} + \zeta_t \frac{\partial \tilde{v}}{\partial \zeta} + \tilde{u}\left(\frac{\partial \tilde{v}}{\partial \xi} + \zeta_x \frac{\partial \tilde{v}}{\partial \zeta}\right) + \tilde{v}\left(\frac{\partial \tilde{v}}{\partial \psi} + \zeta_y \frac{\partial \tilde{v}}{\partial \zeta}\right) + \tilde{w}\zeta_z \frac{\partial \tilde{v}}{\partial \zeta} \\ =& -\frac{1}{\rho_a}\left(\frac{\partial \tilde{p}^*}{\partial \psi} + \zeta_y \frac{\partial \tilde{p}^*}{\partial \zeta}\right) - \frac{\tau_{21}^d}{\partial \xi} - \zeta_x \frac{\partial \tau_{21}^d}{\partial \zeta} - \frac{\tau_{22}^d}{\psi} - \zeta_y \frac{\partial \tau_{22}^d}{\partial \zeta} - \zeta_z \frac{\partial \tau_{23}^d}{\partial \zeta} + \nu_a \nabla^2 \tilde{v}, \end{aligned} \tag{43}$$

$$\begin{aligned} &\frac{\partial \tilde{w}}{\partial \tau} + \zeta_t \frac{\partial \tilde{w}}{\partial \zeta} + \tilde{u}\left(\frac{\partial \tilde{w}}{\partial \xi} + \zeta_x \frac{\partial \tilde{w}}{\partial \zeta}\right) + \tilde{v}\left(\frac{\partial \tilde{w}}{\partial \psi} + \zeta_y \frac{\partial \tilde{w}}{\partial \zeta}\right) + \tilde{w}\zeta_z \frac{\partial \tilde{w}}{\partial \zeta} \\ =& -\frac{1}{\rho_a}\left(\zeta_z \frac{\partial \tilde{p}^*}{\partial \zeta}\right) - \frac{\tau_{31}^d}{\partial \xi} - \zeta_x \frac{\partial \tau_{31}^d}{\partial \zeta} - \frac{\tau_{32}^d}{\psi} - \zeta_y \frac{\partial \tau_{32}^d}{\partial \zeta} - \zeta_z \frac{\partial \tau_{33}^d}{\partial \zeta} + \nu_a \nabla^2 \tilde{w}, \end{aligned} \tag{44}$$

where the time derivative in the physical space is associated with that in the transformed coordinates by:

$$\frac{\partial}{\partial t} = \frac{\partial}{\partial \tau} + \frac{\zeta - 1}{h - \tilde{\eta}} \frac{\partial \tilde{\eta}}{\partial t}, \tag{45}$$

and the Laplacian operator in the transformed coordinates is:

$$\nabla^2 = \frac{\partial^2}{\partial\xi^2} + \frac{\partial^2}{\partial\psi^2} + 2\zeta_x\frac{\partial^2}{\partial\xi\partial\zeta} + 2\zeta_y\frac{\partial^2}{\partial\psi\partial\zeta} + (\zeta_x^2 + \zeta_y^2 + \zeta_z^2)\frac{\partial^2}{\partial\zeta^2} + (\zeta_{xx} + \zeta_{yy})\frac{\partial}{\partial\zeta}. \quad (46)$$

The numerical scheme for solving the above equations was originally developed by Yang & Shen (2011*a*) and has been extensively validated for classical wind–wave problems (Yang & Shen, 2011*b*). It has been applied to the study of the sea surface roughness model (Yang *et al.*, 2013), offshore wind energy (Yang *et al.*, 2014*a*,*b*), and the air–sea exchange of scalar quantities (Yang & Shen, 2017). Here we briefly outline the key steps in the numerical scheme. Derivatives are calculated in the horizontal directions using Fourier transform, while those in the vertical direction are calculated using second-order finite difference. The second order Adam–Bashforth method is used for time advancement. The initial condition of the wind turbulence is generated by adding random turbulence fluctuations to a logarithmic mean profile. To expedite the simulation process, we start the simulation by setting the bottom boundary to a flat surface and then the wave kinematics are incorporated into the boundary condition through a relaxation process. Then the simulation continues and we collect data after the wind turbulence becomes fully developed.

The computational parameters are summarised in table 5. The setup is designed to include the sea states of a monochromatic shoaling wave when it is in the open sea (case OS05) and the coastal region (case CR14), respectively. Here we choose the dimensionless water depth kd in case CR14 to be 0.42, which is close to the shallow water wave limit $\pi/10$ (Dean & Dalrymple, 1991; Young, 1999). A third case OS14 is designed as a controlled experiment to investigate the impact of wave age

Case	c/u_τ	kd	λ/h	ka	$\mathrm{Re}_\lambda = u_\tau\lambda/\nu$	L_x, L_y, L_z	$N_x \times N_y \times N_z$	$\left(\Delta x^+, \Delta y^+, \Delta z^+_{\mathrm{min}}\right)$
OS05	19.3	∞	1.0	0.05	5000	$2h, h, h$	$256 \times 384 \times 384$	$(58, 20, 0.62)$
CR14	7.7	0.42	0.4	0.14	2000	$2h, h, h$	$256 \times 384 \times 384$	$(58, 20, 0.62)$
OS14	19.3	∞	1.0	0.14	5000	$2h, h, h$	$256 \times 384 \times 384$	$(58, 20, 0.62)$

Table 5: Simulation parameters for the wall-resolved LES cases for monochromatic waves. Here, c/u_τ is the wave age, i.e., the ratio of wave phase velocity to friction velocity; kd is the dimensionless water depth normalised by the wavenumber k; λ/h is the ratio of wavelength λ to the domain height h; ka is the wave steepness; Re_λ is the wavelength-based Reynolds number; Δx^+ and Δy^+ are the effective grid size in wall unit after 2/3 dealiasing in horizontal directions; $\Delta z^+_{\mathrm{min}}$ is the minimum vertical grid spacing in wall unit at the wave surface.

and wave steepness. We would like to point out that the wave parameters in case CR14 are calculated from the shoaling theory for monochromatic waves (Dean & Dalrymple, 1991). We first evaluate the wavenumber and the wave amplitude in the coastal region by conservation of wave frequency and wave energy flux, respectively. Then the dimensionless wave age and steepness are obtained. The details are given in appendix F. Note that here we consider the linear wave kinematics and wave shoaling process. At the current settings, the error in the wave orbital velocity due to the linear approximation is less than 2%.

To cope with the challenge of resolving the fluid motions in the viscous sublayer in wall-resolved LES, we modify the viscosity so that computational cost is affordable. The Reynolds number Re_λ defined by the wavelength is listed in table 5. The corresponding Reynolds number $\mathrm{Re}_h = u_\tau h/\nu$ is 5000, sufficiently high to capture the important turbulence features (such as scale separation) in high-Reynolds-number flows (Smits, McKeon & Marusic, 2011). The choice of domain size ensures that the wave effect on turbulence is captured in the wave boundary layer up to the vertical height of $O(\lambda)$ from the mean wave surface (Sullivan & McWilliams, 2010). The grid size at the water surface satisfies the requirement to resolve inner-layer eddies (Piomelli & Balaras, 2002). The total duration for turbulence development is approximately 1.2×10^5 viscous time units (i.e., time normalised by ν/u_τ^2). We then collect data for analyses at a sampling rate of 61 viscous time units for 1.8×10^4 viscous time units, equivalent to nearly 7.3 largest eddy turn-over time units (i.e., time normalised by h/u_τ). The turbulence statistics calculated from the first half ($3.15h/u_\tau$) of duration are the same as those calculated from the entire simulation period of $7.3h/u_\tau$, indicating that the wind turbulence has reached a fully developed

Case	κ	z_0^+
OS05	0.402	0.115
CR14	0.395	0.500
OS14	0.419	0.104

Table 6: Logarithmic fitting constants for the mean wind profile.

state. Note that the total simulation time for data analysis is comparable to those in previous studies on wind turbulence over waves, which are respecitively 1.6×10^3 (Sullivan *et al.*, 2000), 1.35×10^4 (Yang & Shen, 2010), and 3.4×10^4 (Yang & Shen, 2017) in viscous time unit.

3.2.2 Surface roughness and wave-coherent motion

To quantify the wind–wave momentum flux, we first use logarithmic fit to determine the von Kármán constant and the surface roughness, which are listed in table 6. The data used for fitting are located in the region of $z^+ \geq 30$ and $z/h \leq 0.15$ (Smits *et al.*, 2011). As shown in the table, while the values of the von Kármán constant are close in all three cases, the surface roughness in the case CR14 is about five times that in the open sea cases. The difference in the surface roughness thus provides a straightforward evidence for the impact of wave shoaling on momentum transfer, as the coastal region case CR14 presents an increased drag (i.e. surface roughness), caused by the change in the sea state. As shown in the analyses in subsequent sections, in the cases considered in the present study, the reduced wave age associated with wave shoaling is primarily responsible for the increased momentum flux, while the increased wave steepness may have a secondary effect.

To further investigate the wave effect on wind turbulence, we conduct triple de-

composition of the air field following Hussain & Reynolds (1972):

$$f(x,y,z,t) = \bar{f} + f_w + f' \tag{47}$$

where $\bar{f}$ denotes the time average of f, f_w is the wave-coherent motion, and f' is the 'pure' turbulence motion. Here f_w is extracted from the full turbulence field by:

$$f_w = \frac{1}{L_y T} \int_0^T \mathcal{F}^{-1} \left[\mathcal{F}\left[f\right] e^{-ic_0 tk} \right] \mathrm{d}y\mathrm{d}t - \bar{f}, \tag{48}$$

where c_0 denotes the wave phase speed, $\mathcal{F}$ denotes Fourier transform with respect to the streamwise coordinate x, and T denotes the total time duration for the calculation. The integration here is a conditional average of the raw turbulent data, which removes the 'pure' turbulent fluctuations.

We present the wave-coherent velocity and pressure fields in figure 15. The result for case OS14 is qualitatively similar to that in case OS05 and is thus omitted for the sake of space. Our results show that the strength of the wave-coherent motions increases substantially from the open sea case OS05 to the coastal case CR14. The maximum magnitude of u_w^+, for instance, is several times higher in case CR14. Particularly noteworthy is the phase difference between the wave-coherent motions and the wave surface. For example, in figures 15(b) and 15(d), the contours of the wave-coherent velocity are tilted towards the wave propagation direction, and the phase difference changes from $-\pi/2$ to 0 as the height increases. This is a pattern described as the sheltering effect by Belcher & Hunt (1993), serving as one of the main mechanisms for wave generation. Another important feature is associated with the asymmetry of the wave-coherent pressure field as shown in figure 15(f). This

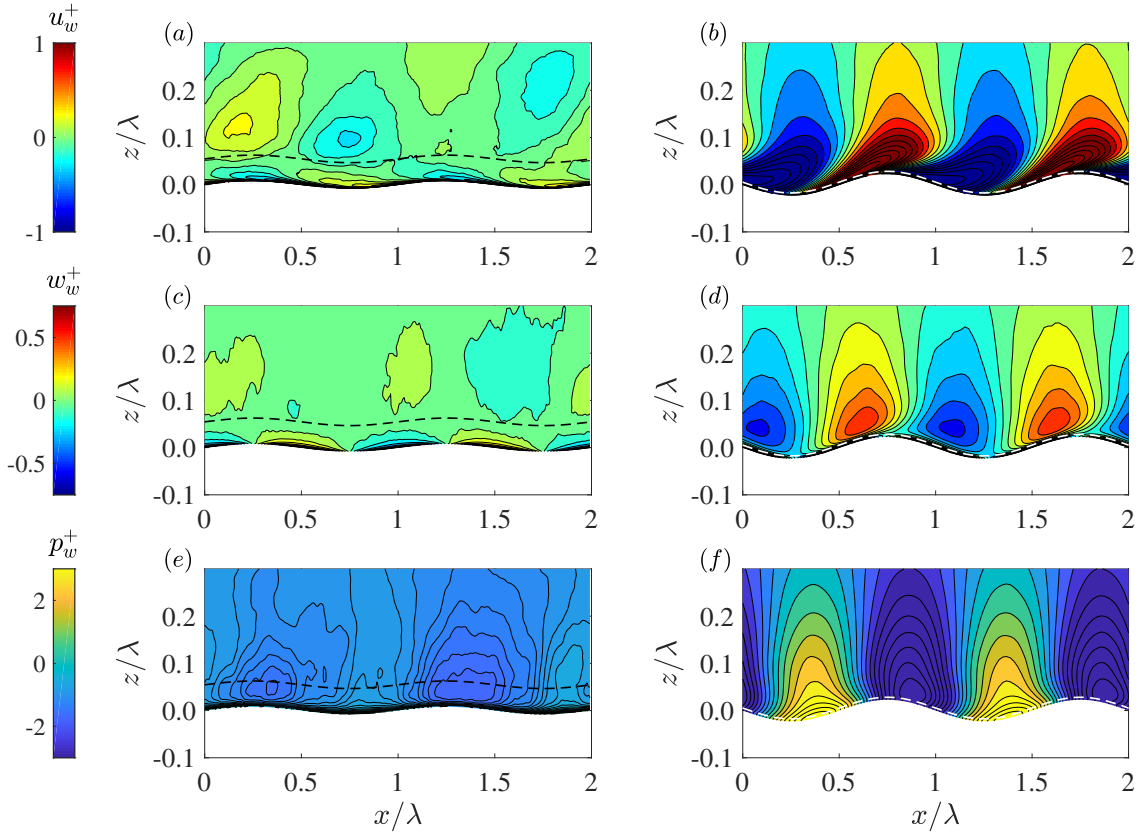

Figure 15: Wave-coherent components of streamwise velocity u_w, vertical velocity w_w, and pressure p_w. All quantities are normalised in wall unit. Here the figures in the left column (a), (c), and (e) correspond to the open sea case OS05, and those in the right column (b), (d), and (f) correspond to the coastal region case CR14. The critical height z_{cr} is denoted by the dashed line. For clarification, only part of the computational domain is shown.

asymmetry is most significant at the wave surface, as the positive pressure is located at the wind-ward side, while the negative pressure lies mostly along the lee-ward side. It is this asymmetry and the increased magnitude of the wave-coherent pressure field that lead to the increased form drag and eventually the enhanced wind–wave momentum transfer in the coastal region, as also shown in the following quantitative analyses. In figure 15, we also plot the critical height z_{cr}, defined as the height where $U(z_{cr}) = c$ (Miles, 1957). In the case OS05, the value of the critical height z_{cr} is 0.055λ. Because the wave speed is reduced in case CR14, the critical height $z_{cr} = 0.0053\lambda$ is much closer to the wave surface. At such a small height, the shear stress may become significant and the quasi-inviscid Miles theory could be inappropriate (see Belcher & Hunt, 1993). The patterns of the wave-coherent motions in figure 15, espeically the asymmetry features, are consistent with those observed in field experiment (Hristov *et al.*, 2003), tank experiment (Buckley & Veron, 2016), and previous simulations (Sullivan *et al.*, 2000; Kihara *et al.*, 2007; Yang & Shen, 2017).

3.2.3 Friction and form drag

The total drag at the wave surface consists of the friction drag and the form drag. In many turbulence studies focusing on engineering applications, to reduce the friction is the main goal (e.g., Choi, Moin & Kim, 1994, Deng & Xu, 2012). In wind–wave interactions, the importance of pressure-induced form drag cannot be overstated (Belcher & Hunt, 1993). In this section, we investigate both the friction drag and form drag at the wave surface, with an emphasis on the latter. We first calculate several integral quantities to investigate the skin-friction generation associated with the self-

sustaining process (de Giovanetti, Hwang & Choi, 2016; Hwang & Bengana, 2016):

$$H_1 = \frac{1}{2L_xL_y}\int_0^{\frac{2}{3}L_y}\int_0^{L_y}\int_0^{L_x} u'^2 \mathrm{d}x\mathrm{d}y\mathrm{d}z \tag{49}$$

$$H_2 = \int_0^{\frac{2}{3}L_y}\left[\left|\hat{u}(\frac{2\pi}{L_y},\frac{2\pi}{L_y},z)\right|^2 + \left|\hat{v}(\frac{2\pi}{L_y},\frac{2\pi}{L_y},z)\right|^2 + \left|\hat{w}(\frac{2\pi}{L_y},\frac{2\pi}{L_y},z)\right|^2\right]\mathrm{d}z \tag{50}$$

$$H_3 = \frac{1}{2L_xL_y}\int_0^{\frac{2}{3}L_y}\int_0^{L_y}\int_0^{L_x} w'^2 \mathrm{d}x\mathrm{d}y\mathrm{d}z \tag{51}$$

$$H_4 = \frac{1}{L_xL_y}\int_0^{L_y}\int_0^{L_x} \tau_\nu \mathrm{d}x\mathrm{d}y \tag{52}$$

where $\widehat{(\cdots)}$ is the velocity component in the Fourier space (k_x, k_y). Here, H_1, H_2, and H_3 denote the energy of streaks, streamwise meandering motions associated with streak instability, and streamwise vortical structures, respectively, while H_4 is the plane-averaged friction drag. The integration in the vertical direction is limited to the region $0 < z < 2L_y/3$ so that the most energetic part of turbulent motions in the self-sustaining process is included (Hwang & Bengana, 2016). While these four integrals were originally used in channel flows with flat walls, there is no explicit requirement on the geometry and motions of the wall and thus they can be readily applied to wind turbulence over waves.

The time evolution of these quantities is presented in figure 16. The curves show similar features as those in channel flows (de Giovanetti *et al.*, 2016). The values of H_i, with $i = 1 - 4$, are not constant over time. Instead, there are quasi-periodic variations, also known as the 'bursting events' (Flores & Jiménez, 2010), which have a time scale of $T_b = 3.1h/u_\tau$. By definition, the integral quantities H_i represent the 'bursting events' associated with the largest energy-containing eddies, the size of which is limited by the computational domain. For smaller eddies within the domain,

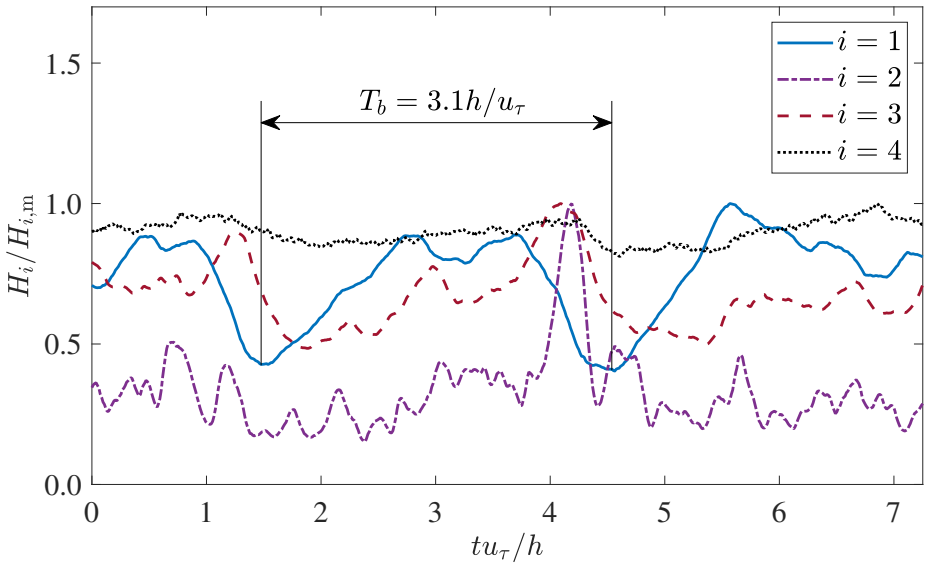

Figure 16: Temporal evolution of the normalised integral quantities $H_i/H_{i,\mathrm{m}}$ ($i = 1, ..., 4$), where $H_{i,\mathrm{m}}$ are the maximum values. Case CR14 is shown here. The marked time interval T_b is the quasi-period of the large scale motions, i.e., the 'bursting events' (Flores & Jiménez, 2010).

the related bursting period is a function of both the domain size and the distance from the wall (Flores & Jiménez, 2010). There are apparent correlations and time lags between the different quantities H_i, because each of them forms part of the full cyclic friction generation and self-sustaining process. In summary, it is found that the friction generation mechanism associated with the self-sustaining process discovered in channel flows also exists in the wind over wave cases.

The form drag originates from the pressure distribution on the wave surface. It can be quantified using the wave-surface-averaged value (e.g., Sullivan *et al.*, 2000):

$$\tau_p = -\frac{1}{L_x L_y}\int_0^{L_y}\int_0^{L_x}\frac{p}{\rho_a}\frac{\mathrm{d}\eta}{\mathrm{d}x}\mathrm{d}x\mathrm{d}y. \tag{53}$$

Note that this definition of form drag is the streamwise component of the form drag

vector, because it neglects the component in the spanwise direction. For a monochromatic wave propagating in the x direction, the above definition is valid as the spanwise component of the form drag vanishes. It also applies to realistic broad-band wave conditions unless the dominant waves propagate at oblique angles with respect to the mean wind field.

According to (47), the surface pressure can be divided into three parts: the mean, the turbulence-related component, and the wave-coherent component. The first two components have negligible contribution to τ_p since their integrals in (53) vanish. Therefore, the form drag is predominantly induced by the wave-coherent pressure (Liu *et al.*, 2010):

$$\tau_p = -\frac{a_p ka}{2\rho_a} \sin \Delta\theta, \tag{54}$$

where a_p is the amplitude of wave-coherent pressure, and $\Delta\theta$ is the phase difference between surface elevation and pressure.

The values of the quantities related to the form drag are listed in table 7. Here, the phase difference and amplitude respectively correspond to the asymmetry and magnitude of the wave-coherent pressure in figures 15(e) and 15(f). The form drag ($\tau_p^+ = -0.041$) in the open sea wave case OS14 is nearly four times that in case OS05 ($\tau_p^+ = -0.011$), because a larger wave steepness leads to a larger pressure amplitude a_p and thus a higher form drag. In the coastal region wave case CR14, the normalised form drag ($\tau_p^+ = -0.31$) is nearly 30 times that in the open sea case OS05 ($\tau_p^+ = -0.011$). This form drag increase is mainly due to the change in the phase difference $\Delta\theta$, the increased pressure magnitude a_p, and the increased wave steepness ka. Here the changes in $\Delta\theta$ and a_p are primarily caused by the difference in the wave age as shown by the comparison among the three cases.

Case	$\Delta\theta$(rad)	a_p^+	τ_p^+	β	c/u_τ	ka
OS05	-0.48	0.877	-0.011	8.11	19.3	0.05
CR14	-0.74	5.95	-0.31	28.5	7.7	0.14
OS14	-0.39	1.41	-0.041	3.81	19.3	0.14

Table 7: Quantities related to form drag. Listed are: $\Delta\theta$, the phase difference between surface elevation and pressure; $a_p^+ = a_p/\rho_a u_\tau^2$, the normalised amplitude of the wave-coherent pressure; $\tau_p^+ = \tau_p/u_\tau^2$, the normalised form drag; β, the wave energy growth rate related to wind input; c/u_τ, the wave age; ka, the wave steepness.

In table 7, we also list the wave growth rate:

$$\beta = \frac{a_p \sin\Delta\theta}{ka\rho_a u_\tau^2}. \tag{55}$$

Note that this equation is obtained by substituting (54) into the definition of the wave growth rate (see Sullivan *et al.*, 2000; Yang & Shen, 2010), a measure of the energy transfer from wind to wave (Miles, 1957). The result shows that β decreases with the increase of wave age (CR14 and OS14) and wave steepness (OS05 and OS14), consistent with the measurement (Peirson & Garcia, 2008; Grare *et al.*, 2013) and simulation results (Sullivan *et al.*, 2000; Liu *et al.*, 2010; Yang & Shen, 2010) in literature.

The mathematical expressions of β and τ_p suggest that the momentum and energy transfer between wind and waves are correlated, where in both processes $\Delta\theta$, a_p, and ka play an essential role. Comparing the results of all three cases, we can conclude that the wave age has a more significant effect on the form drag than the wave steepness. It should be noted that the importance of wave steepness on form drag-related momentum transfer is dependent on the sea states. The wave steepness may

be the dominant factor when waves are at an early stage of growth with small wave ages, such as those in lab measurement conducted in water tank (e.g., Grare *et al.*, 2013). In our wave shoaling cases, the wave age is higher than that in the laboratory experiments and the relative change in wave age is larger than that in wave steepness. As a result, the reduced wave age, rather than the increased wave steepness, is mainly responsible for the form drag increase in the wave shoaling case shown above.

3.2.4 Momentum budget

In this section, we analyse the momentum budget of the wind turbulence following the study by Hara & Sullivan (2015). Consider the balance between the total stress in the streamwise direction and the driving force at the statistically stationary state:

$$\langle \tau_{13} \rangle + \langle \tau_p \rangle + \langle \tau_w \rangle + \langle \tau_v \rangle + \langle \tau_{SGS} \rangle = -(1-\zeta)u_\tau^2, \tag{56}$$

where $\tau_{13} = u'W'$, $\tau_p = (1/J)p_w(\partial\zeta/\partial x)$, $\tau_w = u_w W_w$, $\tau_v = (1/J)\sigma_{1k}(\partial\zeta/\partial x_k)$, and τ_{SGS} are the turbulent stress, wave-induced pressure, wave-induced stress, viscous stress, and SGS stress, respectively, $W = (1/J)u_j(\partial\zeta/\partial x_j)$ is the contravariant component of the vertical velocity, J is the transformation Jacobian matrix (40), and $\sigma_{ij} = -\nu(\partial u_i/\partial x_j + \partial u_j/\partial x_i)$ is the viscous stress in the Cartesian coordinates. The wave-induced pressure at the wave surface is exactly the form drag on the wave, which represents the momentum transfer from wind to wave by pressure. The wave-induced stress originates from the perturbation of the wind flow field by the surface waves. Both the wave-induced pressure and wave-induced stress are directly caused by the presence of water waves, and vary with the wave age and the wave steepness.

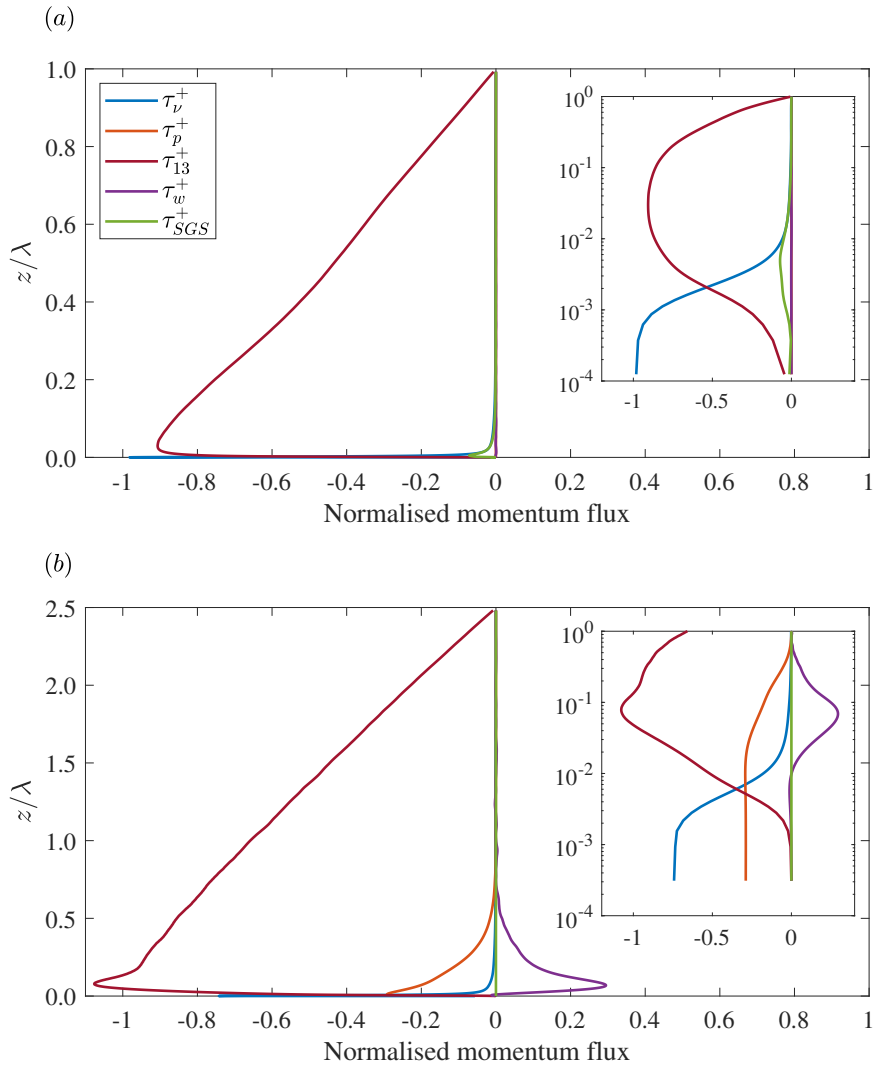

Figure 17: Budget of horizontally averaged momentum flux in (a) open sea case OS05 and (b) coastal region case CR14. The insets are zoom-in views of the profiles in the boundary layer near the wave surface.

The momentum budgets for the open sea case OS05 and the coastal region case CR14 are shown in figures 17(a) and 17(b), respectively. Note that we have omitted the result of case OS14 because it is qualitatively similar to that of case OS05. Of the several stress terms in (56), the viscous stress dominates only in the thin viscous sublayer adjacent to the wave surface, while the turbulent stress becomes the main contributor in the outer regions. There is an appreciable difference in the wave-induced pressure and stress between the open sea case and the coastal region case. In the open sea case OS05, the stresses caused by wave effect are negligibly small in the entire domain. In the coastal region case CR14, the wave effect is prominent and the peak values of these two stresses reach approximately 30% of the total stress. As expected, the wave-induced pressure in this case is negative, because it can be viewed as the form drag on the wave-following ζ plane. Near the wave surface, there is an excess of turbulent stress as also observed by Hara & Sullivan (2015): $|\langle\tau_{13}\rangle| > (1-\zeta)u_*^2$, caused by the large positive wave-induced stress $\langle\tau_w\rangle$ that exceeds the magnitude of the wave-induced pressure (see the inset of figure 17b). This difference between the open sea case and the coastal region case can be attributed to the reduced wave age as well as the increased wave steepness for the coastal region wave. Since the momentum budget results in cases OS05 and OS14 (not plotted) are nearly identical, we infer that the wave age plays a more important role than the wave steepness in terms of their impacts on the wave-related stress terms.

3.3 Wind over broad-band waves

3.3.1 Broad-band wave shoaling

In this section, we investigate the shoaling of realistic broad-band waves and obtain the directional wave spectrum in coastal region from a numerical experiment based on a nonlinear mild slope equation (Agnon & Sheremet, 1997; Davis *et al.*, 2014; Sheremet *et al.*, 2016), in which key physical processes involved in wave shoaling are captured. In this model, the wave surface elevation $\eta(x, y, t)$ is expressed in Fourier modes in terms of frequency ω and alongshore wavenumber k_y:

$$\eta(x, y, t) = \sum_{\omega, k_y} a(\omega, k_y, x) \exp i \left[\phi(x) + k_y y - \omega t\right], \tag{57}$$

where $\phi(x)$ is the phase function.

Define $B(\omega, k_y, x) = aC^{1/2}e^{i\phi}$, where C is the across-shore component of the group velocity, and the evolution equation yields (Davis *et al.*, 2014):

$$\frac{\partial B(\omega, k_y, x)}{\partial x} = ik_x B - \Gamma_d B + \sum_{P,Q} \left(-\delta_{Q+P} + 2\delta_{Q-P}\right) iW_{\pm P,Q} B_{\pm P} B_Q, \tag{58}$$

where Γ_d is a coefficient representing the wave energy dissipation caused by various processes, such as bottom friction and wave breaking. Because these dissipation processes are not resolved, the value of Γ_d is determined empirically (Agnon & Sheremet, 1997). The third term on the right hand side of (58) denotes the energy transfer

U_{10} (m/s)	α_p	f_p (Hz)	λ_p (m)
12	0.012	0.16	54

Table 8: Parameters of the initial JONSWAP wave field in open sea, where α_p is the Phillips parameter, f_p is the peak wave frequency, and λ_p is the peak wavelength.

$-\Delta d/\Delta x$	μ_c	$N_f \times N_k$	Δf (Hz)	Δk_y (1/m)
1%	1.0	120×80	0.004	0.003

Table 9: Parameters in the wave shoaling model, where $-\Delta d/\Delta x$ is the bottom slope, μ_c is the threshold to determine the resonant triads, N_f and N_k are grid numbers, and Δf and Δk_y are respectively the frequency and wavenumber interval.

among wave components in all triad groups that satisfy the following conditions:

$$\omega = \omega_Q \pm \omega_P, \tag{59}$$

$$k_y = k_{y,Q} \pm k_{y,P}, \tag{60}$$

$$|k_x \mp k_{x,P} - k_{x,Q}| \leq \mu_c k, \tag{61}$$

where μ_c is a threshold that determines the percentage of near-resonant interactions involved in the computation. For an active triad, the interaction coefficient is:

$$\begin{aligned} W_{\pm P,Q} =& \frac{1}{2}\frac{g\omega}{\omega_P \omega_Q}\left(CC_P C_Q\right)^{-1/2} \\ & \times \left(\pm 2\boldsymbol{k_P}\cdot\boldsymbol{k_Q} + k_P^2\frac{\omega_Q}{\omega} \pm k_Q^2\frac{\omega_Q}{\omega} + \frac{\omega_P^2\omega_Q^2}{g^2} \mp \frac{\omega^2\omega_P\omega_Q}{g^2}\right). \end{aligned} \tag{62}$$

The wave shoaling process is simulated by integrating equation (58) from a deep water depth towards the shore. Without loss of generality, the initial open sea wave field $B(\omega, k_y, x)$ is constructed from a directional JONSWAP spectrum $E(f, \theta)$ as

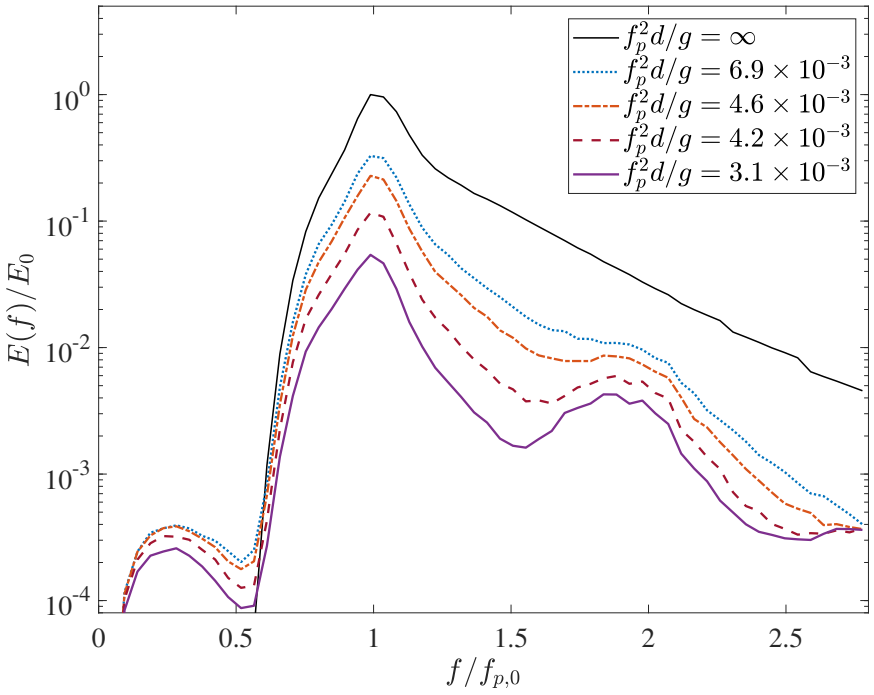

Figure 18: Omnidirectional frequency spectrum at different water depths. Here $f_{p,0}$ is the initial peak frequency and $E_0 = E(f_{p,0})$ is the peak wave energy density of the initial JONSWAP spectrum (black solid line, see also table 8).

used in Davis *et al.* (2014). The parameters of the JONSWAP spectrum are listed in table 8. Each wave component is assigned a random phase with a uniform distribution between 0 and 2π, and thus the Gaussian hypothesis is invoked here (Komen *et al.*, 1994). The numerical parameters are listed in table 9. The slope of the bottom bathymetry is comparable to the simulations in Davis *et al.* (2014) and Sheremet *et al.* (2016). The grid numbers and intervals are chosen in accordance with the requirement to resolve the wave components with the most energy, i.e., those near the peak of the wave spectrum. To obtained converged statistics, we conduct 64 simulations with independent initial realisations of the random wave phases, and the results presented below are the ensemble average of all these cases.

The changes in the wave spectrum are presented in figures 18 and 19. In the omnidirectional spectra shown in figure 18, we observe a distinct second harmonic peak near $f/f_{p,0} = 2$. It corresponds to a special type of triad interactions when P and Q refer to the same wave component in (59). A relatively weak peak appears at very low frequency, suggesting the generation of infragravity wave because of triad interactions. The presence of these two peaks is related to the wave shoaling process, because it leads to the change in the dispersion relation at various water depths and thus the numbers of wave components involved in triad interactions. Figure 18 also shows a decreasing wave energy as the water depth decreases, owing to the depth-limited breaking effect modelled in (58). The process of wave refraction can be found in the directional spectrum (figure 19), where the spreading of wave energy becomes narrower in coastal region. In summary, the shape of the wave spectrum in coastal region is predominantly a result of the wave energy redistribution, dissipation, and the change in wave propagation direction.

3.3.2 LES of wind over broad-band waves

In this section, we design a numerical experiment for wind over a broad-band wave field where the wind turbulence is computed using LES (Yang *et al.*, 2014*a*,*b*) and waves are simulated using a high-order-spectral (HOS) method (Dommermuth & Yue, 1987; Yang & Shen, 2011*b*). The governing equations for wind turbulence is the same as (41) except that the viscous terms are neglected because the Reynolds number is very large at the field scale. A wall model is applied at the wind–wave interface to provide an estimation of the stress at the water surface (Yang *et al.*, 2013). The computational parameters are listed in table 10. Two simulation cases

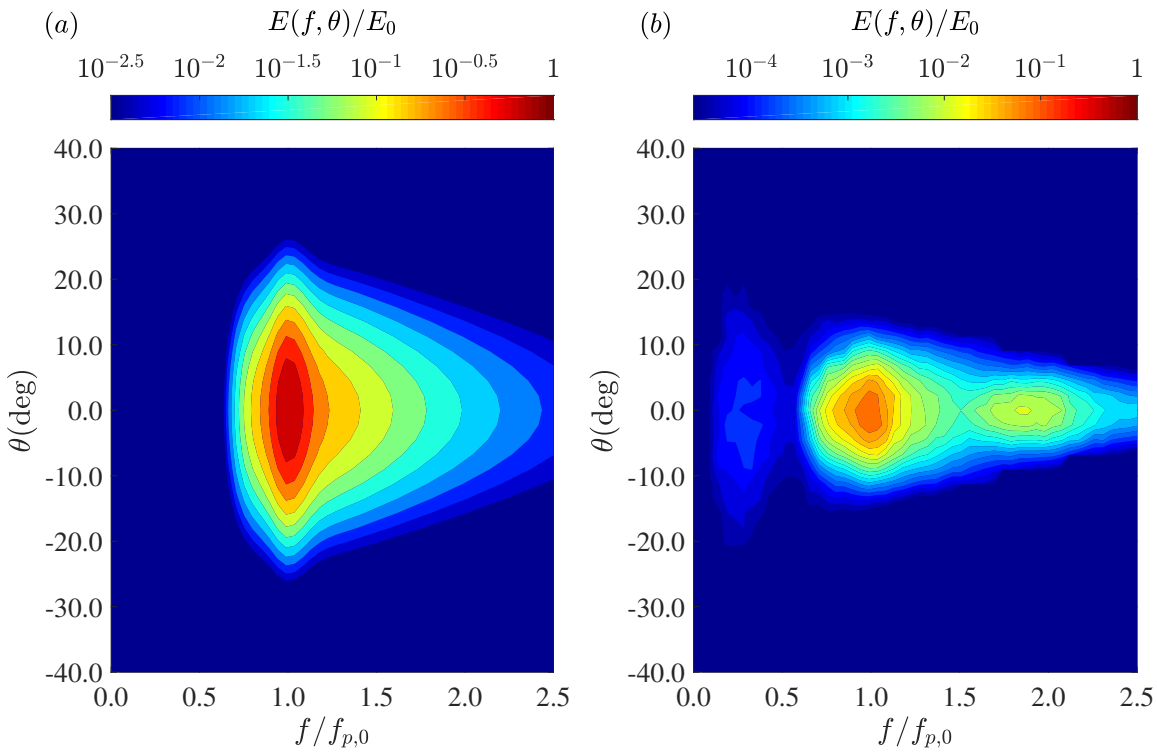

Figure 19: Directional wave spectrum in (a) open sea (black solid line in figure 18) and (b) coastal region (purple solid line in figure 18). See the caption of figure 18 for the definition of E_0.

are considered. In the first case WMOS, the initial wave field is constructed from the JONSWAP wave spectrum (table 8), and the wind–wave system is representative in the open sea. In the second case WMCR that simulates the coastal wind–wave field, the initial condition of the HOS model is constructed using the coastal wave spectrum shown in figure 19(b), which is obtained from the wave shoaling simulation described in § 3.3.1. Note that for this case, we replace the open sea HOS model with the one used in coastal region (Liu & Yue, 1998). The key parameter of the wall model in LES, namely the surface roughness, is calculated using a dynamic model (Yang *et al.*, 2013). In this model, the sea-surface roughness is written as:

$$z_{0,\Delta} = \sqrt{z_{0,s}^2 + (\alpha_w \sigma_\eta^\Delta)^2}, \tag{63}$$

where $z_{0,s}$ is associated with the viscous effect at a flat plane, and $\alpha_w \sigma_\eta^\Delta$ is associated with the air–water momentum flux caused by the waves. Here, Δ is the LES filter scale, α_w is a coefficient to be determined dynamically, and σ_η^Δ is the effective wave amplitude calculated from the wave-kinematic-dependent model developed by Yang *et al.* (2013) based on Kitaigorodskii & Volkov (1965) and Kitaigorodskii (1968):

$$\sigma_\eta^\Delta = \left[\int_{-\pi/2}^{\pi/2} \int_{\pi/\Delta}^{2\pi/\lambda_c} E(k,\theta) \exp\left(-\frac{2\kappa}{u_\tau} \sqrt{\frac{\mathrm{g}}{k}} \right) \mathrm{d}k \mathrm{d}\theta \right]^{1/2}. \tag{64}$$

The key assumption of the dynamic surface roughness model is that the total drag at the wind–wave interface should be the same when calculated from the velocity fields

u_τ(m/s)	$(L_x,\ L_y,\ L_z)$ (m)	$N_x \times N_y \times N_z$	$(\Delta x,\ \Delta y,\ \Delta z)$ (m)
0.444	540, 540, 270	$256 \times 256 \times 384$	3.2, 3.2, 0.70

Table 10: Simulation parameters of the wind field for the wall-modelled LES cases. Note that Δx and Δy are the effective grid size after 2/3 dealiasing in horizontal directions.

of two different resolutions in LES (Yang *et al.*, 2013):

$$\iint \widetilde{p}^s \widetilde{n}_1 \mathrm{d}x\mathrm{d}y + \rho_a \iint \left[\frac{\kappa \widehat{\widetilde{U}}_r}{\log\left(d_2 / \sqrt{z_{0,s}^2 + (\alpha_w \sigma_\eta^\Delta)^2} \right)} \right] \frac{\widehat{\widetilde{u}}_{r,1}}{\widehat{\widetilde{U}}_r} \mathrm{d}x\mathrm{d}y \tag{65}$$

$$= \iint \widehat{\widetilde{p}}^s \widehat{\widetilde{n}}_1 \mathrm{d}x\mathrm{d}y + \rho_a \iint \left[\frac{\kappa \overline{\widehat{\widetilde{U}}}_r}{\log\left(d_2 / \sqrt{z_{0,s}^2 + (\alpha_w \sigma_\eta^{\widehat{\widetilde{\Delta}}})^2} \right)} \right] \frac{\overline{\widehat{\widetilde{u}}}_{r,1}}{\overline{\widehat{\widetilde{U}}}_r} \mathrm{d}x\mathrm{d}y, \tag{66}$$

where $\widehat{(\widetilde{\ldots})}$ and $\overline{\widehat{(\widetilde{\ldots})}}$ denote the filtering at scale $\widehat{\widetilde{\Delta}}$ and $\overline{\widehat{\widetilde{\Delta}}}$, respectively, $u_{r,1}$ is the x-direction wind velocity relative to wave surface at the first grid above the surface, d_2 is the mean vertical height of the first grid point above the surface, n_1 is the x-component of the normal vector of the wave surface, and $U_r = \sqrt{u_{r,1}^2 + u_{r,2}^2}$ is the magnitude of the horizontal wind velocity relative to the water surface. The left hand side is therefore the total surface stress calculated from a flow field $(\tilde{u}, \tilde{p})$ at scale Δ, while the right hand side from a flow field $(\widehat{\widetilde{u}}, \widehat{\widetilde{p}})$ at scale $\tilde{\Delta}$. For the applications of the dynamic roughness model in the coastal region case, the wave properties, such as open sea wave speed $\sqrt{g/k}$ in (64), are adjusted according to the general dispersion relation $\omega^2 = gk \tanh(kd)$. Note that these adjustments do not change the underlying assumptions of the numerical scheme and the dynamic surface roughness model.

It is found that the momentum flux between wind and waves increases markedly

	$\alpha_{ch} = gz_0/u_\tau^2$	$R_{CD} = C_D^{\mathrm{WMCR}}/C_D^{\mathrm{WMOS}}$
Case WMCR	0.16	1.8
Case WMOS	0.019	n/a
Oost *et al.* (2001)	–	1.0-1.6
Shabani *et al.* (2014)	0.110	$\sim$2
Ortiz-Suslow *et al.* (2015)	–	2.6

Table 11: Normalised surface roughness and drag coefficient ratio.

in the coastal region case. We list the surface roughness from our simulations, as well as the recent field observations in table 11. The normalised roughness in case WMCR is calculated using the dynamic model mentioned above, and is comparable to the measurement by Shabani *et al.* (2014). Its value is nearly eight times the roughness estimated in the open sea case WMOS. The coefficient $R_{CD} = C_D^{\mathrm{WMCR}}/C_D^{\mathrm{WMOS}}$ is defined as the ratio of the coastal drag coefficient to the open sea value. In Ortiz-Suslow *et al.* (2015), the open sea drag coefficient used to estimate R_{CD} is calculated using the Smith (1988) algorithm. In Shabani *et al.* (2014), α_{ch} is the mean value of their experimental data. In Oost *et al.* (2001), the drag coefficients from measurement and the Smith (1980) parameterisations are plotted as a function of the wind speed, and the values of R_{CD} listed in table 11 correspond to the range of wind speed from 7 m/s to 15 m/s. The increase of momentum flux may also be observed directly from the mean profile of the wind field (figure 20), where the coastal mean wind speed is significantly reduced compared with the open sea. As a conclusion, wave shoaling leads to substantial increase in the momentum flux in the coastal region and reduction in wind speed.

In figure 21, we plot the vertical profiles of the correlation coefficient between the wind field and wave field. The correlation coefficient of two variables, f_1 and

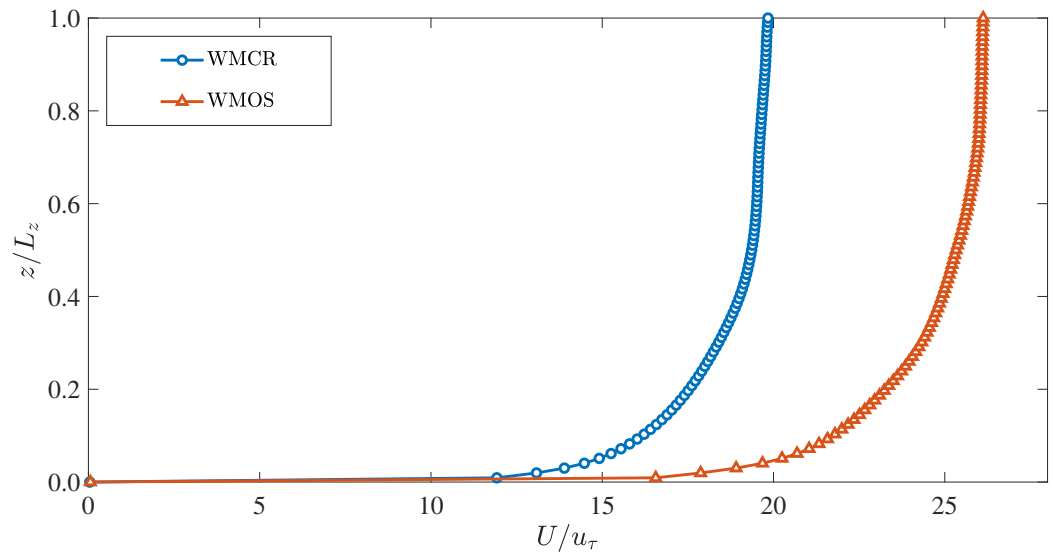

Figure 20: Mean velocity profiles of the wind field for the open sea case WMOS and the coastal case WMCR. The mean velocity is normalised by the friction velocity and the height is normalised by the vertical domain length.

f_2, is defined as $\mathrm{Corr}(f_1, f_2) = \langle f_1 f_2 \rangle / \sigma_{f_1} \sigma_{f_2}$, where σ is the standard deviation. It should be noted that the vertical height is normalised by the peak wavelength, because the wave penetration depth into the wind turbulence is dependent on the wavelength (Chalikov & Belevich, 1993; Makin, Kudryavtsev & Mastenbroek, 1995). As shown, the magnitudes of the correlation coefficients are apparently larger in the coastal case WMCR, which is expected because the wind–wave equilibrium state is not reached at the small wave age. In both cases, $\mathrm{Corr}(u, \eta)$ and $\mathrm{Corr}(w, \eta)$ are positive while $\mathrm{Corr}(p, \eta)$ is negative. Contrarily, under the swell-dominated condition, the correlation coefficients $\mathrm{Corr}(u, \eta)$ and $\mathrm{Corr}(w, \eta)$ switch signs (Sullivan *et al.*, 2014), which is due to the fact that the wave-coherent velocity field has a different phase with respect to the wave surface elevation.

To further illustrate the wave shoaling effect on wind turbulence, we examine the

full wavenumber–frequency spectrum $F_{11}(\mathbf{k}, \omega; z)$ of the streamwise velocity of the wind turbulence at the height z. For demonstration, the spectrum $F_{11}(\mathbf{k}, \omega; z)$ is projected onto the (k_1, ω) plane. The result is plotted in figure 22. The Doppler shift caused by the advection of the mean velocity and the Doppler broadening due to large eddies can be observed on the spectrum, which is similar to turbulent flows over a flat plate (Wilczek & Narita, 2012). In the first part of this study on monochromatic shoaling waves (§ 3.2), we can extract wave-induced motions by taking the phase-average of the wind velocity and pressure field because they appear as a fixed point in the wavenumber–frequency space. For the more general broad-band waves shown here, there is no absolute criterion to distinguish the 'pure' turbulent motions and those induced by waves, because their length and time scales are mingled together (Hristov, Friehe & Miller, 1998). In figure 22, the wave shoaling effect can be identified from its signature on the full spectrum. Because of wave shoaling, the wavelengths are reduced in the coastal region, and thus the wave-induced energy moves to higher wavenumbers on the spectrum of case WMCR. In the coastal region, the dispersion relation is a straight line in figure 22(a) as these waves are nondispersive and share the same wave speed, while in the open sea, as shown by figure 22(b), the dispersion relation is a parabolic curve (Dean & Dalrymple, 1991). Our result shows that the waves leave a distinct feature on the wind velocity spectrum, where the wave-induced energy distribution aligns along the wave dispersion relation curve, which is affected by the water depth. In other words, there exists a footprint of wave shoaling in the wind spectrum.

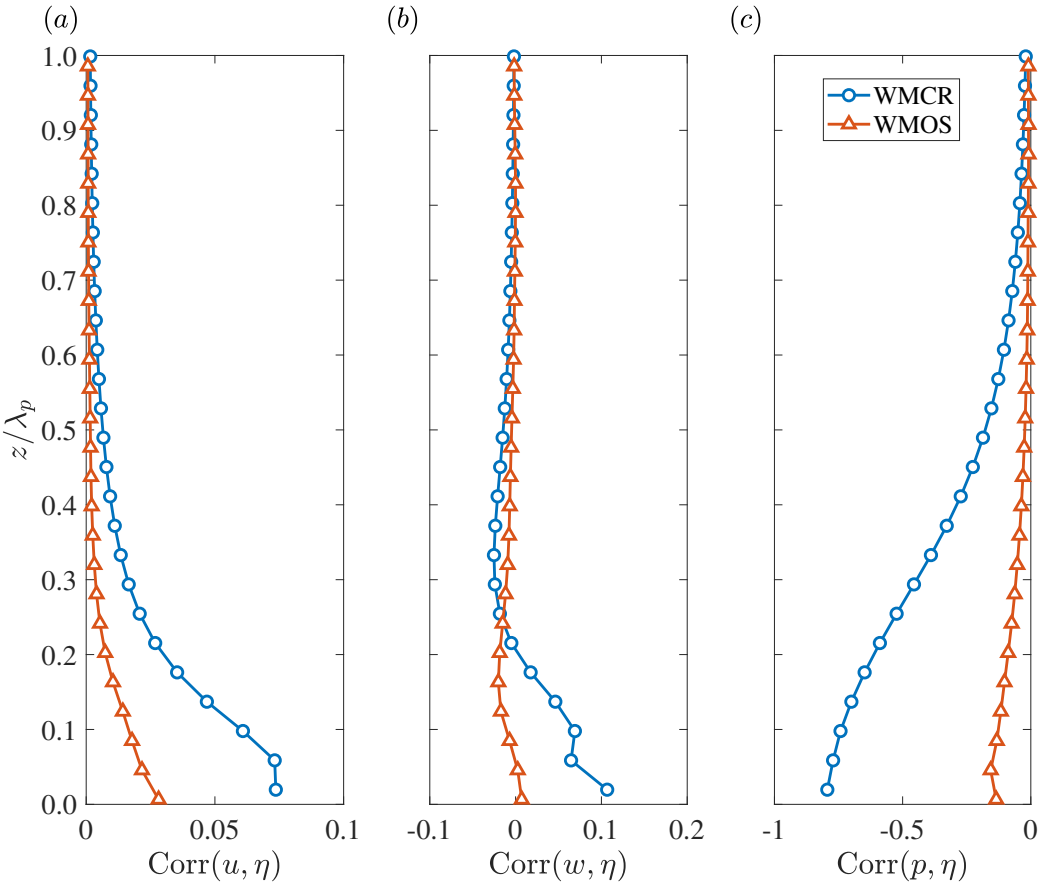

Figure 21: Vertical profiles of the correlation coefficient between wind and waves. The vertical height is normalised by the peak wavelength in each case.

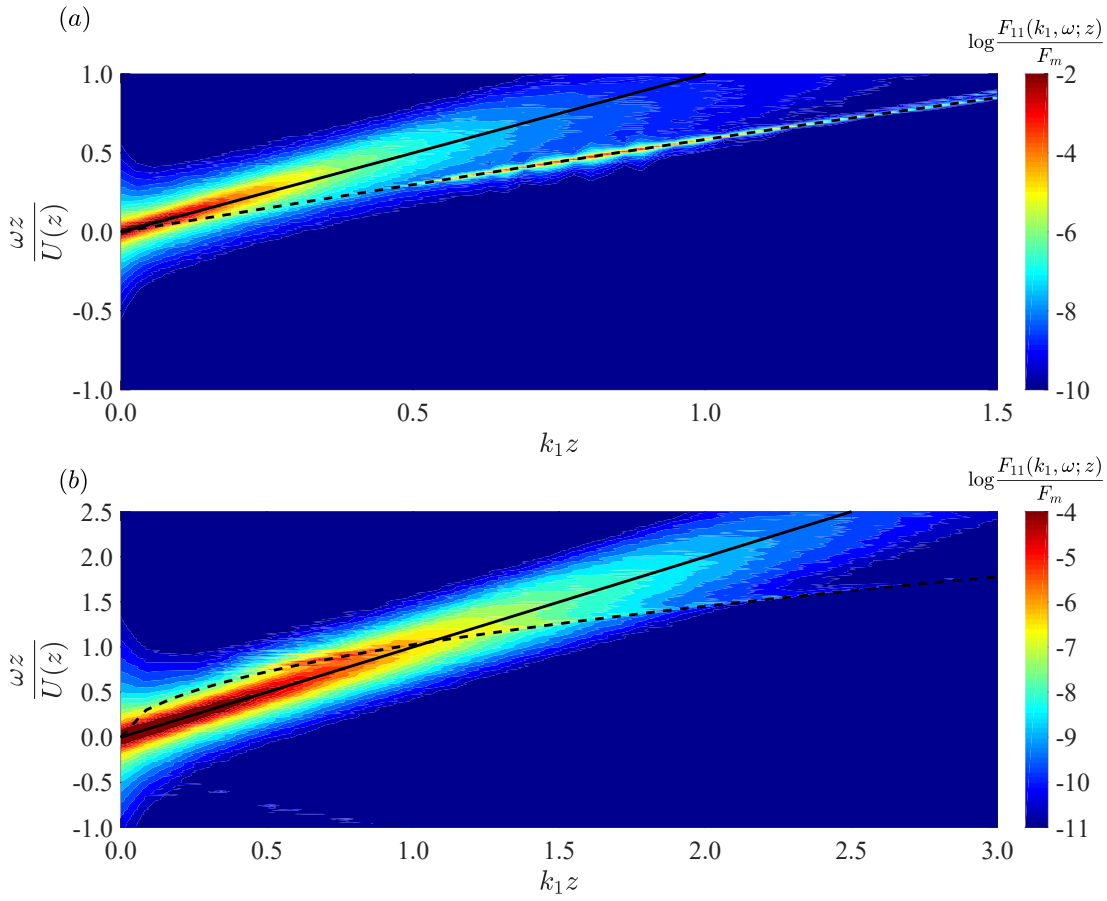

Figure 22: Wavenumber–frequency spectrum of the streamwise wind velocity: (a) coastal case WMCR and (b) open sea case WMOS. The velocity data are located on a horizontal plane at a height $z/\lambda_p = 0.13$. The solid line denotes the Doppler shift by the mean wind velocity: $\omega = k_1 U(z)$. The dashed line denotes the wave dispersion relation: (a) $\omega = k_1\sqrt{gd}$ and (b) $\omega = \sqrt{gk_1}$.

3.4 Conclusions

In this study, we have investigated the wave shoaling effect on wind–wave momentum flux using numerical simulations. In the first part, we have examined the momentum flux change caused by the shoaling of monochromatic waves. The changes in wave age and wave steepness induced by wave shoaling are first obtained by utilizing the analytical shoaling coefficient. We then conduct wall-resolved LES of wind turbulence over waves in the open sea and coastal region, respectively. The change in the wind–wave momentum flux induced by the wave shoaling is found to be prominent. The surface roughness in the coastal region case CR14 is nearly five times that in the open sea (cases OS05 and OS14). We have shown that this enhancement in wind–wave momentum flux in coastal region is accompanied by significantly stronger wave-coherent motions in the wind velocity and pressure field. Besides the magnitude, the spatial patterns of the wave-coherent motions in case CR14 are qualitatively different from those in the open sea. We have analysed the friction generation using several integral quantities. From the time evolution of these integral quantities, we observe large quasi-periodic motion and apparent correlations among these quantities. Our results show that for wind turbulence over waves, the friction generation is closely related to the turbulence self-sustaining process. We have also quantified the form drag, which takes up a much larger portion of the total drag in the coastal region case than in the open sea case. The cause for this large difference is found to originate from the asymmetry and magnitude increase of the wave-coherent pressure in the air. We have further analysed the momentum budget by isolating the stress terms from different effects in the total momentum balancing equation. While the stresses related to wave effect are small in the open sea cases, they are prominent from the surface up

to a vertical height of 0.5λ in the coastal region case. Because we have designed our numerical experiments with the wave age and steepness being the control variables, we can identify their relative importance in determining the momentum flux, and our results suggest that the wave age change in shoaling has a larger impact.

In the second part of this study, we first capture the wave shoaling process using a mild slope equation. Starting from a broad-band directional wave spectrum in the open sea, we integrate the equation and obtain the coastal region wave spectrum, which shows the features of low-frequency infragravity waves, second order harmonics, a decreased wave energy, and a reduced directional spreading. Based on this spectrum, we perform LES–HOS simulation for the wind–wave field in the coastal region and quantify the surface roughness using a dynamical model. For comparison, we also set up a simulation case for wind over broad-band waves in the open sea. We find that the coastal surface roughness is nearly eight times the value from the open sea parameterisation, corresponding to a drag coefficient ratio of approximately 1.8. This increased momentum flux is a result of the wave effect, as indicated by the correlation function between the wind turbulence field and wave surface elevation. The wave effect is also identified on the full wavenumber–frequency spectrum of the wind field. The fusion of the wave-induced motions and turbulent motions on the spectrum reveals a scenario at sea when these two types of motions have a mingled range of space and time scales. While this feature causes difficulty to quantify the wave contribution to the wind–wave momentum flux, we have identified the wave shoaling effect from the spectrum. In particular, we find that the wave-induced motions align with the dispersion relation of waves. Because of wave shoaling, the wave dispersion appears as a straight line in the wavenumber–frequency spectrum in coastal region,

compared with the parabolic curve in open sea, and the wave-induced motions move towards higher wavenumbers in the spectrum. In summary, the shoaling of broad-band waves has a distinct signature on the turbulent wind and contributes to the increased momentum flux in the coastal region.

Finally, we remark that there are several problems not addressed in this study but require special attention in future studies. First of all, we have focused on neutral conditions and excluded the stratification effect, which could be important in the atmospheric boundary layer in the large scale air–sea–land interactions (Hsu, 1988; Garratt, 1990; Yang *et al.*, 2018*a*). Furthermore, there are two important physical processes that can affect the coastal wave dynamics and thus the wave-dependent surface roughness. One is wave–current interaction as the currents can lead to changes in the wave properties (Peregrine, 1976; Dysthe, 2001; Ardhuin *et al.*, 2012; Romero *et al.*, 2017). The other is wave breaking, which can drastically change the wind turbulence structure and the wind–wave momentum flux. With the increase in computer power in the coming years, these processes should be simulated and investigated in future research.

4 Surface Wave Signature Induced by Internal Wave

4.1 Introduction

Internal waves are a common type of fluid motions in the ocean interior. They affect not only the nearshore ecosystem (Woodson, 2018) but also the energy transfer in global circulation (Ferrari & Wunsch, 2009). As internal waves propagate, they leave on the ocean surface a distinct signature of alternating rough and smooth regions. When observed using satellite radars, this signature of internal waves appears in the form of bright and dark bands, similar to the white and black stripes of a zebra. Such bands appear when a spatial change in the wave roughness induces a variation in the strength of the backscattering of the electromagnetic signals of radars (Perry & Schimke, 1965; Ziegenbein, 1969; Osborne & Burch, 1980). The surface signature obtained via remote sensing is a critical technique for the identification of internal waves (Helfrich & Melville, 2006), which allows a large area coverage compared with in-situ measurements. It remains a challenge to quantify the surface signature for the purpose of internal wave characterization. For mechanistic study, it would be desirable to resolve a wide range of wave motions from the first principles of fluid dynamics so that the impact of internal waves on the surface waves can be accurately described and modeled.

In previous studies, attempts to quantify the surface wave variation are often based on the ray theory in a manner similar to geometrical optics. In this theory, an individual surface wave component is tracked by the change in its wavenumbers and energy, whereas the wave phase is discarded. The effect of the internal wave is generally treated as a prescribed time-invariant surface current (Alpers, 1985; Donato

et al., 1999; Bakhanov & Ostrovsky, 2002). Under this assumption, a singularity occurs when the surface waves are blocked by the countercurrent induced by the internal wave (Peregrine, 1976). The singularity can be illustrated by the dispersion relation of one-dimensional surface waves on a current: $\omega = kU + \sqrt{gk}$, where ω denotes the wave (angular) frequency, k the wavenumber, and U the current velocity. The dispersion relation is therefore a quadratic equation for $\sqrt{k}$. If the wave and current are counterpropagating, i.e., $kU < 0$, and if the current is sufficiently strong, it is possible that the equation has no real solutions where the wave is blocked by the current (Smith, 1975; Peregrine, 1976). For certain idealized wave conditions, the wave amplitude can be approximated by an Airy function in the vicinity of the blocking point (Smith, 1975; Peregrine, 1976; Nardin *et al.*, 2009). Given the generally complex wave field at sea, it is unlikely that the same ray theory approach can be extended to the study of the formation of surface signature.

Furthermore, it remains unclear whether external physical processes play a determinant role in the surface signature formation. Surface waves can acquire energy from wind and dissipate energy via turbulent motions when they break. These processes may also affect the water surface roughness (Bakhanov & Ostrovsky, 2002; Jackson *et al.*, 2013). The smooth region was conjectured in some research to be a result of wave energy dissipation induced by blocking-induced wave breaking (Phillips, 1966), while on the other hand, Peregrine pointed out that wave blocking not necessarily causes breaking (Peregrine, 1976). Since it is impossible to remove the effects of wind and wave breaking in field measurement at sea, two recent studies rely on numerical simulation (Craig *et al.*, 2012) and laboratory measurement (Kodaira *et al.*, 2016) to isolate the impact of internal waves. While not directly showing the zebra pattern,

both studies suggest that an internal wave can induce the surface signature in the absence of wind input and wave breaking.

Here we show that the surface signature can be formed within an energy conservative framework, from which the singularity and effect of external processes are excluded. Our study is based on the simulation of two layers of fluids with different densities, which are incompressible, irrotational, and immiscible at the interface (Lamb, 1932; Apel, 1988; Sutherland, 2010). Starting from the primitive wave-phase-resolved governing equations allows us to avoid the singularity issue encountered in the phase-averaging ray theory. This approach is justified by a number of studies in the astrophysics community (Schützhold & Unruh, 2002; Michel & Parentani, 2014; Euvé *et al.*, 2015), which use the blocking events in wave-current interaction as an analogue to the black hole physics. Under the potential flow assumption, the simulation framework conserves energy (Alam *et al.*, 2009*a*; Tanaka & Wakayama, 2015), and thus the interaction between surface waves and internal waves is isolated from possible effects from external energy sources.

4.2 Mathematical model

Our simulation is performed using the two-layer ocean model (Lamb, 1932; Sutherland, 2010), where the upper layer fluid has a smaller density than the lower layer fluid, while in each layer the fluid has a constant density. The governing equations are as follows:

$$\nabla^2 \phi_u(x, y, z, t) = 0, \tag{67}$$

$$\nabla^2 \phi_l(x, y, z, t) = 0. \tag{68}$$

The kinematics and dynamics boundary conditions at the surface $z = \eta_u$ are:

$$\frac{\partial \eta_u}{\partial t} + \nabla_{\boldsymbol{x}} \eta_u \cdot \nabla_{\boldsymbol{x}} \phi_u - \phi_{u,z} = 0, \tag{69}$$

$$\frac{\partial \phi_u}{\partial t} + g\eta_u + \frac{1}{2}\nabla\phi_u \cdot \nabla\phi_u - \frac{\sigma_s}{\rho_u}\nabla_{\boldsymbol{x}} \cdot \left[\frac{\nabla_{\boldsymbol{x}}\eta_u}{\sqrt{1 + |\nabla_{\boldsymbol{x}}\eta_u|^2}}\right] = 0. \tag{70}$$

At the interface $z = -h_u + \eta_l$, the boundary conditions yield:

$$\frac{\partial \eta_l}{\partial t} + \nabla_{\boldsymbol{x}} \eta_l \cdot \nabla_{\boldsymbol{x}} \phi_u - \phi_{u,z} = 0, \tag{71}$$

$$\frac{\partial \eta_l}{\partial t} + \nabla_{\boldsymbol{x}} \eta_l \cdot \nabla_{\boldsymbol{x}} \phi_l - \phi_{l,z} = 0, \tag{72}$$

$$\frac{\partial \phi_u}{\partial t} + g\eta_l + \frac{1}{2}\nabla\phi_u \cdot \nabla\phi_u + \frac{p_u}{\rho_u} = 0, \tag{73}$$

$$\frac{\partial \phi_l}{\partial t} + g\eta_l + \frac{1}{2}\nabla\phi_l \cdot \nabla\phi_l + \frac{p_l}{\rho_l} = 0, \tag{74}$$

$$p_l - p_u = -\sigma_i \nabla_{\boldsymbol{x}} \cdot \left[\frac{\nabla_{\boldsymbol{x}}\eta_l}{\sqrt{1 + |\nabla_{\boldsymbol{x}}\eta_l|^2}}\right], \tag{75}$$

where ϕ_u (respectively, ϕ_l), ρ_u (respectively, ρ_l), and h_u (respectively, h_l) are the velocity potential, density, and mean depth of the upper (respectively, lower) layer fluid, σ_s (respectively, σ_i) is the surface tension of the air-upper fluid surface (respectively, upper-lower fluid interface), p_u (respectively, p_l) is the interface pressure on the upper (respectively, lower) fluid side, and $\nabla_{\boldsymbol{x}} = (\partial/\partial x, \partial/\partial y)$ denotes the gradient operator in horizontal directions.

At the bottom $z = -h_u - h_l$, the boundary condition is:

$$\phi_{l,z} = 0. \tag{76}$$

The boundary conditions can be written as the evolution equations of four surface/interface quantities, which uniquely determine the dynamics of the system (Alam *et al.*, 2009*b*):

$$\frac{\partial \eta_u}{\partial t} = -\nabla_{\boldsymbol{x}}\eta_u \cdot \nabla_{\boldsymbol{x}}\phi_u^s + \left(1 + \nabla_{\boldsymbol{x}}\eta_u \cdot \nabla_{\boldsymbol{x}}\eta_u\right)\phi_{u,z}, \tag{77}$$

$$\begin{aligned}\frac{\partial \phi_u^s}{\partial t} = & -g\eta_u - \frac{1}{2}\nabla_{\boldsymbol{x}}\phi_u^s \cdot \nabla_{\boldsymbol{x}}\phi_u^s + \frac{1}{2}\left(1 + \nabla_{\boldsymbol{x}}\eta_u \cdot \nabla_{\boldsymbol{x}}\eta_u\right)\phi_{u,z}^2 \\ & + \frac{\sigma_s}{\rho_u}\nabla_{\boldsymbol{x}} \cdot \left[\frac{\nabla_{\boldsymbol{x}}\eta_u}{\sqrt{1 + |\nabla_{\boldsymbol{x}}\eta_u|^2}}\right],\end{aligned} \tag{78}$$

$$\frac{\partial \eta_l}{\partial t} = -\nabla_{\boldsymbol{x}}\eta_l \cdot \nabla_{\boldsymbol{x}}\phi_u^i + \left(1 + \nabla_{\boldsymbol{x}}\eta_l \cdot \nabla_{\boldsymbol{x}}\eta_l\right)\phi_{u,z}, \tag{79}$$

$$\begin{aligned}\frac{\partial \psi^i}{\partial t} = & \frac{1}{2}\left(R\nabla_{\boldsymbol{x}}\phi_u^i \cdot \nabla_{\boldsymbol{x}}\phi_u^i - \nabla_{\boldsymbol{x}}\phi_l^i \cdot \nabla_{\boldsymbol{x}}\phi_l^i\right) - g\eta_l\left(1 - R\right) \\ & + \frac{1}{2}\left(1 + \nabla_{\boldsymbol{x}}\eta_l \cdot \nabla_{\boldsymbol{x}}\eta_l\right)\left(\phi_{l,z}^2 - R\phi_{u,z}^2\right) + \frac{\sigma_i}{\rho_l}\nabla_{\boldsymbol{x}} \cdot \left[\frac{\nabla_{\boldsymbol{x}}\eta_l}{\sqrt{1 + |\nabla_{\boldsymbol{x}}\eta_l|^2}}\right],\end{aligned} \tag{80}$$

where $\phi_u^s(\boldsymbol{x}, t) = \phi_u(\boldsymbol{x}, \eta_u(\boldsymbol{x}, t), t)$, $\psi^i(\boldsymbol{x}, t) = \phi_l^i(\boldsymbol{x}, t) - R\phi_u^i(\boldsymbol{x}, t)$, and $R = \rho_u/\rho_l$ is the density ratio.

The process of the numerical experiment, based on a high-order spectral method (Alam *et al.*, 2009*b*), is outlined here. The boundary conditions are reorganized into a set of evolution equations of the wave elevation and velocity potential at the surface and interface. It can be shown that the entire flow field in the two-layer fluid is uniquely determined by the surface and interface quantities, similar to the deep water wave case (Zakharov, 1968). The evolution equations are discretized on a uniform grid in a rectangular domain with periodic boundary conditions and then integrated in time to obtain the evolution of the wave fields. The initial condition is a superposition

of individual wave components, i.e., eigenfunctions of the two-layer system, and then nonlinear waves develop and evolve dynamically in the simulation. The initial amplitudes of the surface wave components are set based on the empirical Joint North Sea Wave Project (JONSWAP) spectrum (Hasselmann *et al.*, 1973), while the internal wave components are extracted from a permanent form of internal wave solution of the Korteweg-de Vries (KdV) equation (Djordjevic & Redekopp, 1978). Key physical parameters, including the thickness of the two layers, the density ratio, and the amplitude of the internal wave, are comparable to a typical internal wave observed in the field (Stanton & Ostrovsky, 1998). The details of the simulation setup (case Kun) and validation of the numerical scheme (case Li) can be found in the Supplemental Materials.

By using the deterministic wave model, we address the major challenge in quantifying the surface signature: capturing the broadband wave motions between two distinct length scales (figure 25). The first one is the length scale of the surface waves relevant to the zebra pattern observed by satellite radars, which can be inferred from the radar electromagnetic signal wavelength, ranging from a few centimeters to a few decimeters (Martin, 2014), because water waves are visible to the radar signal only when their wavelengths are close such that Bragg scattering can occur. On the surface gravity wave spectrum (Munk, 1950), these surface waves are located near the gravity-capillary wave boundary. The second length scale is that of internal waves, which often span several hundred meters or kilometers (Perry & Schimke, 1965). In our numerical experiment, the wave motions at these two distinct length scales are captured with a sufficiently large number of wave modes.

4.3 Simulation setup and validation

To generate the initial condition for the simulation, we start with the linear wave modes of the two-layer fluid system. By neglecting the nonlinear terms in the boundary conditions, we can obtain the wave-like solution of the linearized system (Alam *et al.*, 2009*b*):

$$\eta_u = a\cos\psi, \tag{81}$$

$$\eta_l = \frac{\omega^2\cosh kh_u - g_1(k)k\sinh kh_u}{\omega^2}a\cos\varphi, \tag{82}$$

$$\phi_u = \left(\frac{g_1(k)}{\omega}\cosh kz + \frac{\omega}{k}\sinh kz\right)a\sin\varphi, \tag{83}$$

$$\phi_l = \frac{\omega^2\cosh kh_u - g_1(k)k\sinh kh_u}{\omega k\sinh kh_l}a\cosh k(z+h_u+h_l)\sin\varphi, \tag{84}$$

where $a = a(\omega, k_x, k_y)$ is the surface wave amplitude for the component (ω, k_x, k_y), $\varphi = k_x x + k_y y - \omega t$ is the phase function, $k = \sqrt{k_x^2 + k_y^2}$ is the wavenumber magnitude, and

$$g_1(k) = g\left(1 + \frac{\sigma_s}{\rho_u g}k^2\right), \tag{85}$$

$$g_2(k) = g\left[1 + \frac{\sigma_i}{(\rho_l - \rho_u)g}k^2\right]. \tag{86}$$

The (linear) dispersion relation of the waves can also be obtained (Alam *et al.*, 2009*a*; Kodaira *et al.*, 2016):

$$D(\omega, k) = (R + \coth kh_u\coth kh_l)\omega^4 - k\left[Rg_1\coth kh_u + g_1\coth kh_l\right. \tag{87}$$

$$\left. + (1-R)g_2\coth kh_u\right]\omega^2 + (1-R)g_1g_2k^2 = 0. \tag{88}$$

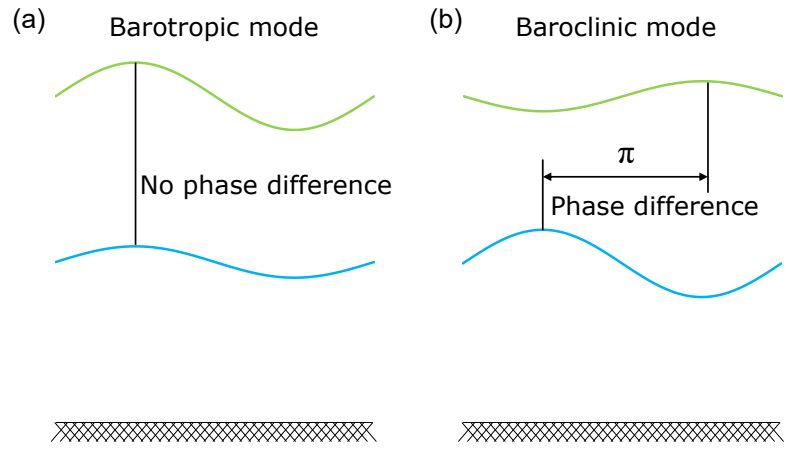

Figure 23: Eigenfunctions of the linearized two-layer fluid system: (a) barotropic mode where the surface elevation and interface elevation have the same phase; (b) baroclinic mode where the phase difference between the surface and interface elevation is π.

Given a wavenumber k, the equation $D(\omega, k) = 0$ has two solutions of ω, and the linearized system has two types of eigenfunctions: the barotropic and baroclinic modes, which can be distinguished by the phase difference between the surface and interface elevations (figure 23). The initial wave field of the simulation is generated using the sum of multiple barotropic and baroclinic modes:

$$\eta_u = \eta_{u,\mathrm{bt}} + \eta_{u,\mathrm{bc}}, \tag{89}$$

$$\eta_l = \eta_{l,\mathrm{bt}} + \eta_{l,\mathrm{bc}}, \tag{90}$$

$$\phi_u = \phi_{u,\mathrm{bt}} + \phi_{u,\mathrm{bc}}, \tag{91}$$

$$\phi_l = \phi_{l,\mathrm{bt}} + \phi_{l,\mathrm{bc}}, \tag{92}$$

where the subscripts 'bt' and 'bc' denote the barotropic and baroclinic modes, respectively.

Table 12: Physical and numerical parameters of the simulation. L_x and L_y are the computational domain size in the x and y directions, respectively. N_x and N_y are the corresponding grid numbers. λ_p is the peak wave length of the JONSWAP spectrum.

Quantity	Physical meaning	Cases Kun*	Case Li**
h_u (m)	Upper layer fluid depth	7	0.05
h_l (m)	Lower layer fluid depth	140	0.25
$R = \rho_u/\rho_l$	Density ratio	0.997	0.859
A_{iw} (m)	Amplitude of the internal solitary wave	5	0.012
L_x (m)	Domain size in x direction	500	6.0
L_y (m)	Domain size in y direction	125	0.5
N_x	Grid number in x direction	6144	768
N_y	Grid number in y direction	1536	64
λ_p (m)	Peak surface wave length	10	0.05

* Kun is a legendary fish with a length of a few thousand kilometers in Chinese mythology.
** Li is a common domesticated fish that stands for good fortune in Chinese culture, usually a few decimeters in length.

For barotropic surface wave modes, the amplitude of each wave component $a(\omega, k_x, k_y)$ is calculated from the empirical JONSWAP (Joint North Sea Wave Project) spectrum (Hasselmann *et al.*, 1973). The directional spreading function of the surface waves is assumed to be $D(\theta) = (2/\pi)\cos^2\theta$ (Young, 1999). A random number is assigned to the initial phase of each wave component. To reconstruct the baroclinic (internal) wave modes, we use a solitary wave form of $\eta_{l,\mathrm{bc}} = A_{iw}\mathrm{sech}^2\left[(x - x_0)/L_x\right] - C$ (Kodaira *et al.*, 2016). Here x_0 is the initial location of the internal wave trough, and C is a constant chosen to eliminate the mean of $\eta_{l,\mathrm{bc}}$. We then obtain $a(\omega, k_x, k_y)$ by taking the inverse Fourier transform of $\eta_{l,\mathrm{bc}}$. The computational domain is rectangular with an area of 500 m by 125 m, sufficiently large to cover the entire internal wave. The initial condition is thus generated with the information of wave amplitude for the barotropic wave modes and baroclinic wave modes. In the simulation of this case, the surface tension forces at the surface and interface are negligibly small, and

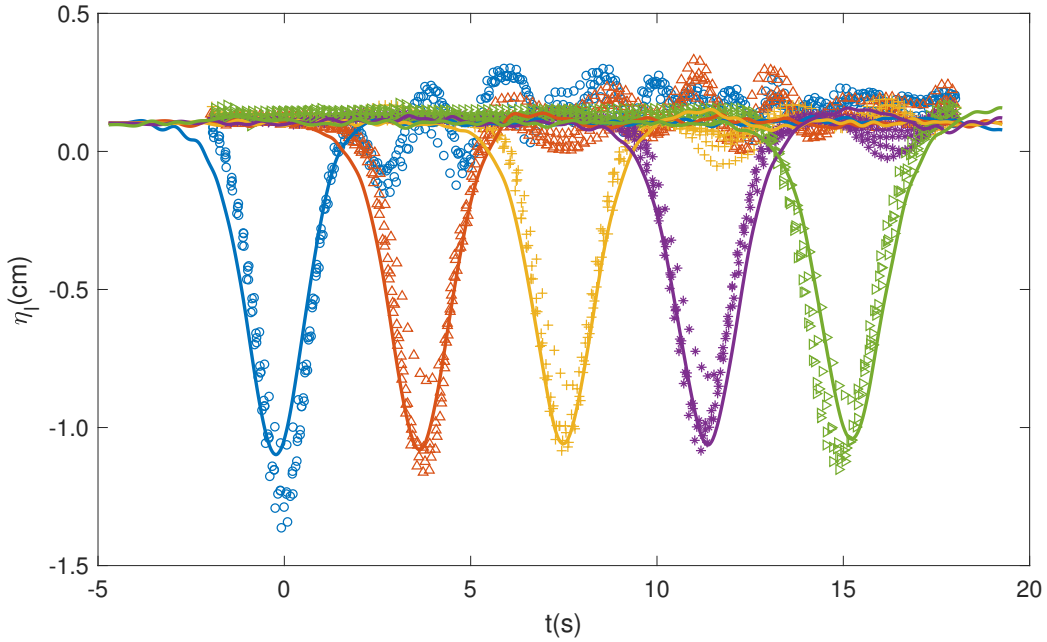

Figure 24: Time history of the interface elevation η_l at five locations. Our numerical result is denoted by lines, and the laboratory measurement (Kodaira *et al.*, 2016) by symbols.

therefore the associated terms are not computed to speed up the simulation speed. The physical and numerical parameters are presented in Table 12 (case Kun).

For the validation purpose, we conduct an auxiliary experiment (case Li in Table 12) where the parameters are adapted from a recent laboratory measurement (Kodaira *et al.*, 2016). We track the time history of the internal wave profile at five different locations, similar to the probes in the laboratory experiment setup. Note that in case Li, we calculate the pressure due to surface tension at both the surface and the interface because the shortest wavelength falls in the capillary-gravity wave range. As shown in figure 24, our result is consistent with the laboratory measurement, indicating that the dynamics of internal wave are captured.

4.4 Results

The surface signature can be directly observed from the surface elevation with naked eyes (Woodson, 2018). In the simulation, the initial surface wave field is statistically homogeneous and the surface signature is found to form gradually and maintain throughout the simulation. We present an example of the instantaneous surface elevation and the interface elevation in figure 25. As shown, a rough surface region with increased wave steepness is formed above the leading edge of the internal wave. Right behind the rough region exists a smooth region where the surface wave steepness is significantly reduced. The rough and smooth regions correspond to a pair of bright and dark bands on satellite images. Note that there is no definite boundary between the surface signature and the background surface wave field. The total length of the surface signature is over 100 m, while the waves associated with the roughness change have much smaller length scales. The rough and smooth regions are found to propagate at the same speed as the internal wave, which remains constant throughout the simulation.

In case Kun, the phase speed of the internal wave is found to be approximately 0.52 m/s, much smaller than the surface wave celerity of a similar length scale, for instance, a 200 m swell propagating at 17.7 m/s. For comparison, we also calculate the theoretical internal wave phase speed in the asymptotic limit of nonlinearity. For weak nonlinearity, the phase speed is given by the Korteweg-de Vries (KdV) equation (Djordjevic & Redekopp, 1978):

$$c_1 = \left(1 + \frac{A_{iw}}{2h_u h_l}\frac{\rho_l h_u^2 - \rho_u h_l^2}{\rho_l h_u + \rho_u h_l}\right)\sqrt{\frac{g(\rho_l - \rho_u)h_u h_l}{\rho_u h_l + \rho_l h_u}} = 0.59 \text{ m/s}. \tag{93}$$

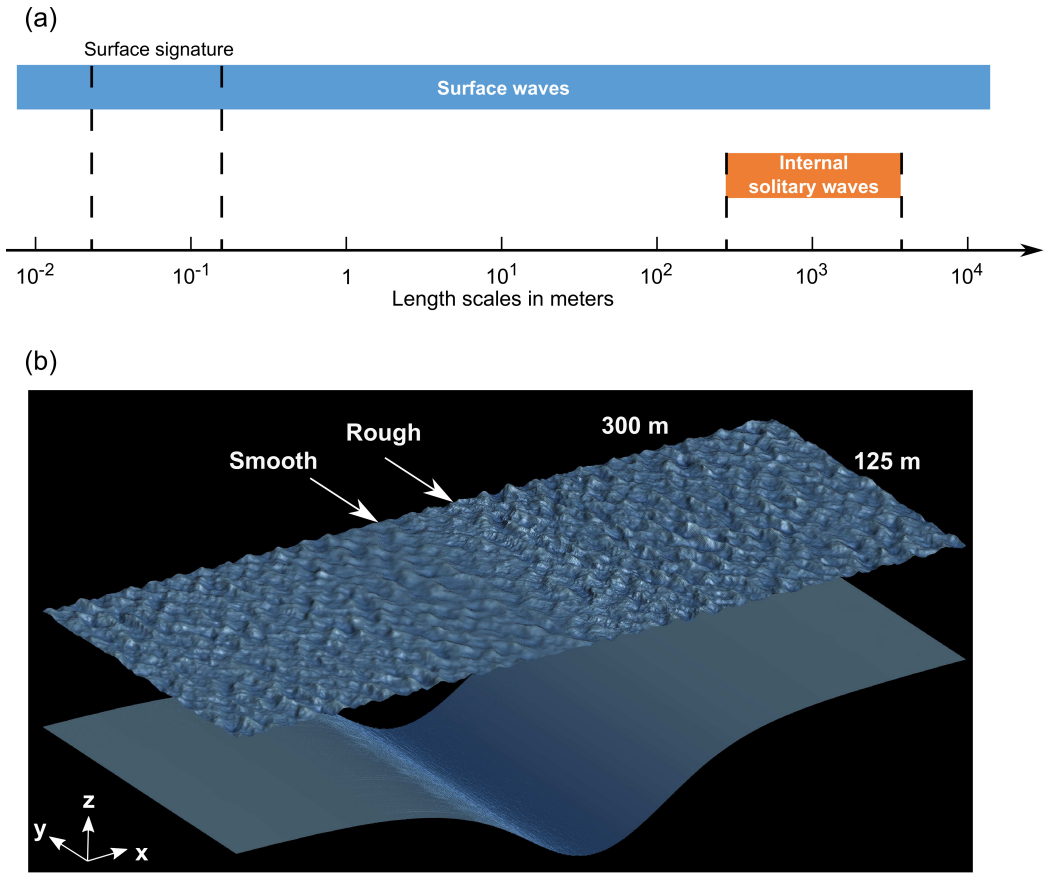

Figure 25: (a) Length scales of the surface signature and internal waves. (b) Direct observation of the surface signature, denoted by the instantaneous surface wave elevation field. Also plotted is the interface elevation, denoting the internal wave profile. For clarity, we only plot part of the computational domain. The internal wave is propagating in the $+x$ direction.

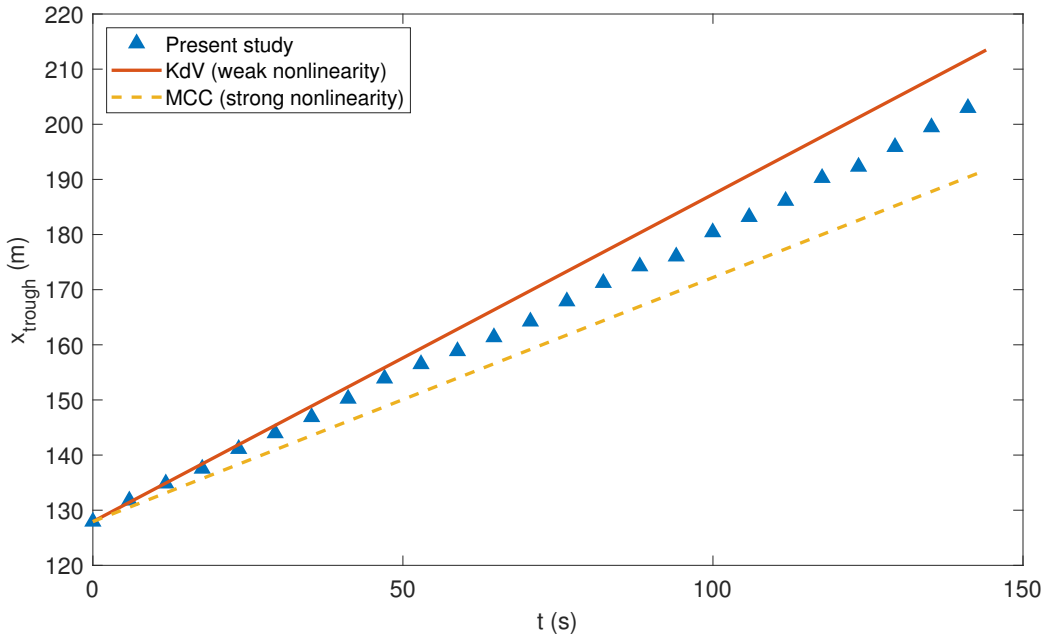

Figure 26: Time history of the location of the internal wave trough. Also plotted are the theoretical results in the weak and strong nonlinearity limit (Djordjevic & Redekopp, 1978; Miyata, 1985; Choi & Camassa, 1996; Barros *et al.*, 2007).

In the strong nonlinearity limit, the wave speed can be estimated by the Miyata-Choi-Camassa (MCC) model (Miyata, 1985; Choi & Camassa, 1996; Barros *et al.*, 2007):

$$c_2 = \sqrt{\frac{gh_u h_l(1-R)}{h_u + h_l}} = 0.44 \text{ m/s}. \tag{94}$$

Compared with these asymptotic cases, the internal wave in case Kun has a moderate nonlinearity, as shown by figure 26. Initially, our result is closer to the weakly nonlinear KdV prediction, while at the later time the nonlinearity slightly increases. Overall, the speed of internal wave remains a constant, presenting a moderate nonlinearity.

To quantify the motions induced by the internal wave, we calculate the surface current by performing the following averaging:

$$U(x) = \frac{1}{L_y(t_2 - t_1)} \int_{t_1}^{t_2} \int_0^{L_y} u(x - c_{iw}t, y, t) \mathrm{d}y \mathrm{d}t, \tag{95}$$

where t_1 and t_2 denote two different time instants. The effectiveness of the averaging operator relies on two assumptions: the scale separation between the background surface waves and the internal wave, and the homogeneity of the internal wave motion in the y direction. The first assumption holds since the peak surface wave length is much smaller than the length scale of internal wave, i.e., $\lambda_p << L_x$. The validity of the second assumption is less intuitive, especially because the governing equations pose no constraints in the y direction. Throughout the simulation, we found the internal wave to be de facto one dimensional, with variations in the x direction. The first-order approximation of the current can be estimated from mass conservation: $-c_{iw}\eta_l/(h_u - \eta_l) - C_0$, where C_0 is a constant to ensure that the mean is zero. Overall,

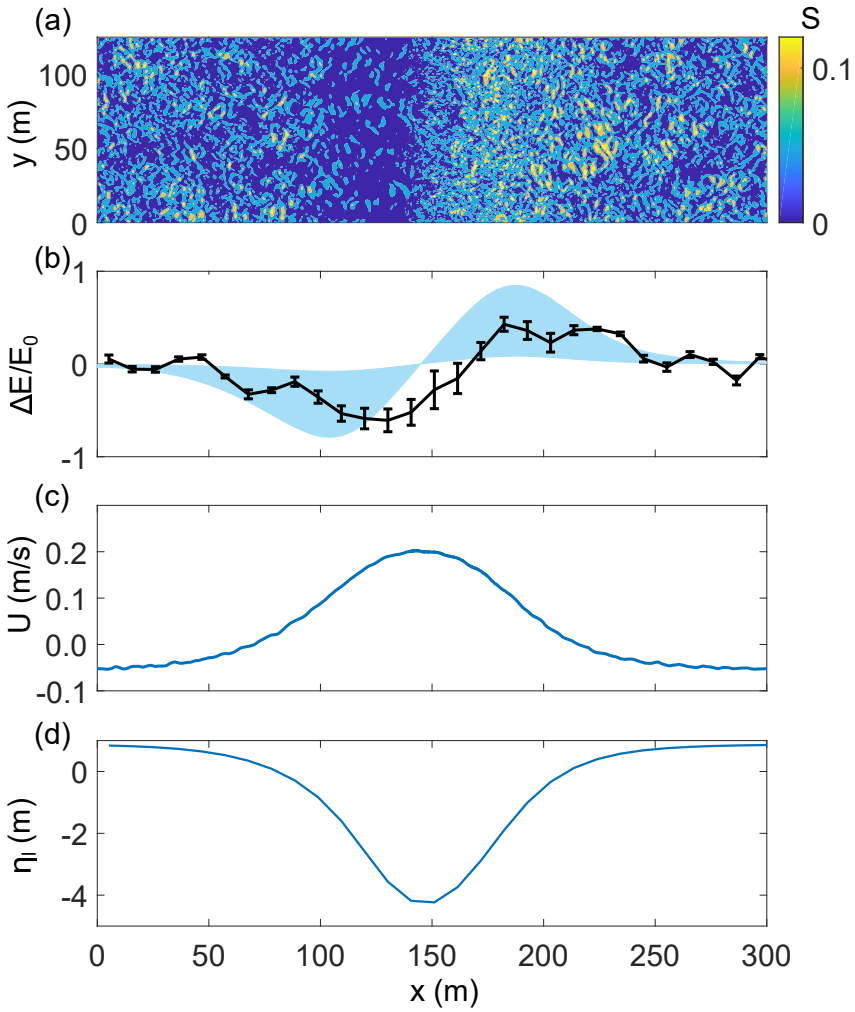

Figure 27: Quantitative analysis of the surface signature. (a) Plan view of the instantaneous local steepness $S = [(\partial\eta_u/\partial x)^2 + (\partial\eta_u/\partial y)^2]^{1/2}$ of the surface wave field, where η_u is the surface elevation. (b) The change in surface wave energy ΔE normalized by the unperturbed value E_0. The shaded area in light blue denotes the range of $\Delta E/E_0 = -4.5\tau(\mathrm{d}U/\mathrm{d}x)$ with $\tau = 4.7 - 47$ s (Alpers, 1985). (c) Surface current induced by the internal wave. (d) Profile of the internal wave denoted by the interface elevation η_l.

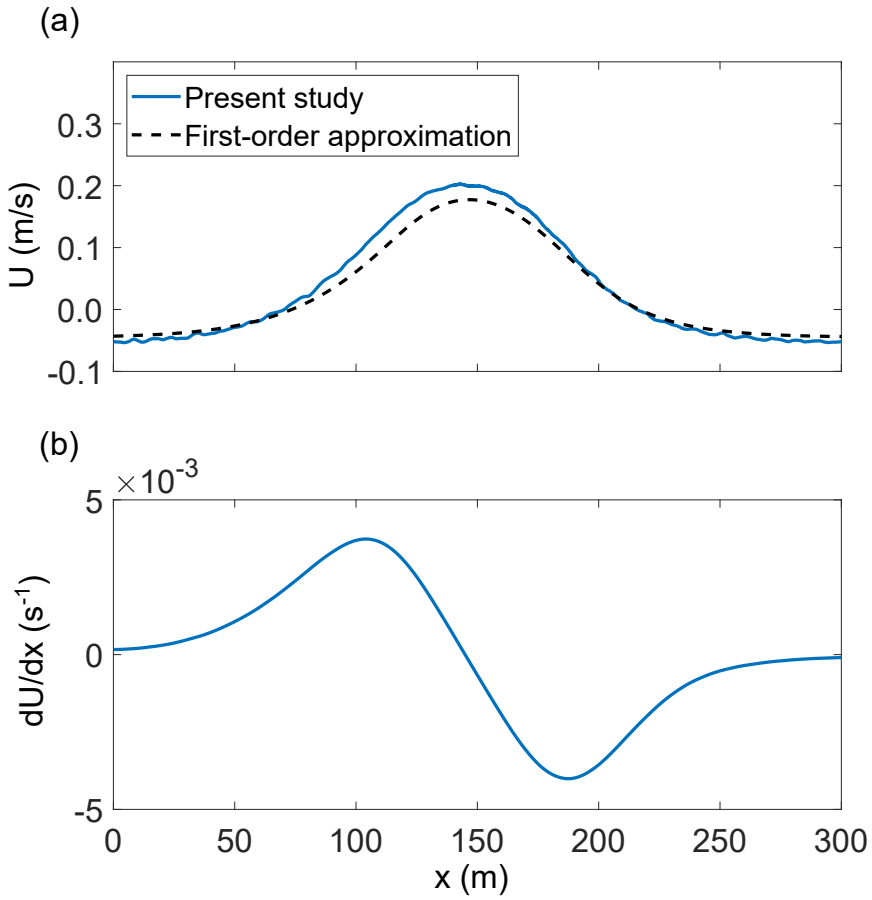

Figure 28: (a) Surface current compared with the first order approximation. (b) Gradient of the surface current.

the two results agree with each other except for some deviations in the region above the internal wave trough (figure 28a).

The gradient of the current $\mathrm{d}U/\mathrm{d}x$, shown in figure 28(b), is then calculated from $U(x)$. Instead of direct calculation with a finite difference method, we estimate $\mathrm{d}U/\mathrm{d}x$ by minimizing the following functional to avoid extreme values caused by irregularity

and noise in $U(x)$ (Chartrand, 2011):

$$\mathcal{G}(f) = \alpha \int_0^{L_x} |f'|^2 \, \mathrm{d}x + \frac{1}{2} \int_0^{L_x} \left| \int_0^x f(\xi) d\xi - U(x) \right| \mathrm{d}x, \tag{96}$$

where α is a parameter to control the balance between these two terms. Note that if $\alpha = 0$, the optimal solution would be $f(x) = \mathrm{d}U/\mathrm{d}x$ in theory.

To quantify the roughness change, we calculate the local steepness defined as $S = [(\partial \eta_u/\partial x)^2 + (\partial \eta_u/\partial y)^2]^{1/2}$ (figure 27a). The wave steepness in the rough region is higher than that in the smooth region in a statistical sense. As shown in figure 27(b), the surface wave energy change $\Delta E/E_0$ calculated from the wavenumber spectrum can also reveal the surface signature pattern. We divide the computational domain into 48 regions along the x direction, each with a size of 10.4 m $\times$ 125 m. Then we conduct 2D Fourier transform on the product of the surface elevation $\eta_u(x, y)$ and a window function in each region and obtain the wavenumber spectrum $E(k_x, k_y)$. Considering that the surface wave field should be statistically homogeneous in the y direction, we perform averaging to obtain the 1D wavenumber spectrum $E(k_x) = \int E(k_x, k_y) \mathrm{d}k_y$. The surface wave energy change is then computed by:

$$\frac{\Delta E}{E_0} = \sum_{k_x} \frac{E(k_x) - E_0(k_x)}{E_0(k_x)}. \tag{97}$$

To clarify the correlation between the wave energy change and the surface motion induced by the internal wave, we provide another estimation according to the formula proposed in (Alpers, 1985):

$$\frac{\Delta E}{E_0} = -4.5\tau \frac{\mathrm{d}U}{\mathrm{d}x}, \tag{98}$$

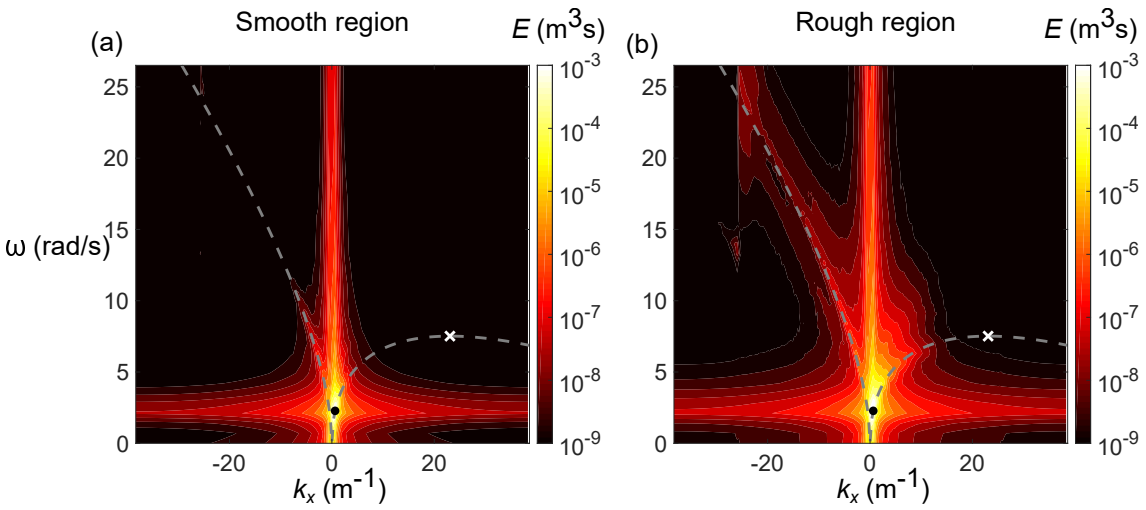

Figure 29: Wavenumber-frequency spectrum of surface waves in the (a) smooth region and (b) rough region. The spectrum is calculated in the moving frame of reference with the internal wave. The dashed curves denote the dispersion relation of the surface waves in the moving frame of reference: $\omega = (U_m - c_{iw})k_x + \sqrt{g\,|k_x|}$, where U_m is the maximum value of the surface current U (see figure 27). The white cross denotes the maximum frequency of the right-moving surface wave $\omega_m = -g/4(U_m - c_{iw})$. The black filled circle denotes the peak surface wave.

where $\tau = 4.7 - 47$ s is an empirical relaxation time and $\mathrm{d}U/\mathrm{d}x$ is the gradient of the surface current. Overall, the results are consistent and show the same trend in the wave energy change which sees an apparent correlation with the current gradient. Note that the surface current (figure 27c) is geometrically similar to the internal wave profile (figure 27d) because of mass conservation.

After the smooth and rough regions are formed, the resulting surface wave field becomes inhomogeneous in the physical space. We conduct spectral analysis on the surface elevation in the frame of reference traveling with the internal wave. The data is extracted from two domains above the internal wave trough, one in the smooth region and the other in the rough region. We extract the surface elevation data from the smooth region and rough region, respectively (figure 30). These two sub-

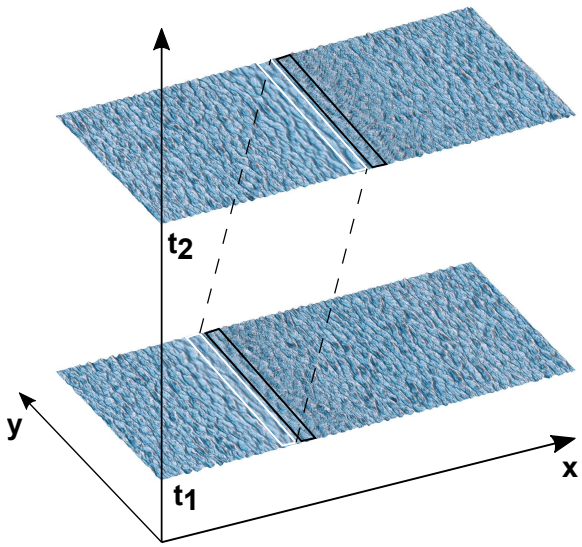

Figure 30: Surface wave field in the four-dimensional space. The surface elevation in the white box is used for spectral analysis in the smooth region, while that in the black box is for the rough region.

domains for spectral analysis are located near the boundary between the smooth and rough regions, where the magnitude of the surface current is maximum. The size of each subdomain is 21 m $\times$ 125 m. In the x direction, the subdomain size cannot be too large. Otherwise, spectral analysis would be invalid because of the spatial variation of the wave field. The wavenumber-frequency spectrum $E(k_x, k_y, \omega)$ is then separately calculated in each subdomain. For clarity, the integrated spectrum $E(k_x, \omega) = \int E(k_x, k_y, \omega) \mathrm{d}k_y$ is calculated for visualization.

From the contours of the wavenumber-frequency spectra (figure 29), we can separately identify the energy associated with the two different eigenfunctions: the baroclinic mode energy is located in the low frequency and low wavenumber portion, while the barotropic mode energy is primarily along the dispersion relation curve of the surface wave in the moving frame of reference as shown by the dashed lines. In the moving

frame, the surface motion induced by the internal wave is a countercurrent because $U - c_{iw} < 0$. As a result, there exists a maximum frequency $\omega_m = -g/4(U_m - c_{iw})$ for surface waves propagating against the current (Donato *et al.*, 1999; Nardin *et al.*, 2009). The surface signature can be identified from the difference in the energy of left-moving ($k_x < 0$) surface waves between the smooth region and the rough region. Surface waves with smaller wavenumbers, for instance, the peak wave, are less affected by the surface current induced by the internal wave. When the surface waves are quasi-monochromatic, their properties experience a change as they enter a potential well formed by the internal wave (Craig *et al.*, 2012). Similarly in this study, the short waves in the rough region (figure 29b) are in a bound state and cannot propagate freely, which correspond to the short wave packets observed at the surface of two-layer fluids in the recent laboratory experiment (Kodaira *et al.*, 2016).

4.5 Conclusions

We have presented the first simulation to directly capture the surface roughness signature induced by an internal wave. Our results show that the formation of the surface signature is essentially an energy conservative process. In other words, energy sources and sinks including wind input and wave breaking are not the direct cause of the surface signature. With the surface wave and internal wave dynamics captured, the surface signature is quantified using the wave geometry in the physical space and the energy change in the spectral space. Admittedly, we have neglected the effects of the stratification associated with the continuous density profile, turbulence, and the strong nonlinearity in internal waves, which can be captured by solving the full three dimensional Navier-Stokes equations, yet at a considerably high computa-

tional cost due to the length scale separation (figure 25). For practical applications in oceanography, the quantified surface signature can now be directly connected to the internal wave properties through a numerical simulation before in-situ measurements are made. The wave-phase-resolved surface signature will be especially useful by providing hydrodynamic information to radar electromagnetic signal simulations in oceanic remote sensing (Chen *et al.*, 1992; Franceschetti *et al.*, 1998; Liu & He, 2016; Yoshida, 2017), which are nowadays conducted on artificially generated ocean surfaces.

5 Concluding Remarks

5.1 Contributions of this thesis

In this study, we have conducted the first wind and wave coupled simulation for a long duration up to $O(3000)$ peak wave periods with the wave phases and turbulence eddies resolved, based on a computational framework developed by Yang & Shen (2011*a*,*b*) and Yang, Meneveau & Shen (2013). The wave field evolves for a long duration up to $O(3000)$ peak wave periods to have appreciable change in the wave spectrum. We have discovered the wave signature on wind turbulence and substantiated the self-similarity-based wave evolution law (Zakharov *et al.*, 2015). We have contributed to the fundamental understanding of the long-term wind-forced wave field evolution, and pave the way for future wind–wave studies from the deterministic perspective.

We have also identified wave shoaling as a main reason for the increased wind–wave momentum transfer in the coastal region. The simulations address the critical need of resolving the wind turbulence and capturing the wave dynamics, as suggested by the field studies in literature. To the best of our knowledge, this is the first comprehensive simulation-based study of its kind focusing on the coastal wind–wave momentum transfer, whereas in previous numerical studies that involve the investigation of momentum transfer (e.g., Sullivan, Mcwilliams & Moeng, 2000; Yang & Shen, 2010; Druzhinin, Troitskaya & Zilitinkevich, 2012; Sullivan, McWilliams & Patton, 2014), the waves are all in open seas. This knowledge will be especially useful for improving the performance of regional climate models in the coastal region.

Our direct simulation based on the two-layer model solves a decades-long problem to directly capture the surface roughness signature induced by an internal wave.

Our results show that the formation of the surface signature is essentially an energy conservative process. In other words, energy sources and sinks including wind input and wave breaking are not the direct cause of the surface signature. With the surface wave and internal wave dynamics captured, the surface signature is quantified using the wave geometry in the physical space and the energy change in the spectral space. For practical applications in oceanography, the quantified surface signature can now be directly connected to the internal wave properties through a numerical simulation before in-situ measurements are made.

5.2 Future studies

5.2.1 Quantitative study of long-term wave evolution

The deterministic wind–wave simulation used in this study is a valuable research tool, but is also computationally demanding (for example, a typical case takes about two months to run on a parallel computer using 384 cores). This poses challenges to further increase the evolution period of the wave field with the existing computer power. In the future, with the increase of computer power, when the simulations can be carried out for much longer evolution periods, it would be helpful to provide further quantitative analysis on the wave evolution process when the wave properties, including the total wave energy, peak wavenumber and peak wave frequency, are plotted as functions of time or fetch. These functions are valuable to the further assessment of the wave turbulence theory (see Badulin *et al.*, 2005; Gagnaire-Renou *et al.*, 2011) and may provide additional support for the significance of nonlinear interactions in the wind-forced wave evolution. The computation framework developed in this study

will be useful for such studies.

5.2.2 Wind–wave interaction at extreme conditions

At extreme conditions such as a hurricane, wave breaking frequently occurs. The energy dissipation of wave breaking is excluded in the analysis of the present study on wind–wave interaction. In the design of our numerical experiments, we deliberately chose relatively weak wind speeds to reduce the impact of wave breaking that cannot be directly resolved by a prescribed monochromatic wave or the HOS method due to the potential flow assumption. The complexity of wave breaking requires substantial work in modelling and validation, which is beyond the scope of this study. In future study, it will be beneficial to improve the heuristic wave breaking model in the present numerical tool to better capture the energy dissipation caused by different types of breakers (Melville, 1996; Duncan, 2001; Perlin *et al.*, 2013)).

5.2.3 Surface wave signature induced by stratified flow

To facilitate the phase-resolved simulation that simultaneously capture surface wave and internal wave dynamics, we have neglected the effects of the stratification associated with the continuous density profile, turbulence, and the strong nonlinearity in internal waves, which can be captured by solving the full three dimensional Navier-Stokes equations, yet at a considerably high computational cost due to the length scale separation. An enhanced computing power in the future will enable these studies with more realistic physical configurations.

5.2.4 Multi-physics simulation for remote sensing of surface waves

With the advancement in the radar electromagnetic signal simulations in oceanic remote sensing Chen *et al.* (1992); Franceschetti *et al.* (1998); Liu & He (2016); Yoshida (2017), it is now possible to conduct multi-physics simulation that resolve key processes in physical optics and hydrodynamics. The phase-resolved surface wave field, with the impact from wind and oceanic internal waves captured, will be especially useful by providing hydrodynamic information to the radar simulation, which are nowadays conducted on artificially generated ocean surfaces.

References

Agafontsev, D. S. & Zakharov, V. E. 2015 Intermittency in generalized NLS equation with focusing six-wave interactions. *Phys. Lett. A* **379** (40-41), 2586–2590.

Agnon, Y. & Sheremet, A. 1997 Stochastic nonlinear shoaling of directional spectra. *J. Fluid Mech.* **345**, 79–99.

Alam, M.-R., Liu, Y. & Yue, D. K. P. 2009*a* Bragg resonance of waves in a two-layer fluid propagating over bottom ripples. Part I. Perturbation analysis. *J. Fluid Mech.* **624**, 191–224.

Alam, M.-R., Liu, Y. & Yue, D. K. P. 2009*b* Bragg resonance of waves in a two-layer fluid propagating over bottom ripples. Part II. Numerical simulation. *J. Fluid Mech.* **624**, 225–253.

Alpers, W. 1985 Theory of radar imaging of internal waves. *Nature* **314**, 245–247.

Annenkov, S. Y. & Shrira, V. I. 2013 Large-time evolution of statistical moments of wind-wave fields. *J. Fluid Mech.* **726**, 517–546.

Annenkov, S. Y. & Shrira, V. I. 2014 Evaluation of skewness and kurtosis of wind waves parameterized by JONSWAP spectra. *J. Phys. Oceanogr.* **44** (6), 1582–1594.

Apel, J. R. 1988 *Principles of ocean physics*. London; Orlando: Academic Press.

Ardhuin, F. & Herbers, T. H. C. 2002 Bragg scattering of random surface gravity waves by irregular seabed topography. *J. Fluid Mech.* **451**, 1–33.

Ardhuin, F., Roland, A., Dumas, F., Bennis, A.-C., Sentchev, A., Forget, P., Wolf, J., Girard, F., Osuna, P. & Benoit, M. 2012 Numerical wave modeling in conditions with strong currents: dissipation, refraction, and relative wind. *J. Phys. Oceanogr.* **42** (12), 2101–2120.

Badulin, S. I., Babanin, A. V., Zakharov, V. E. & Resio, D. T. 2007 Weakly turbulent laws of wind-wave growth. *J. Fluid Mech.* **591**, 339–378.

Badulin, S. I., Pushkarev, A. N., Resio, D. T. & Zakharov, V. E. 2005 Self-similarity of wind-driven seas. *Nonlinear Process. Geophys.* **12** (6), 891–945.

Bakhanov, V. V. & Ostrovsky, L. A. 2002 Action of strong internal solitary waves on surface waves. *J. Geophys. Res. Ocean.* **107** (C10), 3139.

Banner, M. L. & Melville, W. K. 1976 On the separation of air flow over water waves. *J. Fluid Mech.* **77** (04), 825–842.

Barnard, P. L., Short, A. D., Harley, M. D., Splinter, K. D., Vitousek, S., Turner, I. L., Allan, J., Banno, M., Bryan, K. R., Doria, A., Hansen, J. E., Kato, S., Kuriyama, Y., Randall-Goodwin, E., Ruggiero, P., Walker, I. J. & Heathfield, D. K. 2015 Coastal vulnerability across the Pacific dominated by El Niño/Southern Oscillation. *Nat. Geosci.* **8** (10), 801–807.

Barros, R, Gavrilyuk, S. L. & Teshukov, V. M. 2007 Dispersive nonlinear waves in two-layer flows with free surface. I. model derivation and general properties. *Stud. Appl. Math.* **119** (3), 191–211.

Belcher, S. E. & Hunt, J. C. R. 1993 Turbulent shear flow over slowly moving waves. *J. Fluid Mech.* **251**, 109–148.

Belibassakis, K. A. & Athanassoulis, G. A. 2002 Extension of second-order Stokes theory to variable bathymetry. *J. Fluid Mech.* **464**, 35–80.

Buckley, M. P. & Veron, F. 2016 Structure of the airflow above surface waves. *J. Phys. Oceanogr.* **46** (5), 1377–1397.

Buckley, M. P. & Veron, F. 2017 Airflow measurements at a wavy air–water interface using PIV and LIF. *Exp. Fluids* **58** (11), 161.

Burling, R. W. 1959 The spectrum of waves at short fetches. *Dtsch. Hydrogr. Zeitschrift* **12** (3), 96–117.

Calaf, M., Meneveau, C. & Meyers, J. 2010 Large eddy simulation study of fully developed wind-turbine array boundary layers. *Phys. Fluids* **22** (1), 015110.

Campbell, B. K., Hendrickson, K. & Liu, Y. 2016 Nonlinear coupling of interfacial instabilities with resonant wave interactions in horizontal two-fluid plane Couette-Poiseuille flows: numerical and physical observations. *J. Fluid Mech.* **809**, 438–479.

Casulli, V. & Stelling, G. S. 1998 Numerical simulation of 3D quasi-hydrostatic, free-surface flows. *J. Hydraul. Eng.* **124** (7), 678–686.

Caulliez, G. 2013 Dissipation regimes for short wind waves. *J. Geophys. Res. Ocean.* **118** (2), 672–684.

Cavaleri, L., Alves, J.-H.G.M., Ardhuin, F., Babanin, A. V., Banner, M. L., Belibassakis, K., Benoit, M., Donelan, M. A., Groeneweg, J., Herbers, T. H. C., Hwang, P. A., Janssen, P. A. E. M., Janssen, T., Lavrenov, I. V., Magne, R., Monbaliu, J., Onorato, M., Polnikov, V., Resio, D. T., Rogers, W. E., Sheremet, A., McKee Smith, J., Tolman, H. L., van Vledder, G., Wolf, J. & Young, I. R. 2007 Wave modelling – The state of the art. *Prog. Oceanogr.* **75** (4), 603–674.

Chalikov, D., Babanin, A. V. & Sanina, E. 2014 Numerical modeling of 3D fully nonlinear potential periodic waves. *Ocean Dyn.* **64** (10), 1469–1486.

Chalikov, D. V. 2016 *Numerical modeling of sea waves*. Cham: Springer International Publishing.

Chalikov, D. V. & Belevich, M. Y. 1993 One-dimensional theory of the wave boundary layer. *Boundary-Layer Meteorol.* **63** (1-2), 65–96.

Chamberlain, P. G. & Porter, D. 1995 The modified mild-slope equation. *J. Fluid Mech.* **291**, 393–407.

Charnock, H. 1955 Wind stress on a water surface. *Q. J. R. Meteorol. Soc.* **81** (350), 639–640.

Chartrand, R. 2011 Numerical differentiation of noisy, nonsmooth data. *ISRN Appl. Math.* **2011**, 164564.

Chen, K. S., Fung, A. K. & Weissman, D. A. 1992 A backscattering model for ocean surface. *IEEE Trans. Geosci. Remote Sens.* **30** (4), 811–817.

Choi, H., Moin, P. & Kim, J. 1994 Active turbulence control for drag reduction in wall-bounded flows. *J. Fluid Mech.* **262**, 75–110.

Choi, W. & Camassa, R. 1996 Long internal waves of finite amplitude. *Phys. Rev. Lett.* **77** (9), 1759–1762.

Craig, W., Guyenne, P. & Sulem, C. 2012 The surface signature of internal waves. *J. Fluid Mech.* **710**, 277–303.

Davis, J., Sheremet, A., Tian, M. & Saxena, S. 2014 A numerical implementation of a nonlinear mild slope model for shoaling directional waves. *J. Mar. Sci. Eng.* **2** (1), 140–158.

Dean, R. G. & Dalrymple, R. A. 1991 *Water wave mechanics for engineers and scientists*. Singapore; Teaneck, NJ: World Scientific.

Dean, R. G. & Dalrymple, R. A. 2001 *Coastal processes with engineering applications*. Cambridge University Press.

DeLeonibus, P. S. & Simpson, L. S. 1972 Case study of duration-limited wave spectra observed at an open ocean tower. *J. Geophys. Res.* **77** (24), 4555–4569.

Deng, B.-Q. & Xu, C.-X. 2012 Influence of active control on STG-based generation of streamwise vortices in near-wall turbulence. *J. Fluid Mech.* **710**, 234–259.

Dingemans, M. W. 1997 *Water wave propagation over uneven bottoms*. River Edge, NJ: World Scientific.

Djordjevic, V. D. & Redekopp, L. G. 1978 The fission and disintegration of internal solitary waves moving over two-dimensional topography. *J. Phys. Oceanogr.* **8** (6), 1016–1024.

Dommermuth, D. G. & Yue, D. K. P. 1987 A high-order spectral method for the study of nonlinear gravity waves. *J. Fluid Mech.* **184**, 267–288.

Donato, A. N., Peregrine, D. H. & Stocker, J. R. 1999 The focusing of surface waves by internal waves. *J. Fluid Mech.* **384**, 27–58.

Donelan, M. 1979 On the fraction of wind momentum retained by waves. In *Mar. Forecast.* (ed. J. C. J. Nihoul), pp. 141–159. Elsevier.

Donelan, M. A. 1999 Wind-induced growth and attenuation of laboratory waves. In *Wind. Couplings Perspect. Prospect.* (ed. S. G. Sajjadi, N. H. Thomas & J. C. R. Hunt), pp. 183–194. Clarendon.

Donelan, M. A. 2004 On the limiting aerodynamic roughness of the ocean in very strong winds. *Geophys. Res. Lett.* **31** (18), L18306.

Donelan, M. A., Babanin, A. V., Young, I. R. & Banner, M. L. 2006 Wave-follower field measurements of the wind-input spectral function. Part II: Parameterization of the wind input. *J. Phys. Oceanogr.* **36** (8), 1672–1689.

Donelan, M. A. & Pierson, W. J. 1987 Radar scattering and equilibrium ranges in wind-generated waves with application to scatterometry. *J. Geophys. Res.* **92** (C5), 4971–5029.

Druzhinin, O. A., Troitskaya, Y. I. & Zilitinkevich, S. S. 2012 Direct numerical simulation of a turbulent wind over a wavy water surface. *J. Geophys. Res. Ocean.* **117**, 1–16.

Duncan, J. H. 2001 Spilling breakers. *Annu. Rev. Fluid Mech.* **33** (1), 519–547.

Dysthe, K., Krogstad, H. E. & Müller, P. 2008 Oceanic rogue waves. *Annu. Rev. Fluid Mech.* **40** (1), 287–310.

Dysthe, K. B. 2001 Refraction of gravity waves by weak current gradients. *J. Fluid Mech.* **442**, 157–159.

Edson, J., Crawford, T., Crescenti, J., Farrar, T., Frew, N., Gerbi, G., Helmis, C., Hristov, T., Khelif, D., Jessup, A., Jonsson, H., Li, M., Mahrt, L., McGillis, W., Plueddemann, A., Shen, L., Skyllingstad, E., Stanton, T., Sullivan, P., Sun, J., Trowbridge, J., Vickers, D., Wang, S., Wang, Q., Weller, R., Wilkin, J., Williams, A. J., Yue, D. K. P. & Zappa, C. 2007 The coupled boundary layers and air-sea transfer experiment in low winds. *Bull. Am. Meteorol. Soc.* **88** (3), 341–356.

Edson, J. B., Jampana, V., Weller, R. A., Bigorre, S. P., Plueddemann, A. J., Fairall, C. W., Miller, S. D., Mahrt, L., Vickers, D. & Hersbach, H. 2013 On the exchange of momentum over the open ocean. *J. Phys. Oceanogr.* **43** (8), 1589–1610.

Engsig-Karup, A. P., Bingham, H. B. & Lindberg, O. 2009 An efficient flexible-order model for 3D nonlinear water waves. *J. Comput. Phys.* **228** (6), 2100–2118.

Euvé, L. P., Michel, F., Parentani, R. & Rousseaux, G. 2015 Wave blocking and partial transmission in subcritical flows over an obstacle. *Phys. Rev. D - Part. Fields, Gravit. Cosmol.* **91** (2), 024020.

Fedele, F., Brennan, J., Ponce De León, S., Dudley, J. & Dias, F. 2016 Real world ocean rogue waves explained without the modulational instability. *Sci. Rep.* **6** (May), 1–11.

Ferrari, R. & Wunsch, C. 2009 Ocean circulation kinetic energy: reservoirs, sources, and sinks. *Annu. Rev. Fluid Mech.* **41** (1), 253–282.

Flores, O. & Jiménez, J. 2010 Hierarchy of minimal flow units in the logarithmic layer. *Phys. Fluids* **22** (7), 071704.

Franceschetti, G., Migliaccio, M. & Riccio, D. 1998 On ocean SAR raw signal simulation. *IEEE Trans. Geosci. Remote Sens.* **36** (1), 84–100.

Gagnaire-Renou, E., Benoit, M. & Badulin, S. I. 2011 On weakly turbulent scaling of wind sea in simulations of fetch-limited growth. *J. Fluid Mech.* **669**, 178–213.

García-Nava, H., Ocampo-Torres, F. J., Osuna, P. & Donelan, M. A. 2009 Wind stress in the presence of swell under moderate to strong wind conditions. *J. Geophys. Res. Ocean.* **114** (C12), C12008.

Garratt, J. R. 1977 Review of drag coefficients over oceans and continents. *Mon. Weather Rev.* **105** (7), 915–929.

Garratt, J. R. 1990 The internal boundary layer–a review. *Boundary-Layer Meteorol.* **50** (1-4), 171–203.

Geernaert, G. L. 1990 Bulk parameterizations for the wind stress and heat fluxes. In *Surf. waves fluxes. Vol. I-current theory* (ed. G. L. Geernaert & W. L. Plant), *Environmental Fluid Mechanics*, vol. 7, pp. 91–172. Springer Netherlands.

Geernaert, G. L., Katsaros, K. B. & Richter, K. 1986 Variation of the drag coefficient and its dependence on sea state. *J. Geophys. Res.* **91** (C6), 7667–7679.

Germano, M., Piomelli, U., Moin, P. & Cabot, W. H. 1991 A dynamic subgrid-scale eddy viscosity model. *Phys. Fluids A Fluid Dyn.* **3** (7), 1760.

de Giovanetti, M., Hwang, Y. & Choi, H. 2016 Skin-friction generation by attached eddies in turbulent channel flow. *J. Fluid Mech.* **808**, 511–538.

Grare, L., Peirson, W. L., Branger, H., Walker, J. W., Giovanangeli, J.-P. & Makin, V. 2013 Growth and dissipation of wind-forced, deep-water waves. *J. Fluid Mech.* **722**, 5–50.

Hara, T. & Sullivan, P. P. 2015 Wavy boundary layer turbulence over surface waves in a strongly forced condition. *J. Phys. Oceanogr.* **45**, 868–883.

Hasselmann, K. 1962 On the non-linear energy transfer in a gravity-wave spectrum. Part 1. General theory. *J. Fluid Mech.* **12** (04), 481–500.

Hasselmann, K. 1963*a* On the non-linear energy transfer in a gravity-wave spectrum. Part 2. Conservation theorems; wave-particle analogy; irreversibility. *J. Fluid Mech.* **15** (02), 273–281.

Hasselmann, K. 1963*b* On the non-linear energy transfer in a gravity-wave spectrum. Part 3. Evaluation of the energy flux and swell-sea interaction for a Neumann spectrum. *J. Fluid Mech.* **15** (03), 385–398.

Hasselmann, K., Barnett, T. P., Bouws, E., Carlson, H., Cartwright, D. E., Enke, K., Ewing, J. A., Gienapp, H., Hasselmann, D.E., Kruseman, P., Meerburg, A., Müller, P., Olbers, D.J., Richter, K., Sell, W. & Walden, H. 1973 *Measurements of wind-wave growth and swell decay during the Joint North Sea Wave Project (JONSWAP)*. Deutsches Hydrographisches Institut.

He, G., Jin, G. & Yang, Y. 2017 Space-time correlations and dynamic coupling in turbulent flows. *Annu. Rev. Fluid Mech.* **49** (1), 51–70.

He, G. W. & Zhang, J. B. 2006 Elliptic model for space-time correlations in turbulent shear flows. *Phys. Rev. E - Stat. Nonlinear, Soft Matter Phys.* **73** (5), 2–5.

Helfrich, K. R. & Melville, W. K. 2006 Long nonlinear internal waves. *Annu. Rev. Fluid Mech.* **38**, 395–425.

Holthuijsen, L. H. 2007 *Waves in oceanic and coastal waters*. Cambridge: Cambridge University Press.

Hristov, T. S., Friehe, C. A. & Miller, S. D. 1998 Wave-coherent fields in air flow over ocean waves: Identification of cooperative behavior buried in turbulence. *Phys. Rev. Lett.* **81**, 5245–5248.

Hristov, T. S., Miller, S. D. & Friehe, C. A. 2003 Dynamical coupling of wind and ocean waves through wave-induced air flow. *Nature* **422** (6927), 55–58.

Hsu, S. A. 1988 *Coastal meteorology*. Elsevier.

Hussain, A. K. M. F. & Reynolds, W. C. 1972 The mechanics of an organized wave in turbulent shear flow. Part 2. Experimental results. *J. Fluid Mech.* **54** (02), 241.

Hwang, P. A. 2004 Influence of wavelength on the parameterization of drag coefficient and surface roughness. *J. Oceanogr.* **60** (5), 835–841.

Hwang, P. A. & Wang, D. W. 2004 Field measurements of duration-limited growth of wind-generated ocean surface waves at young stage of development. *J. Phys. Oceanogr.* **34**, 2316–2326.

Hwang, Y. & Bengana, Y. 2016 Self-sustaining process of minimal attached eddies in turbulent channel flow. *J. Fluid Mech.* **795**, 708–738.

Iafrati, A., De Vita, F. & Verzicco, R. 2019 Effects of the wind on the breaking of modulated wave trains. *Eur. J. Mech. - B/Fluids* **73**, 6–23.

Jackson, C., Silva, J. D. & Jeans, G. 2013 Nonlinear internal waves in synthetic aperture radar imagery. *Oceanography* **26** (2), 68–79.

Janssen, P. A. E. M. 2009 On some consequences of the canonical transformation in the Hamiltonian theory of water waves. *J. Fluid Mech.* **637**, 1–44.

Jeffreys, H. 1925 On the formation of water waves by wind. *Proc. R. Soc. A Math. Phys. Eng. Sci.* **107** (742), 189–206.

Jeffreys, H. 1926 On the formation of water waves by wind (second paper). *Proc. R. Soc. A Math. Phys. Eng. Sci.* **110** (754), 241–247.

Jiang, Q., Sullivan, P., Wang, S., Doyle, J. & Vincent, L. 2016 Impact of swell on air–sea momentum flux and marine boundary layer under low-wind conditions. *J. Atmos. Sci.* **73** (7), 2683–2697.

Kaihatu, J. M., Veeramony, J., Edwards, K. L. & Kirby, J. T. 2007 Asymptotic behavior of frequency and wave number spectra of nearshore shoaling and breaking waves. *J. Geophys. Res.* **112** (C6), C06016.

Kats, A. V. & Kontorovich, V. M. 1973 Symmetry properties of the collision integral and non-isotropic stationary solutions in weak turbulence theory. *J. Exp. Theor. Phys.* **37** (1), 80–85.

Kats, A. V. & Kontorovich, V. M. 1974 Anisotropic turbulent distributions for waves with a nondecay dispersion law. *J. Exp. Theor. Phys.* **38** (1), 102–107.

Kawai, S. 1981 Visualization of airflow separation over wind-wave crests under moderate wind. *Boundary-Layer Meteorol.* **21** (1), 93–104.

Kihara, N., Hanazaki, H., Mizuya, T. & Ueda, H. 2007 Relationship between airflow at the critical height and momentum transfer to the traveling waves. *Phys. Fluids* **19** (1), 015102.

Kirby, J. T. 1986 A general wave equation for waves over rippled beds. *J. Fluid Mech.* **162**, 171–186.

Kirby, J. T. & Kaihatu, J. M. 1996 Structure of frequency domain models for random wave breaking. *Coast. Eng. Proc.* **25**, 1144–1155.

Kitaigorodskii, S. A. 1968 On the calculation of the aerodynamic roughness of the sea surface. *Izv. Russ. Acad. Sci. Atmos. Ocean. Phys., Engl. Transl.* **4**, 498–502.

Kitaigorodskii, S. A. & Volkov, Y. A. 1965 On the roughness parameter of the sea surface and the calculation of momentum flux in the near water layer of the atmosphere. *Bull. Acad. Sci. USSR Atmos. Ocean. Phys.* **1**, 973–988.

Kodaira, T., Waseda, T., Miyata, M. & Choi, W. 2016 Internal solitary waves in a two-fluid system with a free surface. *J. Fluid Mech.* **804**, 201–223.

Kolassa, J. E. 2006 *Series approximation methods in statistics*, *Lecture notes in statistics*, vol. 88. Springer-Verlag New York.

Komen, G. J., Cavaleri, L., Donelan, M. A., Hasselmann, K., Hasselmann, S. & Janssen, P. A. E. M. 1994 *Dynamics and modelling of ocean waves*. Cambridge: Cambridge University Press.

Korotkevich, A. O., Pushkarev, A., Resio, D. & Zakharov, V. E. 2008 Numerical verification of the weak turbulent model for swell evolution. *Eur. J. Mech. - B/Fluids* **27** (4), 361–387.

Lamb, H. 1932 *Hydrodynamics*. Cambridge: Cambridge University Press.

Li, P. Y., Xu, D. & Taylor, P. A. 2000 Numerical modelling of turbulent airflow over water waves. *Boundary-Layer Meteorol.* **95** (3), 397–425.

Lilly, D. K. 1992 A proposed modification of the Germano-subgrid-scale closure method. *Phys. Fluids A Fluid Dyn.* **4** (3), 633–635.

Lin, M.-Y., Moeng, C.-H., Tsai, W.-T., Sullivan, P. P. & Belcher, S. E. 2008 Direct numerical simulation of wind-wave generation processes. *J. Fluid Mech.* **616**, 1–30.

Liu, B. & He, Y. 2016 SAR raw data simulation for ocean scenes using inverse Omega-K algorithm. *IEEE Trans. Geosci. Remote Sens.* **54** (10), 6151–6169.

Liu, P. C. 1985 Testing parametric correlations for wind waves in the Great Lakes. *J. Great Lakes Res.* **11** (4), 478–491.

Liu, Y., Yang, D., Guo, X. & Shen, L. 2010 Numerical study of pressure forcing of wind on dynamically evolving water waves. *Phys. Fluids* **22** (4), 041704.

Liu, Y. & Yue, D. K. P. 1998 On generalized Bragg scattering of surface waves by bottom ripples. *J. Fluid Mech.* **356**, 297–326.

Longuet-Higgins, M. S. 1963 The effect of non-linearities on statistical distributions in the theory of sea waves. *J. Fluid Mech.* **17** (3), 459–480.

Lu, S. S. & Willmarth, W. W. 1973 Measurements of the structure of the Reynolds stress in a turbulent boundary layer. *J. Fluid Mech.* **60** (03), 481–511.

Mahrt, L., Vickers, D., Howell, J., Højstrup, J., Wilczak, J. M., Edson, J. B. & Hare, J. 1996 Sea surface drag coefficients in the Risø Air Sea Experiment. *J. Geophys. Res. Ocean.* **101** (C6), 14327.

Makin, V. K., Kudryavtsev, V. N. & Mastenbroek, C. 1995 Drag of the sea surface. *Boundary-Layer Meteorol.* **73** (1-2), 159–182.

Martin, S. 2014 *An Introduction to Ocean Remote Sensing*, 2nd edn. Cambridge: Cambridge University Press.

Mastenbroek, C., Makin, V. K., Garat, M. H. & Giovanangeli, J. P. 1996 Experimental evidence of the rapid distortion of turbulence in the air flow over water waves. *J. Fluid Mech.* **318**, 273–302.

Melville, W. K. 1996 The role of surface-wave breaking in air-sea interaction. *Annu. Rev. Fluid Mech.* **28** (1), 279–321.

Michel, F. & Parentani, R. 2014 Probing the thermal character of analogue Hawking radiation for shallow water waves? *Phys. Rev. D - Part. Fields, Gravit. Cosmol.* **90** (4), 044033.

Miles, J. W. 1957 On the generation of surface waves by shear flows. *J. Fluid Mech.* **3** (02), 185–204.

Miles, J. W. 1993 Surface-wave generation revisited. *J. Fluid Mech.* **256**, 427–441.

Miyata, M. 1985 An internal solitary wave of large amplitude. *La Mer* **23**, 43–48.

Munk, W. H. 1949 Surf beats. *Eos, Trans. Am. Geophys. Union* **30** (6), 849–854.

Munk, W. H. 1950 Orgin and generation of waves. In *Proc. First Conf. Coast. Eng.* (ed. J. W. Johnson), , vol. 1, pp. 1–4.

Nardin, J. C., Rousseaux, G. & Coullet, P. 2009 Wave-current interaction as a spatial dynamical system: Analogies with rainbow and black hole physics. *Phys. Rev. Lett.* **102** (12), 1–4.

Nazarenko, S. 2011 *Wave turbulence*. Heidelberg; New York: Springer.

Nikolayeva, Y. I. & Tsimring, L. S. 1986 Kinetic model of the wind generation of waves by turbulent wind. *Izv. Atmos. Ocean. Phys.* **22**, 102–107.

Nilsson, E. O., Rutgersson, A., Smedman, A.-S. & Sullivan, P. P. 2012 Convective boundary-layer structure in the presence of wind-following swell. *Q. J. R. Meteorol. Soc.* **138** (667), 1476–1489.

Ochi, M. K. & Wang, W.-C. 1984 Non-Gaussian characteristics of coastal waves. In *Proc. 19th Conf. Coast. Eng.*. Houston, Texas.

Onorato, M., Cavaleri, L., Fouques, S., Gramstad, O., Janssen, P. A. E. M., Monbaliu, J., Osborne, A. R., Pakozdi, C., Serio, M., Stansberg, C. T., Toffoli, A. & Trulsen, K. 2009 Statistical properties of mechanically generated surface gravity waves: a laboratory experiment in a three-dimensional wave basin. *J. Fluid Mech.* **627**, 235–257.

Oost, W. A., Komen, G. J., Jacobs, C. M. J., Van Oort, C. & Bonekamp, H. 2001 Indications for a wave dependent Charnock parameter from measurements during ASGAMAGE. *Geophys. Res. Lett.* **28** (14), 2795–2797.

Ortiz-Suslow, D. G., Haus, B. K., Williams, N. J., Laxague, N. J. M., Reniers, A. J. H. M. & Graber, H. C. 2015 The spatial-temporal variability of air-sea momentum fluxes observed at a tidal inlet. *J. Geophys. Res. Ocean.* **120** (2), 660–676.

Osborne, A. R. & Burch, T. L. 1980 Internal solitons in the Andaman Sea. *Science* **208** (4443), 451–460.

Peirson, W. L. & Garcia, A. W. 2008 On the wind-induced growth of slow water waves of finite steepness. *J. Fluid Mech.* **608**, 243–274.

Peregrine, D. H. 1976 Interaction of water waves and currents. In *Adv. Appl. Mech.* (ed. C.-S. Yih), pp. 9–117. Elsevier.

Perlin, M., Choi, W. & Tian, Z. 2013 Breaking waves in deep and intermediate waters. *Annu. Rev. Fluid Mech.* **45** (1), 115–145.

Perry, R. B. & Schimke, G. R. 1965 Large-amplitude internal waves observed off the northwest coast of Sumatra. *J. Geophys. Res.* **70** (10), 2319–2324.

Phillips, O. M. 1957 On the generation of waves by turbulent wind. *J. Fluid Mech.* **2** (05), 417–445.

Phillips, O. M. 1958 The equilibrium range in the spectrum of wind-generated waves. *J. Fluid Mech.* **4**, 426–434.

Phillips, O. M. 1966 *The dynamics of the upper ocean*.

Piomelli, U. & Balaras, E. 2002 Wall-layer models for large-eddy simulations. *Annu. Rev. Fluid Mech.* **34** (1), 349–374.

Plant, W. J. 1982 A relationship between wind stress and wave slope. *J. Geophys. Res. Ocean.* **87** (C3), 1961–1967.

Pope, S. B. 2000 *Turbulent flows*. Cambridge; New York: Cambridge University Press.

Porter, D. 2003 The mild-slope equations. *J. Fluid Mech.* **494**, 51–63.

Porter, D. & Staziker, D. J. 1995 Extensions of the mild-slope equation. *J. Fluid Mech.* **300**, 367–382.

Raupach, M. R. 1981 Conditional statistics of Reynolds stress in rough-wall and smooth-wall turbulent boundary layers. *J. Fluid Mech.* **108**, 363–382.

Reul, N., Branger, H. & Giovanangeli, J.-P. 1999 Air flow separation over unsteady breaking waves. *Phys. Fluids* **11** (7), 1959–1961.

Reul, N., Branger, H. & Giovanangeli, J.-P. 2008 Air flow structure over short-gravity breaking water waves. *Boundary-Layer Meteorol.* **126** (3), 477–505.

Rijnsdorp, D. P., Ruessink, G. & Zijlema, M. 2015 Infragravity-wave dynamics in a barred coastal region, a numerical study. *J. Geophys. Res. Ocean.* **120** (6), 4068–4089.

Romero, L., Lenain, L. & Melville, W. K. 2017 Observations of surface wave–current interaction. *J. Phys. Oceanogr.* **47** (3), 615–632.

Romero, L. & Melville, W. K. 2010 Numerical modeling of fetch-limited waves in the Gulf of Tehuantepec. *J. Phys. Oceanogr.* **40** (3), 466–486.

Schützhold, R. & Unruh, W. G. 2002 Gravity wave analogues of black holes. *Phys. Rev. D - Part. Fields, Gravit. Cosmol.* **66** (4), 044019.

Sergeev, D., Kandaurov, A., Troitskaya, Y., Caulliez, G., Bopp, M. & Jaehne, B. 2017 Laboratory modelling of the wind-wave interaction with modified PIV-method. *EPJ Web Conf.* **143**, 02101.

Shabani, B., Nielsen, P. & Baldock, T. 2014 Direct measurements of wind stress over the surf zone. *J. Geophys. Res. Ocean.* **119** (5), 2949–2973.

Sheremet, A., Davis, J. R., Tian, M., Hanson, J. L. & Hathaway, K. K. 2016 TRIADS: A phase-resolving model for nonlinear shoaling of directional wave spectra. *Ocean Model.* **99**, 60–74.

Smedman, A., Högström, U., Bergström, H. & Rutgersson, A. 1999 A case study of air–sea interaction during swell conditions. *J. Geophys. Res. Ocean.* **104**, 25833–25851.

Smith, R. 1975 The reflection of short gravity waves on a non-uniform current. *Math. Proc. Cambridge Philos. Soc.* **78** (03), 517–525.

Smith, S. D. 1980 Wind stress and heat flux over the ocean in gale force winds. *J. Phys. Oceanogr.* **10**, 709–726.

Smith, S. D. 1988 Coefficients for sea surface wind stress, heat flux, and wind profiles as a function of wind speed and temperature. *J. Geophys. Res. Ocean.* **93** (C12), 15467–15472.

Smith, S. D., Anderson, R. J., Oost, W. A., Kraan, C., Maat, N., De Cosmo, J., Katsaros, K. B., Davidson, K. L., Bumke, K., Hasse, L. & Chadwick, H. M. 1992 Sea surface wind stress and drag coefficients: The HEXOS results. *Boundary-Layer Meteorol.* **60** (1-2), 109–142.

Smits, A. J, McKeon, B. J. & Marusic, I. 2011 High-Reynolds number wall turbulence. *Annu. Rev. Fluid Mech.* **43**, 353–375.

Socquet-Juglard, H., Dysthe, K. B., Trulsen, K., Krogstad, H. E. & Liu, J. 2005 Probability distributions of surface gravity waves during spectral changes. *J. Fluid Mech.* **542**, 195–216.

Stansby, P. K. & Zhou, J. G. 1998 Shallow-water flow solver with non-hydrostatic pressure: 2D vertical plane problems. *Int. J. Numer. Methods Fluids* **28** (3), 541–563.

Stanton, T. P. & Ostrovsky, L. A. 1998 Observations of highly nonlinear internal solitons over the continental shelf. *Geophys. Res. Lett.* **25** (14), 2695–2698.

Sullivan, P. P., Edson, J. B., Hristov, T. & McWilliams, J. C. 2008 Large-eddy simulations and observations of atmospheric marine boundary layers above nonequilibrium surface waves. *J. Atmos. Sci.* **65** (4), 1225–1245.

Sullivan, P. P. & McWilliams, J. C. 2010 Dynamics of winds and currents coupled to surface waves. *Annu. Rev. Fluid Mech.* **42**, 19–42.

Sullivan, P. P., Mcwilliams, J. C. & Moeng, C. 2000 Simulation of turbulent flow over idealized water waves. *J. Fluid Mech.* **404**, 47–85.

Sullivan, P. P., McWilliams, J. C. & Patton, E. G. 2014 Large-eddy simulation of marine atmospheric boundary layers above a spectrum of moving waves. *J. Atmos. Sci.* **71**, 4001–4027.

Sutherland, B. R. 2010 *Internal gravity waves*. Cambridge: Cambridge University Press.

Sverdrup, H. U. & Munk, W. H. 1947 *Wind, sea, and swell: theory of relations for forecasting*. Washington, D.C.: U. S. Hydrographic Office.

Tanaka, M. 2001 Verification of Hasselmann's energy transfer among surface gravity waves by direct numerical simulations of primitive equations. *J. Fluid Mech.* **444**, 199–221.

Tanaka, M. & Wakayama, K. 2015 A numerical study on the energy transfer from surface waves to interfacial waves in a two-layer fluid system. *J. Fluid Mech.* **763**, 202–217.

Tayfun, M. A. 1980 Narrow-band nonlinear sea waves. *J. Geophys. Res. Ocean.* **85** (C3), 1548–1552.

Tayfun, M. A. & Fedele, F. 2007 Wave-height distributions and nonlinear effects. *Ocean Eng.* **34** (11-12), 1631–1649.

Taylor, G. I. 1938 The spectrum of turbulence. *Proc. R. Soc. A Math. Phys. Eng. Sci.* **164** (919), 476–490.

Taylor, P. K. & Yelland, M. J. 2001 The dependence of sea surface roughness on the height and steepness of the waves. *J. Phys. Oceanogr.* **31** (2), 572–590.

The WAVEWATCH III® Development Group 2016 User manual and system documentation of WAVEWATCH III® version 5.16. Tech. Note 329, NOAA/NWS/NCEP/MMAB, College Park, MD, USA, 326 pp. + Appendices.

Tian, Z., Perlin, M. & Choi, W. 2010 Observation of the occurrence of air flow separation over water waves. In *29th Int. Conf. Ocean. Offshore Arct. Eng. Vol. 4*, pp. 333–341. ASME.

Toba, Y. 1972 Local balance in the air-sea boundary processes. *J. Oceanogr.* **28** (3), 109–120.

Toffoli, A., Benoit, M., Onorato, M. & Bitner-Gregersen, E. M. 2009 The effect of third-order nonlinearity on statistical properties of random directional waves in finite depth. *Nonlinear Process. Geophys.* **16** (1), 131–139.

Tracy, B. A. & Resio, D. T. 1982 Theory and calculation of the nonlinear energy transfer between sea waves in deep water. *WES Rep. 11*. Hydraulics Laboratory, U.S. Army Engineer Waterways Experiment Station, Vicksburg, MS.

Troitskaya, Y., Sergeev, D., Ermakova, O. & Balandina, G. 2011*a* Statistical parameters of the air turbulent boundary layer over steep water waves measured by the PIV technique. *J. Phys. Oceanogr.* **41** (8), 1421–1454.

Troitskaya, Y., Sergeev, D., Kandaurov, A. & Kazakov, V. 2011*b* Air-sea interaction under hurricane wind conditions. In *Recent Hurric. Res. - Clim. Dyn. Soc. Impacts* (ed. A. Lupo). InTech.

Troitskaya, Y. I., Sergeev, D. A., Kandaurov, A. A., Baidakov, G. A., Vdovin, M. A. & Kazakov, V. I. 2012 Laboratory and theoretical modeling of air-sea momentum transfer under severe wind conditions. *J. Geophys. Res. Ocean.* **117** (C11), C00J21.

Tucker, M. J. 1950 Surf beats: sea waves of 1 to 5 min. period. *Proc. R. Soc. A Math. Phys. Eng. Sci.* **202** (1071), 565–573.

Tulin, M. P. & Waseda, T. 1999 Laboratory observations of wave group evolution, including breaking effects. *J. Fluid Mech.* **378**, 197–232.

Veron, F., Saxena, G. & Misra, S. K. 2007 Measurements of the viscous tangential stress in the airflow above wind waves. *Geophys. Res. Lett.* **34** (19), L19603.

Wabnitz, S. 2013 Optical tsunamis: shoaling of shallow water rogue waves in nonlinear fibers with normal dispersion. *J. Opt.* **15** (6), 064002.

Wallace, J. M., Eckelmann, H. & Brodkey, R. S. 1972 The wall region in turbulent shear flow. *J. Fluid Mech.* **54** (01), 39.

Webb, D. J. 1978 Non-linear transfers between sea waves. *Deep Sea Res.* **25**, 279–298.

Wei, Z. & Jia, Y. 2014 Simulation of nearshore wave processes by a depth-integrated non-hydrostatic finite element model. *Coast. Eng.* **83**, 93–107.

Wetzel, B., Bongiovanni, D., Kues, M., Hu, Y., Chen, Z., Dudley, J. M., Wabnitz, S. & Morandotti, R. 2015 Experimental signature of Riemann wave shoaling in optical fiber. In *2015 Eur. Conf. Lasers Electro-Optics - Eur. Quantum Electron. Conf.*, , vol. 2293. Optical Society of America.

Wilczek, M. & Narita, Y. 2012 Wave-number-frequency spectrum for turbulence from a random sweeping hypothesis with mean flow. *Phys. Rev. E - Stat. Nonlinear, Soft Matter Phys.* **86** (6), 1–8.

Woodson, C. B. 2018 The fate and impact of internal waves in nearshore ecosystems. *Ann. Rev. Mar. Sci.* **10** (1), 421–441.

Wu, G. 2004 Direct simulation and deterministic prediction of large-scale nonlinear ocean wave-field. PhD thesis, Massachusetts Institute of Technology.

Wu, J. 1980 Wind-stress coefficients over sea surface near neutral conditions–a revisit. *J. Phys. Oceanogr.* **10** (5), 727–740.

Xiao, W., Liu, Y., Wu, G. & Yue, D. K. P. 2013 Rogue wave occurrence and dynamics by direct simulations of nonlinear wave-field evolution. *J. Fluid Mech.* **720**, 357–392.

Yang, D., Meneveau, C. & Shen, L. 2013 Dynamic modelling of sea-surface roughness for large-eddy simulation of wind over ocean wavefield. *J. Fluid Mech.* **726**, 62–99.

Yang, D., Meneveau, C. & Shen, L. 2014*a* Effect of downwind swells on offshore wind energy harvesting – a large-eddy simulation study. *Renew. Energy* **70**, 11–23.

Yang, D., Meneveau, C. & Shen, L. 2014*b* Large-eddy simulation of offshore wind farm. *Phys. Fluids* **26** (2), 025101.

Yang, D. & Shen, L. 2010 Direct-simulation-based study of turbulent flow over various waving boundaries. *J. Fluid Mech.* **650**, 131–180.

Yang, D. & Shen, L. 2011*a* Simulation of viscous flows with undulatory boundaries. Part I: Basic solver. *J. Comput. Phys.* **230** (14), 5488–5509.

Yang, D. & Shen, L. 2011*b* Simulation of viscous flows with undulatory boundaries: Part II. Coupling with other solvers for two-fluid computations. *J. Comput. Phys.* **230** (14), 5510–5531.

Yang, D. & Shen, L. 2017 Direct numerical simulation of scalar transport in turbulent flows over progressive surface waves. *J. Fluid Mech.* **819**, 58–103.

Yang, Z., Calderer, A., He, S., Sotiropoulos, F., Doyle, J., Flagg, D., MacMahan, J., Wang, Q., Haus, B., Graber, H. & Shen, L. 2018*a* Numerical study on the effect of air–sea–land interaction on the atmospheric boundary layer in coastal area. *Atmosphere (Basel).* **9** (2), 51.

Yang, Z., Deng, B.-Q. & Shen, L. 2018*b* Direct numerical simulation of wind turbulence over breaking waves. *J. Fluid Mech.* **850**, 120–155.

Yoshida, T. 2017 Azimuthal ocean wave emerged in SAR image spectra under specific condition. *J. Geophys. Res. Ocean.* **122** (12), 9625–9635.

Young, I. R. 1999 *Wind generated ocean waves*, 1st edn. Amsterdam; New York: Elsevier.

Zakharov, V. E. 1968 Stability of periodic waves of finite amplitude on the surface of a deep fluid. *J. Appl. Mech. Tech. Phys.* **9** (2), 190–194.

Zakharov, V. E., Badulin, S. I., Hwang, P. A. & Caulliez, G. 2015 Universality of sea wave growth and its physical roots. *J. Fluid Mech.* **780**, 503–535.

Zakharov, V. E. & Zaslavskii, M. M. 1982 Kinetic equation and Kolmogorov spectra in the weak turbulence theory of wind waves. *Izv. Akad. Nauk SSSR. Fiz. Atmos. i okeana* **18** (9), 970–979.

Zhao, Z.-K., Liu, C.-X., Li, Q., Dai, G.-F., Song, Q.-T. & Lv, W.-H. 2015 Typhoon air-sea drag coefficient in coastal regions. *J. Geophys. Res. Ocean.* **120** (2), 716–727.

Ziegenbein, J. 1969 Short internal waves in the Strait of Gibraltar. *Deep Sea Res. Oceanogr. Abstr.* **16** (5), 479–487.

Zijlema, M., Stelling, G. & Smit, P. B. 2011 SWASH: An operational public domain code for simulating wave fields and rapidly varied flows in coastal waters. *Coast. Eng.* **58** (10), 992–1012.

Zonta, F., Soldati, A. & Onorato, M. 2015 Growth and spectra of gravity–capillary waves in countercurrent air/water turbulent flow. *J. Fluid Mech.* **777**, 245–259.

A Grid resolution and perturbation order in HOS simulation

We design a numerical experiment to assess the effect of grid number and order of nonlinearity in the wave simulation. For the sake of computational cost, the experiment involves only the wave simulation solving equations (12) and (13). The physical parameter setting of the initial wave field is the same as that in table 1. The numerical parameters are listed in table 13, where the case BM simply repeats the wave portion in the coupled wind–wave simulation. For all simulations, the time step is approximately $8.7 \times 10^{-3} T_{p0}$ and the simulation duration is $104 T_{p0}$, comparable to the study of Tanaka (2001). The maximum grid number (case GN2048) is about 2×10^6, the same as that in Korotkevich *et al.* (2008). When the grid number is reduced (case GN256), the high frequency part of wave spectrum is not accurately resolved (figure 31a) because of low resolution. On the other hand, the results in the cases BM, GN1024 and GN2048 collapse for all frequencies, suggesting that the grid resolution (512, 256) is sufficiently high to resolve wave dynamics. In figure 31(b), we observe a significant deviation in spectrum when the perturbation expansion order is two, showing that the nonlinear interactions are not captured. On the other hand, the result of case BM is consistent with those in cases PO4 and PO5. In conclusion, the result of this test shows that our choice of numerical parameters is appropriate in the coupled wind–wave simulation.

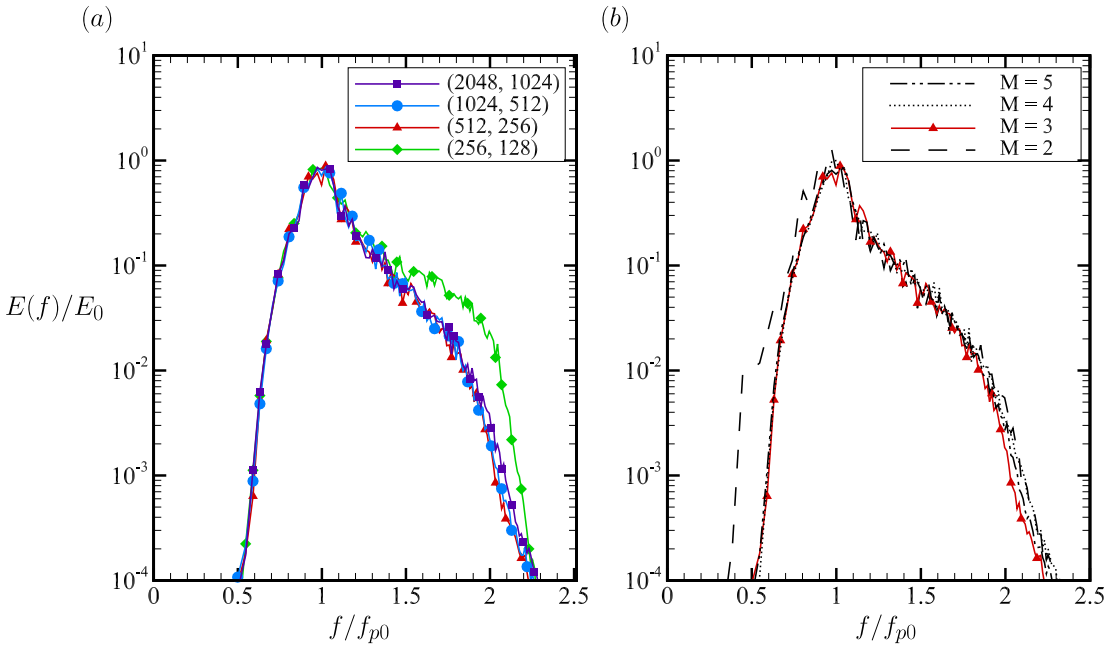

Figure 31: Normalised omnidirectional frequency spectrum calculated with: (a) different grid numbers; and (b) different perturbation orders. In (a), the results are from cases BM, GN256, GN1024, and GN2048. In (b), results are from cases BM, PO2, PO4, and PO5. The spectra are calculated from the instantaneous wave field at $t/T_{p0} = 104$.

Case	Grid number	Perturbation order M
BM	(512, 256)	3
GN256	(256, 128)	3
GN1024	(1024, 512)	3
GN2048	(2048, 1024)	3
PO2	(512, 256)	2
PO4	(512, 256)	4
PO5	(512, 256)	5

Table 13: Numerical parameters of the test cases. Case BM has the same settings as the wave part in the coupled LES–HOS simulation. Cases GNx are designed to test the effect of grid number. Cases POx are designed to test the effect of maximum perturbation order.

B Gram-Charlier series

The Gram-Charlier series is an approximation to the Gaussian distribution (see Kolassa, 2006, chap. 3). It has the following form when truncated to the finite order

$$f(x) = \frac{1}{\sqrt{2\pi\kappa_2}} \exp\left[-\frac{(x-\kappa_1)^2}{2\kappa_2}\right] \times \left[1 + \frac{\kappa_3}{3!\kappa_2^{3/2}} H_3\left(\frac{x-\kappa_1}{\kappa_2^{1/2}}\right) + \frac{\kappa_4}{4!\kappa_2^2} H_4\left(\frac{x-\kappa_1}{\kappa_2^{1/2}}\right)\right], \tag{99}$$

where κ_i is the ith cumulant, and $H_3(\cdot)$ and $H_4(\cdot)$ are the third and fourth Hermite polynomials, respectively.

Equation (99) is valid under the condition that the distribution of the data is approximately Gaussian. Otherwise, the series do not converge and thus the approximation fails to hold rigorously. For the distribution of ocean surface elevation with a zero mean, κ_3 and κ_4 can be approximated using the skewness C_3 and kurtosis C_4, respectively. For the standard Gaussian distribution, $C_3 = 0$ and $C_4 = 3$.

C Surface wave spectrum

Here we briefly review two types of spectrum commonly used in the analysis of surface wave energy: the wavenumber spectrum and the directional frequency spectrum. The reader is referred to Young (1999) and Holthuijsen (2007) for more details. The wavenumber spectrum is defined as

$$E(k_x, k_y) = \lim_{\Delta k_x \to 0} \lim_{\Delta k_x \to 0} \frac{1}{\Delta k_x \Delta k_y} E\{\frac{1}{2}a^2\}, \tag{100}$$

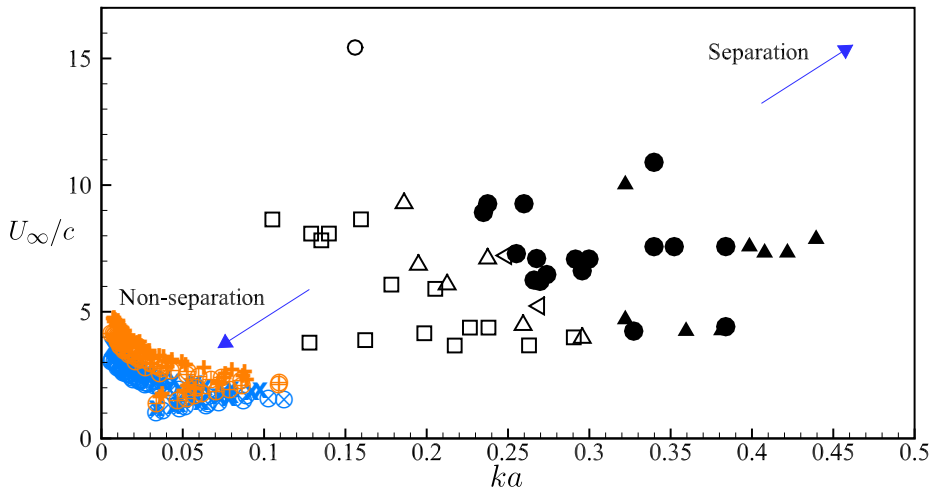

Figure 32: Wind–wave conditions related to air flow separation over water waves. Here, U_∞ denotes the free-stream wind speed. In Tian *et al.* (2010), the conditions are divided into the following categories: no separations, denoted by $\square$; separation undetermined, denoted by $\triangle$; separations over non-breaking waves, denoted by $\bullet$; separations over breaking waves, denoted by $\blacktriangle$. Also included in their paper are results from Kawai (1981), denoted by $\bigcirc$, and Donelan *et al.* (2006), denoted by $\triangleleft$. The trends of non-separation and separation are denoted by blue arrows. The present simulation results are denoted by: $\otimes$, case WW6; $\times$, case WW7; $\oplus$, case WW8; $+$, case WW9.

where a is the amplitude of the corresponding wave component and $E\{\frac{1}{2}a^2\}$ denotes the variance in a spectral bin $(\Delta k_x, \Delta k_y)$. The directional spectrum is defined as

$$E(f,\theta) = \lim_{\Delta f \to 0} \lim_{\Delta \theta \to 0} \frac{1}{\Delta f \Delta \theta} E\{\frac{1}{2}a^2\}. \tag{101}$$

Equation (100) and (101) are related by

$$E(f,\theta) = E(k_x, k_y) \frac{\partial(f,\theta)}{\partial(k_x, k_y)}, \tag{102}$$

where the Jacobian $\partial(f,\theta)/\partial(k_x, k_y)$ can be readily obtained from the dispersion relation.

D Wind input by tangential stress and wave energy dissipation

The energy transfer from wind to wave can be caused by normal stress and tangential stress. Generally, the work done by the tangential stress is small compared with that done by normal stress (Young, 1999). Under certain sea states, the air flow separation may occur and the effect of the tangential stress cannot be neglected (Tian, Perlin & Choi, 2010). In figure 32, we compare the wind–wave conditions of each individual wave component in our simulation with experimental data (Kawai, 1981; Donelan *et al.*, 2006; Tian *et al.*, 2010). While there is no rigorous criterion for determining the boundary of separation as indicated by the study of Tian *et al.* (2010), our result shows that both the wave steepness and the wind speed relative to the waves are

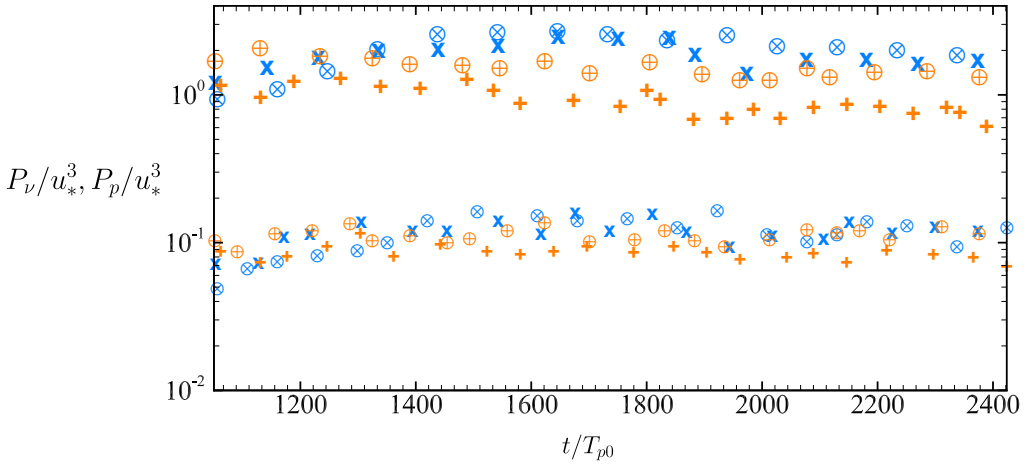

Figure 33: Time history of the work done by stress at the wave surface. The work done by tangential stress P_ν is denoted by the smaller symbols while that done by the pressure P_p is denoted by the larger ones. The present simulation results are denoted by: $\otimes$, case WW6; $\times$, case WW7; $\oplus$, case WW8; $+$, case WW9.

small, suggesting that the air flow separation is unlikely to occur for the wind field in the present study. Consequently, we expect the energy transfer related to the tangential stress to be negligibly small.

To quantitatively assess the significance of tangential stress, we define the work done by the tangential stress and the pressure per unit area per unit time as

$$P_\nu = \frac{1}{A}\int_A \left(u_*^2 - \frac{p_a}{\rho_a}\frac{\partial \eta}{\partial x}\right) u_s \mathrm{d}A, \tag{103}$$

$$P_p = \frac{1}{A}\int_A \frac{p_a}{\rho_a} u_n \mathrm{d}A, \tag{104}$$

where u_s is the streamwise velocity component at the wave surface, u_n is the velocity component normal to the wave surface, and A denotes the area of the entire wave field. Note that the tangential stress on the air side is not directly calculated from the velocity profile as in the DNS of Yang & Shen (2010). Instead, in the present study, it

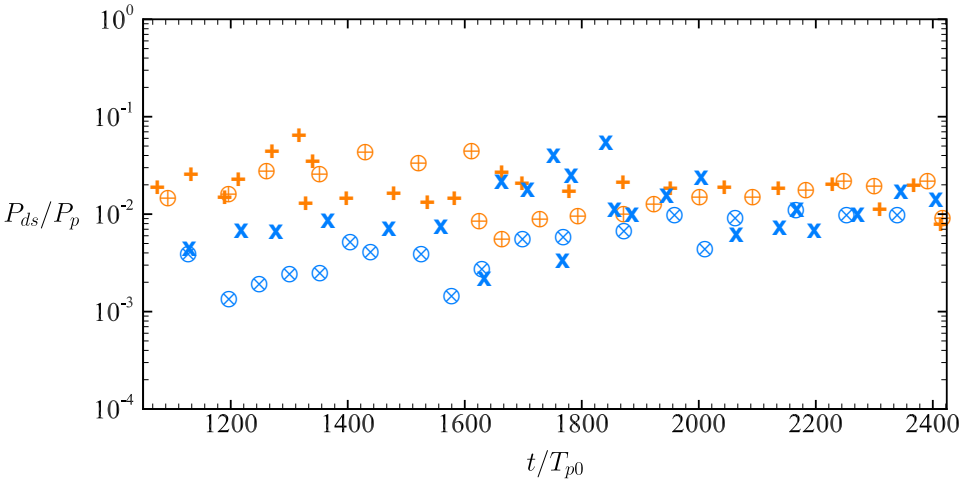

Figure 34: Time history of the ratio of the wave energy dissipation rate to the wind input induced by pressure. The present simulation results are denoted by: $\otimes$, case WW6; $\times$, case WW7; $\oplus$, case WW8; $+$, case WW9.

is estimated by subtracting the horizontal component of the pressure-induced stress from the total stress. As shown in figure 33, the work done by the tangential stress is one order of magnitude smaller than that done by pressure.

The wave energy dissipation modelled by the adaptive filter (14) can be estimated by

$$P_{ds} = \int \frac{\eta^2(\boldsymbol{k})}{\Delta t} \left[1 - G^2(k; C_1, C_2)\right] \mathrm{d}\boldsymbol{k}. \tag{105}$$

The value of P_{ds} is therefore a measure of the wave energy dissipated via the filter per unit area per unit time. By comparing it with the work done by the pressure, we find that the magnitude of P_{ds} is generally one to three orders smaller than P_p (figure 34). Therefore, this energy dissipation is not a significant issue with regards to the wave evolution in the present study. Note that wave breaking in the real ocean is a very complex process, and the value calculated from (105) shall not be viewed as a high-accuracy measure of the energy dissipation induced by wave breaking.

E Drag coefficient and surface roughness

The drag coefficient is defined as:

$$C_D = \frac{\tau}{\rho_a U^2}, \tag{106}$$

where τ is the total drag, ρ_a is the air density, and U is the wind speed. According to Edson *et al.* (2013), U should be the relative wind speed with respect to waves, especially when there is a strong current. When surface currents are weak, it is reasonable to use the absolute wind speed relative to fixed Earth.

Under the constant-stress assumption, one can derive a logarithmic law for the mean wind profile from dimensional analysis (see e.g. Pope, 2000):

$$U(z) = \frac{u_\tau}{\kappa} \log \frac{z}{z_0}, \tag{107}$$

where κ is the von Kármán constant, and z_0 is the aerodynamic surface roughness.

Substituting (107) into (106), one can get the height-dependent drag coefficient:

$$C_D(z) = \kappa^2 \left(\log \frac{z}{z_0} \right)^{-2}. \tag{108}$$

In field measurements, C_D is usually calculated at a reference height. For example, a commonly used height is $z_{10} = 10$ m, and $C_{D,10} = \kappa^2 \left[\log(z_{10}/z_0) \right]^{-2}$.

F Shoaling coefficient

The wave shoaling process can be quantified analytically in certain scenarios when the sea state and bottom bathymetry are relatively simple. We outline the derivation of the shoaling coefficient in Dean & Dalrymple (1991), which used the following assumptions: (a) the nonlinear effects are small; (b) the propagation direction of the wave is perpendicular to the shoreline; (c) the water depth is only a function of the distance from the shoreline; (d) the wave frequency and the wave energy flux are constant in the wave shoaling process.

Suppose that in the open sea a wave has the wavenumber k_0 and amplitude a_0, which change to k and a respectively at a water depth h in the coastal region. The change in wavenumber can be evaluated from the dispersion relation and conservation of wave frequency ω:

$$\omega^2 = gk \tanh(kh) = gk_0. \tag{109}$$

By conservation of the energy flux transferred by the wave motion, we have:

$$c_{g0} a_0^2 = c_g a^2, \tag{110}$$

where c_g is the wave group velocity. Note that the open sea quantities are denoted with a subscript '0'.

From (110), we can obtain the shoaling coefficient:

$$K_s = \frac{a}{a_0} = \sqrt{\frac{c_{g0}}{c_g}}, \tag{111}$$

where the ratio c_{g0}/c_g can be readily obtained from (109).